

**UCLA**

**UCLA Electronic Theses and Dissertations**

**Title**

Design, Control, and Measurement of Molecular and Supramolecular Assemblies

**Permalink**

<https://escholarship.org/uc/item/8946d05d>

**Author**

Pathem, Bala Krishna

**Publication Date**

2012

Peer reviewed|Thesis/dissertation

UNIVERSITY OF CALIFORNIA

Los Angeles

*Design, Control, and Measurement  
of Molecular and Supramolecular Assemblies*

A dissertation submitted in partial satisfaction of the  
requirements for the degree Doctor of Philosophy  
in Chemistry

by

Bala Krishna Pathem

2012



# **ABSTRACT OF THE DISSERTATION**

## **Design, Control, and Measurement of Molecular and Supramolecular Assemblies**

by

Bala Krishna Pathem

Doctor of Philosophy in Chemistry

University of California, Los Angeles, 2012

Professor Paul S. Weiss, Chair

Molecular switches and motors respond structurally, electronically, optically, and/or mechanically to external stimuli, testing and potentially enabling extreme miniaturization of optoelectronic devices, nanoelectromechanical systems, and medical devices. Assembling motors and switches on surfaces makes it possible both to measure the properties of individual molecules as they relate to their environment, and to couple function between assembled molecules. We designed molecules with precise functionality and assembled them on solid substrates either as isolated single molecules, linear one-dimensional chains, or as two-

dimensional islands in order to measure and to test the fundamental limits and cooperative function of the assemblies. We established that proximate functional molecules interact with each other to drive unprecedented cooperative motion at the nanoscale. In conjunction with theory, we establish the mechanism by which the molecules perform this nanoscale action. We modify the environments in which these assemblies are adsorbed to tune their dipole-dipole interactions via self- and directed assembly. We establish the role of the tethers that decouple the functional molecules from the underlying conductive substrates. By varying the composition of the tether we understood that the molecular function varies inversely with the conductance of the tether. In order to circumvent problems with steric hindrance in molecular assemblies, novel functional molecules were designed and tested at single-molecule and at ensemble scales. This thesis details the effects of parameters such as the molecular environment, intermolecular interactions, and internal functional groups of molecular switches on their nanoscale actuation.

The dissertation of Bala Krishna Pathem is approved.

Kendall N. Houk

James K. Gimzewski

Bruce S. Dunn

Paul S. Weiss, Committee Chair

University of California, Los Angeles

2012

To my family

## TABLE OF CONTENTS

### Page

List of Figures .....	viii
List of Abbreviations .....	xxi
Acknowledgments .....	xxiv
Vita .....	xxix
List of Publications and Presentations .....	xxx

## CHAPTER 1 *INTRODUCTION*

1.1	Introduction .....	2
1.1.1	Assembly of Molecular Switches and Motors on Surfaces .....	3
1.1.2	Self-Assembled Monolayers .....	3
1.1.3	Single Molecules and Assemblies in Controlled Environments .....	4
1.2	Molecular Switches .....	5
1.2.1	Electronic Switches .....	5
1.2.2	Conductance Depends Strongly on Contacts and Energy Level Alignment .....	6
1.2.3	Oligo(phenylene ethynylene)s and Proposed Switching Mechanisms .....	9
1.3	Photochromic Switches .....	13
1.3.1	Photochromic Switches Function Differently on Surfaces .....	14
1.3.2	Isomerization on Surfaces Initiated by Tunneling Electrons .....	17
1.3.3	Isomerization on Surfaces Initiated by Electric Field .....	19
1.3.4	Coupled Isomerization on Surfaces .....	19
1.4	Summary and Thesis Outlook .....	20
1.5	References .....	29



## **CHAPTER 2 *INSTRUMENTATION***

2.1	Scanning Tunneling Microscopy .....	43
2.2	Surface-Enhanced Raman Spectroscopy .....	44
2.3	References .....	52

## **CHAPTER 3 *COORDINATED DRIVEN MOTION OF ASSEMBLED ONE-DIMENSIONAL CHAINS OF TETHERED FUNCTIONAL MOLECULES***

3.1	Introduction .....	57
3.2	Methods .....	58
3.3	Results and Discussions .....	59
3.4	Conclusions and Future Prospects .....	65
3.5	References .....	73

## **CHAPTER 4 *DIRECTED ASSEMBLY OF PRECISE SUPRAMOLECULAR STRUCTURES TO TUNE THEIR DIPOLE-DIPOLE INTERACTIONS***

4.1	Introduction .....	78
4.2	Methods .....	79
4.3	Results and Discussions .....	80
4.4	Conclusions and Future Prospects .....	87
4.5	References .....	95

**CHAPTER 5 EFFECT OF TETHER CONDUCTIVITY ON THE EFFICIENCY OF  
PHOTOISOMERIZATION OF AZOBENZENE-FUNCTIONALIZED MOLECULES ON  
*Au{111}***

5.1	Introduction .....	100
5.2	Methods .....	102
5.3	Results and Discussions .....	104
5.4	Conclusions and Future Prospects .....	108
5.5	References .....	119

**CHAPTER 6 PHOTOREACTION OF MATRIX-ISOLATED DIHYDROAZULENE-  
FUNCTIONALIZED MOLECULES ON *Au{111}***

6.1	Introduction .....	126
6.2	Methods .....	128
6.3	Results and Discussions .....	130
6.4	Conclusions and Future Prospects .....	134
6.5	References .....	143

**CHAPTER 7 OUTLOOK**

7.1	Outlook .....	151
7.1.1	Azobenzene .....	151
7.1.2	Dihydroazulene .....	152
7.1.3	Rotaxane .....	153
7.2	References .....	168

## LIST OF FIGURES

### CHAPTER 1 INTRODUCTION

- Figure 1.1.** Overview of electronic, photochromic, and mechanically interlocked molecular switches.....22
- Figure 1.2.** A) Reversible switching of an isolated single molecule inserted in an alkanethiolate matrix on Au{111} under imaging conditions of -1 V sample bias and 1 pA tunneling current. Figure reproduced with permission from reference 43. Copyright AAAS 2001. B) Phenanthracene molecule exhibits conduction switching even when the rotation of aromatic rings in the backbone is precluded. Figure reproduced with permission from reference 49. Copyright ACS 2006. C) The interaction of the dipole moment of the functionalized oligo(phenylene ethynylene) molecule with the electric field induced by the STM tip bias polarity changes the tilt angle of the molecule and leads to switching due to changes in the S-Au bond hybridization. Figure reproduced with permission from reference 47. Copyright ACS 2005. D) Dithiol-functionalized molecules are capable of moving up and down substrate step edges and also changing conductance via tilt. Figure reproduced with permission from reference 48. Copyright ACS 2005 .....23
- Figure 1.3.** Simplified schematic depicting the *trans* to *cis* isomerization paths of azobenzene in the gas phase. Figure reproduced with permission from reference 147. Copyright ACS 2005.....25
- Figure 1.4.** A) Unfunctionalized and 4,4'-di-*tert*-butyl-functionalized azobenzene did not exhibit isomerization, whereas 3,3',5,5'-tetra-*tert*-butyl-functionalized molecules

switched reversibly, between *trans* and *cis* conformations under continuous UV light irradiation. Figure reproduced with permission from reference 160. Copyright APS 2007. B) Azobenzene deposited on a thin insulating NaCl layer on Ag(111) exhibits unidirectional *trans* to *cis* photoisomerization. Figure reproduced with permission from reference 168. Copyright APS 2012. C) Azobenzene molecules functionalized with linear chains exhibit reversible isomerization under ambient conditions. Figure reproduced with permission from reference 53. Copyright ACS 2008. D) 3,3',5,5'-tetra-*tert*-butyl-functionalized azobenzene located at the edges of islands and at domains switched in bundles when assembled on GaAs(110) surface. Figure reproduced with permission from reference 169. Copyright ACS 2011..... 26

**Figure 1.5.** A) Unfunctionalized azobenzene switched from *trans* to *cis* conformation during current-voltage (I-V) measurements (sudden changes in current at -1.5 V bias can be seen, indicating changes in molecular conformation). Figure reproduced with permission from reference 141. Copyright APS 2006. B) Sequence of images showing unidirectional switching of amine-functionalized azobenzenes using tunneling electrons. Figure reproduced with permission from reference 140. Copyright Elsevier 2007. C) Electric field-induced isomerization of bundles of 3,3',5,5'-tetra-*tert*-butyl-functionalized molecules. Isolated single molecules could not be isomerized due to diffusion on the surface. Figure reproduced with permission from reference 140. Copyright ACS 2006... ..27

## CHAPTER 2 *INSTRUMENTATION*

- Figure 2.1.** Energy level diagram depicting a one-dimensional electron tunneling junction in scanning tunneling microscopy. A positive sample bias is shown in the schematic, which results in the electron tunneling from the probe to the sample .....50
- Figure 2.2.** Schematics depicting: A) Rayleigh scattering in which the excited electron relaxes to the same energy level resulting in no net change in the energy of the emitted photon, B) Stokes scattering, in which the excited electron relaxes to an energy level higher than the initial state resulting in a net loss of energy of the emitted photon, and C) anti-Stokes scattering, in which the excited electron relaxes to an energy level lower than the initial state, resulting in a net increase in the energy of the scattered photon .....51

## CHAPTER 3 *COORDINATED DRIVEN MOTION OF ASSEMBLED ONE-DIMENSIONAL CHAINS OF TETHERED FUNCTIONAL MOLECULES*

- Figure 3.1.** (A) Structure of the azobenzene-functionalized molecule (4-[2-(4-phenylazo-phenyl)-ethoxy]-butane-1-thiol), **Azo**. Scanning tunneling microscope images of (B) single-row chain of **Azo** molecules assembled at the domain boundaries of a decanethiol self-assembled monolayer matrix on Au{111} with nearest neighbor distances of  $4.5 \pm 0.3 \text{ \AA}$  (see inset) and (C) double-row chain of **Azo** molecules. Inset: Herringbone arrangements with center-to-center intermolecular distances of  $8.8 \pm 0.4 \text{ \AA}$  and  $5.0 \pm 0.3 \text{ \AA}$  between the farthest and the nearest neighbors in the repeating unit cell. Imaging conditions:  $V_s = 1.0 \text{ V}$  and  $I_t = 1 \text{ pA}$  .....66

**Figure 3.2.** Scanning tunneling microscope images following tunneling-electron-induced isomerization of a 1D chain of **Azo**. (A) All the molecules are initially found in their thermodynamically stable *trans* (ON) state. The sample bias was then increased to 2.0 V and the scanning tunneling microscope probe tip positioned over the chain at the position indicated (yellow arrow) for 2 min. (B) All the coupled molecules in the chain switched to the *cis* conformation, as is evident by the change in the apparent heights of the molecules. (C) A nearby chain that was not electronically coupled (red box) did not isomerize. (D, E) High-resolution images of the 1D chain before and after isomerization. Line scans (F) before and (G) after isomerization, showing apparent reduction in height with respect to the surrounding self-assembled monolayer matrix (red lines from D and E). Imaging conditions:  $V_s = 1.0$  V and  $I_t = 1$  pA.....67

**Figure 3.3.** The transition states of neutral **Azo**, following an inversion mechanism for isomerization with a calculated barrier of 1.71 eV and anionic **Azo**, following a rotation mechanism for isomerization with a calculated barrier of 0.89 eV. The tether (**R**) has been removed in the plot for clarity. The dihedral angles are shown below the energy levels of each state.....69

**Figure 3.4.** (A) Scanning tunneling microscope image after the chain switches back to the *trans* conformation via thermal relaxation. (B) Line scan showing increment in apparent height with respect to surrounding matrix (See red line from Fig. 3.4A). Image conditions:  $V_s = 1.0$  V and  $I_t = 1$  pA.....70

**Figure 3.5.** Double-row chains (A) Before isomerization, all the molecules are in the more stable *trans* conformation. Sample bias was increased to 2.0 V and the scanning tunneling microscope probe tip was positioned over the chain (yellow arrow) for 5 min. (B) After isomerization, all the molecules switch OFF (*cis* conformation) and (C) molecules isomerize back to their *trans* conformation after 30 min at room temperature via thermal relaxation. Imaging conditions:  $V_s = 1.0$  V and  $I_t = 1$  pA .....71

**Figure 3.6.** Scanning tunneling microscope images following the photoinduced isomerization of chains: Both **1R** and **2R** chains switched OFF upon irradiation with UV light for 30 min at  $\sim 12$  mW/cm<sup>2</sup>. (A) A chain in its initial ON state, (B) All molecules in the **1R** chain switched OFF (*cis* conformation) after 30 min UV irradiation, (C) The chain switches back to ON (*trans* conformation) via thermal relaxation after 30 min at room temperature. (D) Initial state of **2R** chain before UV irradiation. (E) Parts of the **2R** chain did not switch OFF (red squares), presumably due to steric hindrance. All scanning tunneling microscope images were recorded at  $V_s = 1$  V and  $I_t = 1$  pA .....72

## CHAPTER 4 DIRECTED ASSEMBLY OF PRECISE SUPRAMOLECULAR STRUCTURES TO TUNE THEIR DIPOLE-DIPOLE INTERACTIONS

**Figure 4.1.** (a) A schematic of tethered azobenzene in self-assembled monolayer of thiolates on a Au surface, illustrating the effects of the light-induced intermolecular interactions (indicated by two black arrows) on the Raman signal. The red arrows indicate the excitation light and the purple arrows indicate the scattered light (*i.e.*, Raman signal). The inset shows a representative scanning electron micrograph of a nanohole array in a Au thin film. The scale bar in the inset is 600 nm. (b) Chemical structures of the two azobenzene-functionalized molecules studied, 4-(1-mercaptoundec-11-yloxy)-azobenzene (**Azo1**) and 4-[2-(4-phenylazo-phenyl)-ethoxy]-butane-1-thiol (**Azo2**), and the corresponding matrix molecules, dodecanethiolate (**C12**) and decanethiolate (**C10**). (c) An illustration of how the vapor-annealing method tunes the supramolecular structure of azobenzene-functionalized molecules. The gray and blue dots represent alkanethiol and azobenzene-functionalized molecules, respectively .....88

**Figure 4.2.** A series of scanning tunneling microscope images of **Azo2** in a decanethiol matrix as a function of vapor annealing time: (a) 0 min; (b) 30 min; (c) 60 min; and (d) 120 min. (e) The relative counts of each structure as a function of annealing time .....89

**Figure 4.3.** (a) A series of surface-enhanced Raman spectra of azobenzene-functionalized molecules (**Azo1**) as a function of annealing time. The numbers near the spectra indicate the annealing times in minutes; C1, C2, C3, C4, and C5 indicate the five



modes observed. (b) Evolution of peak area intensities of the five modes as a function of annealing time .....90

**Figure 4.4.** Control experiments with samples prepared by co-adsorption from solution. (a) Scanning tunneling microscope image of **Azo2** in a **C10** matrix without vapor annealing. (b) Scanning tunneling microscope image of **Azo2** in a **C10** matrix with vapor annealing for 120 min. (c) A series of surface-enhanced Raman spectra as a function of annealing time; the numbers near the spectra indicate the annealing time in minutes. C1, C2, C3, C4, and C5 indicate the five Raman modes observed. (d) Evolution of peak area intensities of the five modes as a function of annealing time .....91

**Figure 4.5.** (a) Three basic types of configuration of the azobenzene pairs. Left: face-to-face (FF), middle: face-to-side (FS), and right: side-to-side (SS). (b) The B3LYP/6-31G\* Raman spectra of azobenzene pairs in FF configurations as a function of the intermolecular distance  $R$ . The five major modes are indicated as C1-C5. The arrow indicates the spectra from high to low intensities corresponding to the  $R$  values.  $R=2*\text{single}$  indicates the spectrum obtained by doubling the single azobenzene spectrum. (c-e) The Raman differential cross sections of modes C1-C5 as a function of inter-azo distance for FF, FS, and SS configurations, respectively.  $R=2*\text{single}$  is assumed to be 20 Å for a better perspective of the figures. The B3LYP/6-31G\* frequencies where scaled by 0.9614 .....92

**Figure 4.6.** The polarizability of azobenzene pairs as function of intermolecular distance for the FF (black), FS (blue), and SS (olive) configurations where (a), (b), and (c) are

the xx, yy, and zz diagonal components of polarizability tensor, respectively, and (d) is the total isotropic polarizability. The solid curves are the polarizabilities calculated by the analytical model, while the points are the B3LYP/6-31G\* polarizabilities. As shown in Fig. 4.5a, the y-axis is the parallel axis while the x- and z-axes are the perpendicular axes.....94

## CHAPTER 5 EFFECT OF TETHER CONDUCTIVITY ON THE EFFICIENCY OF PHOTOISOMERIZATION OF AZOBENZENE-FUNCTIONALIZED MOLECULES ON Au{111}

**Figure 5.1.** Schematic of (left) **Azo1** and (right) **Azo2**. Due to the linear alkyl chain **Azo1** assumes  $\sim 30^\circ$  tilt with respect to surface normal, whereas **Azo2** assumes a nominally perpendicular orientation with respect to the Au{111} surface .....109

**Figure 5.2.** A) Simulated Raman spectra of *trans* and *cis* **Azo2** at various mole fractions as shown in the legend; The peaks labeled P1 and P2 were used to follow the kinetics of photoisomerization.....110

**Figure 5.3.** Calculated vibrational modes of all the prominent peaks of **Azo2** attached to a Au<sub>3</sub> cluster observed in theoretical calculations in their *trans* and *cis* conformations, respectively .....111

**Figure 5.4.** Schematics of the calculated vibrational modes of **Azo2** attached to a Au<sub>3</sub> cluster in a) P1 *trans*, b) P2 *trans*, c) P1 *cis*, and d) P2 *cis* geometries. The contributions to Raman peaks P1 and P2 are due to the tether and the benzene rings (predominantly, the lower ring) of the azobenzene moiety, respectively .....112

<b>Figure 5.5.</b>	Experimental surface-enhanced Raman spectra of <b>Azo2</b> on Au{111} nanohole arrays as a function of UV irradiation time (see legend). The spectra have been offset for clarity. The peaks labeled P1 and P2 are used for monitoring the photoisomerization kinetics .....	113
<b>Figure 5.6.</b>	Top: Experimental decay plot of peak ratios tracking <i>trans</i> to <i>cis</i> conversion of <b>Azo2</b> on Au{111} nanohole array, demonstrating the reduction in the peak area ratio (P2:P1). The calculated time constant from the decay plot was $61 \pm 11$ min. Bottom: Decay plot using peak area ratios from simulated SERS spectra showing the ratios expected as a function of photoconversion .....	114
<b>Figure 5.7.</b>	Top: The surface-enhanced Raman spectra showing the photoisomerization of <b>Azo2</b> back from <i>cis</i> to <i>trans</i> under visible light illumination over a period of 24 h (see legend). The spectra have been offset for clarity. Bottom: The exponential curve fit to the ratio of peak areas (P2: P1) shows the slower <i>cis</i> to <i>trans</i> back reaction. The x-axis has been truncated after 250 min to include the 24-h data point. The <i>cis</i> to <i>trans</i> photoisomerization of <b>Azo2</b> was found to be four times slower when compared to that of <b>Azo1</b> .....	116
<b>Figure 5.8.</b>	<b>Azo2</b> molecules assemble nominally perpendicular to the Au{111} surface as opposed to the tilted alignment of <b>Azo1</b> alkyl tethers. Imaging conditions: $V_s = -1$ V, $I = 1$ pA.....	118

## CHAPTER 6 PHOTOREACTION OF MATRIX-ISOLATED DIHYDROAZULENE-FUNCTIONALIZED MOLECULES ON Au{111}

- Figure 6.1.** Schematic of UV-light-induced photoreaction of functionalized dihydroazulene (**DHA'**, left) to a vinylheptafulvene (**VHF'**, right) isolated as single molecules in a dodecanethiol (**C12**) matrix and the back reaction via thermal relaxation .....135
- Figure 6.2.** Series of theoretical simulations of Raman spectra as a mixture of different mole fractions of functionalized dihydroazulene (**DHA'**) and corresponding vinylheptafulvene (**VHF'**), spectra are offset for clarity. Peaks labeled P1 and P2 were used to follow the photoreaction spectroscopically .....136
- Figure 6.3.** Vibrational modes of the peaks at  $1572\text{ cm}^{-1}$  in dihydroazulene (**DHA'**) and vinylheptafulvene (**VHF'**) isomers, respectively.....137
- Figure 6.4.** Vibrational mode P1 of a) functionalized dihydroazulene (**DHA'**) and b) vinylheptafulvene (**VHF'**) isomers. Vibrational mode P2 of c) **DHA'** and d) **VHF'** isomers.....138
- Figure 6.5.** Series of experimental surface-enhanced Raman spectra as a function of 365 nm UV light illumination time (the legend shows the duration of light illumination). The ratio of peaks labeled P1 and P2 was used to follow the kinetics of surface-bound molecular photoreaction. The spectra are offset for clarity .....139

- Figure 6.6.** Series of experimental surface-enhanced Raman spectra as a function of thermal relaxation time (the legend shows the thermal relaxation time at 30 °C). The spectra are offset for clarity .....140
- Figure 6.7.** (Left) The peak area ratio (P2:P1) as a function of UV light irradiation time fit to an exponential decay. The extracted time constant for dihydroazulene to vinylheptafulvene (**DHA'**→**VHF'**) photoreaction was  $9\pm2$  min. (Right) Data showing the increase in P2:P1 ratio as a function of thermal relaxation time at a constant temperature of 30 °C, also fit to an exponential curve. The time constant for the **VHF'**→**DHA'** thermal back reaction was  $38\pm7$  min. The errors bars are from five sets of measurements .....141
- Figure 6.8.** Plot showing the decrease in the P2:P1 peak area ration from simulated spectra as a function of **VHF'** mole fraction .....142

## CHAPTER 7 OUTLOOK

- Figure 7.1.** Structure of azobenzene-functionalized adamantanetrithioacetate molecule. The lateral separation between neighboring surface-bound molecules will be  $\sim 7.4$  Å, providing enough spatial freedom for the azobenzene moiety to switch between *trans* and *cis* conformations .....158
- Figure 7.2.** Structures of azobenzene terminally functionalized with polar (left) NO<sub>2</sub> functional group and (right) CF<sub>3</sub> functional groups. Introduction of dipole to the *trans* conformation of the azobenzene moiety will help elucidate the effect of dipole moment on the photoisomerization cross sections of the molecules when

assembled on solid substrates and the effects on the work function of the metal before and after isomerization .....159

**Figure 7.3.** Structures of the dihydroazulene-functionalized molecule (in its closed form, left) and vinylheptafulvalene (in its open form, right) studied.....160

**Figure 7.4.** A) Structure of a surface-bound rotaxane. Initially, the ring docks at the TTF station, shown in green. Upon oxidizing the TTF unit at 0.53 V, the ring shuttles to the red DNP unit (blue arrow). Subsequent reduction of the TTF unit propels the ring back to the original position (red arrow). B) Three STM images (initial, after oxidation, and after reduction) superimposed on each other show the translation of the rings on the rotaxane molecules shuttling between the DNP and TTF stations. The blue arrows indicate the motion of the ring after the oxidation step and the red arrows indicate the motion after the reduction step. C) Histograms depicting the displacements of the protrusions in STM at equilibrium potentials of 0.12 V and 0.53 V (top). The displacement of rings after the oxidation step showing a range of 0-55 Å with a root mean square (rms) displacement of 20 Å and after the reduction step with a rms displacement of 16 Å (bottom).....161

**Figure 7.5.** A) Schematic of surface-bound rotaxanes. B) Deflections of the cantilever after reduction and oxidation sweeps. Bare cantilever deflection in the upward direction due to perchlorate adsorption during the forward sweep, and perchlorate desorption during the backward sweep (red). Control experiments with alkanethiols (pink) and molecules *without* the rings (green) blocked some of the

ion adsorption/desorption (more for the higher quality alkanethiol monolayer). Cantilever assembled with functional rotaxanes showed upward deflection at low potential due to some ion adsorption and downward deflection once a potential is reached where the TTF unit oxidizes, indicating the onset of ring shuttling and hence stress on the substrate .....163

**Figure 7.6.** A) Structure of polyrotaxane (5NP[4]R) functionalized with dithiol tethers in order to enable adsorption to Au. B) Scanning tunneling microscope image of isolated single molecules of 5NP[4]R showing the varied size distribution of rotaxane molecules indicating that the molecular thread is not rigid. C-F) High-resolution images of isolated single molecules showing a curved feature indicating that the molecular thread is not rigid and that the molecules orient themselves in bent conformations when adsorbed on a metal surface. Imaging conditions:  $V_s = -1.0$  V and  $I_t = 2$  pA .....165

**Figure 7.7.** A) Structure of a longer polyrotaxane (7NP[5]R) functionalized with dithiol tethers. B, C) Scanning tunneling microscope images of isolated single molecules of 7NP[5]R showing the variation in feature size. D, E) High-resolution images showing the preferred looped orientation of single molecules. Imaging conditions:  $V_s = -1.0$  V and  $I_t = 2$  pA .....166

**Figure 7.8.** Structure of a [4]rotaxane **3R**.3PF<sub>6</sub> molecule (designated as ***n*R**.*n*PF<sub>6</sub>, where *n* is equal to the number of  $-\text{CH}_2\text{NH}_2^+\text{CH}_2-$  recognition sites) with thioether functionality .....167

## LIST OF ABBREVIATIONS

AFM	atomic force microscope(y)
B3LYP	Beck, three-parameter, Lee-Yang-Parr
C10	decanethiol
C12	dodecanethiol
CBPQT	cyclobis(paraquat- <i>p</i> -phenylene)
DFT	density functional theory
DHA	dihydroazulene
DNP	dioxynaphthalene
DTB	4,4'-di- <i>tert</i> -butyl
FF	face-to-face
FS	face-to-side
FIB	focused ion beam
HOMO	highest occupied molecular orbital
LB	Langmuir-Blodgett
LUMO	lowest unoccupied molecular orbital
MIM	mechanically interlocked molecules
OPE	oligo(phenylene ethynylene)
SAM	self-assembled monolayer
SERS	surface-enhanced Raman spectroscopy
STM	scanning tunneling microscope(y)
SS	side-to-side
TTB	3,3',5,5'-tetra- <i>tert</i> -butyl



TTF	tetrathiafulvalene
UHV	ultrahigh vacuum
UV	ultraviolet
VHF	vinylheptafulvene
1D	one-dimensional
2D	two-dimensional
3D	three-dimensional
1R	single-row
2R	double-row
cm	centimeter
$h$	Planck's constant
h	hour
I	current
M	molar
min	minute
mM	millimolar
mW	milliwatt
nm	nanometer
rms	root mean square
s	second
$\alpha$	polarizability
$\beta$	conductivity
$\lambda$	wavelength

$\nu$	frequency
$\phi$	work function
$\text{\AA}$	Ångström

## Acknowledgments

My roommate, Benjamin Smith, over the recruitment weekend at Penn State asked me “So, who are *you* going to talk to today?” “Paul Weiss,” I replied. He followed up with “And?” “That’s it,” I said. I applied to and visited Penn State just because of Professor Paul S. Weiss. Words cannot describe how grateful I am to Paul. He has not been just a thesis advisor for me; he has been a father figure in whom I could confide every detail of my life. He taught me how to speak, to write, and to think science. The constant flow of information when one interacts with him is overwhelming. I cannot count how many ideas worth Ph.D. dissertations come out of the conversations with him that last hardly more than a few minutes! Paul, I am extremely grateful to you for giving me the opportunity to work for and beside you. I am honored and proud to say that I have graduated from your lab.

My sincere thanks to Professor Kendall N. Houk, who challenged me to think outside the box. Thank you for the valuable discussions and contributions that helped me improve myself as a scientist. To my committee members, Professor James Gimzewski, one of the key figures who inspired me to pursue my thesis in nanoscale science and measurements, and Professor Bruce Dunn, who has been more than willing to guide me when I transitioned from Penn State to UCLA. Sincere thanks to my collaborators Profs. James Tour, Lasse Jensen, Yang Yang, Mogens Nielsen, and Fraser Stoddart. Thank you for entertaining our ideas and helping us understand the fundamentals of molecular behavior at nanoscale.

I am thankful for having had the pleasure of working alongside a wonderful group of scientists; Dr. Ajeet Kumar, Dr. Yue Bing Zheng, Jeffrey Schwartz, Dr. John Payton, Dr. Seth Morton, Dr. Shelley Claridge, Dr. Choong-Heui Chung, Tze-Bin Song, Yang Cao, John Thomas,

and all Weiss group members past and present. I thank the National Science Foundation funded Material Science Research and Engineering Center (MRSEC) at Penn State, the Department of Energy (grant no. DE-FG02-07ER15877), The Kavli Foundation, Penn State Department of Chemistry, Department of Chemistry and Biochemistry at UCLA, and the California Nanosystems Institute for their financial support that helped bring this work to fruition.

My amazing and wonderful family – without you, I would have not been where I am now. Dad, you have worked so hard to provide me with everything for which I ever wished. You sacrificed your happiness on countless occasions to see to it that your children were happy first. You have made me who I am today. We love you. Mom, your encouragement and your unconditional love and affection toward me have been a constant source of motivation and desire to succeed. You made sure that I always had nothing but the best ever since I was a baby. Love you. My elder sister Vijaya, you are the best sibling one could ever have. Thank you for all the love and thank you for being such a wonderful human being. My younger sister Rajini, you were my best friend growing up. Thank you for your support, encouragement, and love. Lastly, my wife, my love, my soul, and my best friend, Bhavya. Without your support, motivation, and unconditional love through the toughest of times, I would never have been able to accomplish this goal. Here's to you and our eternal happiness. I love you.

Previous Publications and Contributions of Other Authors:

**Chapter 1** is based on a manuscript submitted for publication in *Annual Review of Physical Chemistry*. The writing of this review was a collaborative effort with Dr. Shelley A. Claridge, Dr. Yue Bing Zheng, and Prof. Paul S. Weiss.

**Chapter 3** is a manuscript in preparation, which should be submitted shortly after this dissertation is filed. Currently, the paper is as follows: Pathem, B. K.; Kumar, A. S.; Cao, Y.; Zheng, Y. B.; Corley, D. A.; Ye, T; Aiello, V. J.; Crespi, V. H.; Houk, K. N.; Tour, J. M.; Weiss, P. S. “Coordinated Driven Motion of Assembled One-Dimensional Chains of Tethered Functional Molecules.” *TBD 2012*. Professor Paul Weiss, Dr. Ajeet Kumar, and I designed the project. Dr. David A. Corley from Professor James M. Tour’s group synthesized the molecule, Dr. Ajeet Kumar and I performed the scanning probe measurements, Yang Cao from Professor Kendall N. Houk’s group performed major part of theoretical simulations, while I performed initial theoretical calculations, Victor J. Aiello performed control STM measurements, and Yue Bing Zheng, Tao Ye, Vincent H. Crespi helped with manuscript preparation. This work was supported by the Department of Energy (#DE-FG02-07ER15877), the Penn State Center for Nanoscale Science (a National Science Foundation funded Materials Research Science and Engineering Center), and the Kavli Foundation.

**Chapter 4** is a manuscript in preparation, which should be submitted shortly after this dissertation is filed. Currently the paper is as follows: Zheng, Y. B.; Pathem, B. K.; Payton, J. L.; Bob. B.; Kumar, A. S.; Chung, C-H.; Yu, B. C.; Yang, Y.; Jensen, L.; Tour, J. M.; Weiss, P. S. “Directed Assembly of Precise Supramolecular Structures to Tune Their Dipole-Dipole Interactions.” *TBD 2012*. Professor Paul Weiss, Dr. Yue Bing Zheng, and I designed the project. Dr. Yue Bing Zheng and I performed the surface-enhanced Raman measurements; I performed scanning probe measurements, Dr. John L. Payton from Professor Lasse Jensen’s group performed the theoretical simulations, Dr. Byung-Chan Yu from Professor James M. Tour’s group synthesized the molecule, Brion Bob and Dr. Choong-Heui Chung from Professor Yang Yang’s group helped with Raman measurements, and Dr. Ajeet S. Kumar helped with

manuscript preparation. This work was supported by the Department of Energy (Grant No. DE-FG02-07ER15877), the Penn State Center for Nanoscale Science (a NSF-supported Materials Research Science and Engineering Center), and the Kavli Foundation.

**Chapter 5** has been published and is adapted with permission from Pathem, B. K.; Zheng, Y. B.; Payton, J. L.; Song, T-B.; Yu, B-C.; Tour, J. M.; Yang, Y.; Jensen, L.; Weiss, P. S. “Effect of Tether Conductivity on the Efficiency of Photoisomerization of Azobenzene-Functionalized Molecules on Au{111}.” *J. Phys. Chem. Lett.* **2012**, 3, 2388-2394. Copyright © 2012 American Chemical Society. Professor Paul Weiss and I designed the project. Dr. Yue Bing Zheng and I performed the surface-enhanced Raman measurements; I performed scanning probe measurements, Dr. John L. Payton from Professor Lasse Jensen’s group performed the theoretical simulations, Dr. Byung-Chan Yu from Professor James M. Tour’s group synthesized the molecule, and Tze-Bin Song from Professor Yang Yang’s group helped with Raman measurements. This work was supported by the Department of Energy (Grant No. DE-FG02-07ER15877), the Penn State Center for Nanoscale Science (a NSF-supported Materials Research Science and Engineering Center), and the Kavli Foundation.

**Chapter 6** is based on a manuscript that has been submitted to Nano Letters and is currently in review. Currently, the paper is as follows: Pathem, B. K.; Zheng, Y. B.; Morton, S.; Petersen, M. A.; Chung, C-H.; Yang, Y.; Jensen, L.; Nielsen, M. B.; Weiss, P. S. “Photoreaction of Matrix-Isolated Dihydroazulene-Functionalized Molecules on Au{111}.” *TBD* **2012**. Professor Paul S. Weiss, Professor Mogens B. Nielsen, and I designed the project. I performed the surface-enhanced Raman measurements, I performed scanning probe measurements, Dr. Seth Morton from Professor Lasse Jensen’s group performed the theoretical simulations, Dr. Michael A. Petersen from Professor Mogens B. Nielsen’s group synthesized the molecule, and

Dr. Choong-Heui Chung from Professor Yang Yang's group helped with Raman measurements. This work was supported by the Department of Energy (Grant No. DE-FG02-07ER15877), the Penn State Center for Nanoscale Science (a NSF-supported Materials Research Science and Engineering Center), and the Kavli Foundation.

## **VITA**

1998-2002	Bachelor of Science, Pharmacy (Honors), Birla Institute of Technology and Science (BITS), Pilani.
2001-2002	Undergraduate Research Assistant, Department of Pharmacy, BITS, Pilani.
2005-2007	Research and Teaching Assistant, Sam Houston State University (SHSU), Huntsville, Texas.
2005-2007	Master of Science, Chemistry, SHSU.
2007-2008	Teaching Assistant, The Pennsylvania State University (PSU), State College, Pennsylvania.
2008-2009	Research Assistant, PSU.
2009-2012	Research Assistant, Department of Chemistry and Biochemistry, University of California, Los Angeles (UCLA), Los Angeles, California.



## LIST OF PUBLICATIONS AND PRESENTATIONS

Takami, T.; Ye, T.; **Pathem, B. K.**; Arnold, D. P.; Sugiura, K.-i.; Bian, Y.; Jiang, J.; Weiss, P. S. “Manipulating Double-Decker Molecules at the Liquid-Solid Interface.” *J. Am. Chem. Soc.* **2010**, *132*, 16460-16466.

**Pathem, B. K.**; Weiss, P. S. (2010, March), “Controlled Motion of Molecular Motors in Precise Nanoscale Assemblies.” Poster presentation at the American Chemical Society National Meeting, San Francisco, California.

Zheng, Y. B.; **Pathem, B. K.**; Hohman, J. N.; Weiss, P. S. “Functional Supramolecular Assemblies: First Glimpses and Upcoming Challenges.” Proceedings of the International Beilstein Symposium on Functional Nanoscience, 2010, Bozen, Italy, 1 (2011).

**Pathem, B. K.**; Weiss, P. S. (2011, April) “Design, Control, and Measurement of Molecular Assemblies.” Oral presentation at the Materials Research Society National Meeting, San Francisco, California.

Zheng, Y. B.; Payton, J. L.; Chung, C.-H.; Liu, R.; Cheunkar, S.; **Pathem, B. K.**; Yang, Y.; Jensen, L.; Weiss, P. S. “Surface-Enhanced Raman Spectroscopy to Probe Reversibly Photoswitchable Azobenzene in Controlled Nanoscale Environments.” *Nano Lett.* **2011**, *11*, 3447-3452.

**Pathem, B. K.**; Weiss, P. S. (2011, September) “Design, Control, and Measurement of Molecular Assemblies.” Oral presentation at the Jawaharlal Nehru Center for Advanced Scientific Research, Bengaluru, India.

**Pathem, B. K.**; Zheng, Y. B.; Payton, J. L.; Song, T.-B.; Yu, B.-C.; Tour, J. M.; Yang, Y.; Jensen, L.; Weiss, P. S. “Effect of Tether Conductivity on the Efficiency of Photoisomerization of Azobenzene-Functionalized Molecules on Au{111}.” *J. Phys. Chem. Lett.* **2012**, *3*, 2388-2394.

Zheng, Y. B.; **Pathem, B. K.**; Hohman, J. N.; Thomas, J. C.; Kim, M. H.; Weiss, P. S. “Photoresponsive Molecules in Well-Defined Nanoscale Environments.” *Adv. Mater.* **2012**, in press, DOI: 10.1002/adma.201201532.

**CHAPTER 1**  
***INTRODUCTION***

## 1.1 INTRODUCTION

Molecular switches and motors, which change their structural, electronic, and/or optical properties in response to external stimuli, represent the ultimate limit of miniaturization for creating functional molecular devices.<sup>1-3</sup> While progress in chemical synthesis has created a broad range of switches and motors, measuring and understanding the physics and chemistry of switching molecules has proved more challenging.<sup>4-7</sup> Most studies of molecular motors and switches have been carried out in solution, meaning molecules are randomly distributed and oriented, and cannot be addressed individually.<sup>1,2,8,9</sup> Placement, addressability, and cooperative operation become possible once switches and motors are assembled on solid surfaces.<sup>5,10-14</sup> However, some molecules function differently on surfaces,<sup>15</sup> making it important to characterize the effects of assembly on molecular structure, arrangement, and function.

Fundamental experimental and theoretical studies of a broad range of molecular switches and motors have laid the groundwork for early applications in molecular devices.<sup>5-7,12-14,16-18</sup> Active molecules are first assembled on surfaces using one of several existing methods,<sup>19-21</sup> then manipulated and characterized using techniques including optical spectroscopy, scanning tunneling microscopy (STM), and/or atomic force microscopy (AFM).<sup>22</sup> Molecular simulation and theoretical analysis tools incorporating surface effects have been developed to complement experimental studies.<sup>23-25</sup>

As a preface to the thesis, I discuss some of the most commonly studied molecular switches and motors, surface assembly methods, techniques to monitor and to understand switching, and emerging applications.

### **1.1.1 ASSEMBLY OF MOLECULAR SWITCHES AND MOTORS ON SURFACES**

Molecular switches and motors can be assembled as Langmuir-Blodgett (LB) monolayers, self-assembled monolayers (SAMs) deposited either in vacuum or from solution, and single molecules and assemblies in well-defined nanoscale environments.<sup>4,13,15,26,27</sup> Here, we focus primarily on monolayers self-assembled from solution, since this method can be used to form dense, ordered structures suitable for characterization and directed coupling between molecules. An important subset of these assembly techniques distribute switches or motors in a preexisting background monolayer, resulting in a controlled nanoscale environment around the active molecule and facilitating characterization of switching and motion under ambient conditions.

### **1.1.2 SELF-ASSEMBLED MONOLAYERS**

Self-assembled monolayers form when molecules spontaneously adsorb on a surface through either covalent or noncovalent interactions. Early work by Allara, Nuzzo, Whitesides, and others focused on SAMs of alkanethiols on gold.<sup>26,28,29</sup> From ethanolic solutions (typically at concentrations near 1 mM), thiols organize rapidly (within seconds) on gold by forming covalent bonds between the thiol head group and the gold surface, exposing the tail groups in ordered lattices. Although SAMs can be assembled on surfaces including metals (such as Au, Ag, Cu, Pt, and Pd),<sup>26</sup> semiconductors (including Si and Ge),<sup>30-32</sup> insulators,<sup>33</sup> glass,<sup>34-36</sup> nanoparticles,<sup>37,38</sup> and porous materials,<sup>39</sup> gold is a widely used substrate because it is commercially available, easily forms bonds to thiols, and is otherwise relatively inert.

Although thiols are commonly used to form monolayers on gold, amines, selenols, thioacetyls, and other attachment chemistries may also be used.<sup>26,29,40</sup> However, even for the widely used Au–S attachment chemistry, the exact surface bonding arrangement is widely debated,<sup>41</sup> highlighting the critical importance of understanding molecule–surface contact for the molecular switches and motors discussed here.

In addition to linear backbones, bulkier and more rigid backbones such as adamantanes and carboranes<sup>42</sup> have also been explored as means to display chemical functional groups on surfaces. These molecules are also expected to be important in the context of molecular switches, since the tethering group has been shown to play important roles in both molecule-surface coupling and determining the steric freedom available for switching and other motion.

### **1.1.3 SINGLE MOLECULES AND ASSEMBLIES IN CONTROLLED ENVIRONMENTS**

Individual switches and motors can couple to their environments or to surrounding active molecules, changing their function.<sup>15,43-49</sup> Thus, it is important to be able to isolate individual molecules and controlled assemblies to measure their properties. One straightforward method is to isolate individual molecular switches and motors or their assemblies within well-ordered two-dimensional (2D) alkanethiolate SAM matrices.<sup>16,50-58</sup> Experimentally, this is achieved in one of two ways. Active molecules can be added to an existing film, resulting in selective deposition at defects in the SAM; these defects are the most reactive and sterically accessible sites on the surface. Alternatively, small amounts of the active molecule can be co-deposited with the matrix molecules, typically resulting in isolation of the active molecules within the domains of alkanethiolate domains. Annealing at elevated temperatures (~80 °C) can then be used to

organize the active molecules,<sup>59</sup> producing controlled (clustered or linear) assemblies.<sup>57,58</sup> When using the insertion method, active molecules can also be applied to the existing SAM using soft-lithographic stamps, leaving isolated molecules at defects in the stamped areas only.<sup>60</sup>

This host-guest system has a number of advantages. Isolated molecules can be probed individually<sup>61</sup> and their functional properties understood in relation to the immediate molecular environment. For some switch molecules, the ordered matrix reduces stochastic switching, making it easier to measure switching based on controlled stimuli.<sup>43,53</sup> The matrix can also be precisely designed to interact with molecules in the assembly, for instance by engineering hydrogen-bonding or dipole interactions with the active molecule.<sup>15,46,49</sup> The matrix can channel heat evolved from excitations and reactions, preventing thermal damage to the monolayer.<sup>62-65</sup> Finally, well-characterized SAMs provide spatial and electronic references for measurements of inserted molecules.<sup>16,43,46,47,49,50,53,55,60,66,67</sup>

## **1.2 MOLECULAR SWITCHES**

### **1.2.1 ELECTRONIC SWITCHES**

The discovery in 1977 that conjugated polymers such as polyacetylene can be electrically conductive<sup>68,69</sup> led to extensive research on molecular conductance, ranging from single molecules wired to metal electrodes<sup>22,43,46,53</sup> to bulk materials for solar cells.<sup>70</sup> Some conductive molecules can switch between high- and low-conductance states, making them candidates for molecular electronics (Fig. 1.1).

However, both conductance and switching properties depend critically on contact with electrodes as well as the details of molecular structure, conformation, and interactions with the environment, complicating their use in devices. It is also often necessary to distinguish between

several possible switching mechanisms, which is not straightforward due to challenges inherent in single-molecule measurements.<sup>22</sup> In this chapter, experimental and theoretical approaches to solving these problems will be discussed, focusing on functionalized benzenes and on larger conjugated oligo(phenylene ethynylene) switches as examples.

## **1.2.2 CONDUCTANCE DEPENDS STRONGLY ON CONTACTS AND ENERGY LEVEL ALIGNMENT**

The physical, chemical, and electronic contact between the molecular switch and the metal electrode is critical to understanding molecular conductance.<sup>71-73</sup> Calculations show that when a benzenedithiol molecule is bound to metal electrodes, significant charge transfer occurs, shifting the molecular energy levels. The offset in energy between the resulting molecular orbitals and the metal Fermi level is one of the key quantities determining molecular conductance.

Spatial extents of the molecular orbitals are also important. Calculations for benzenedithiol<sup>74</sup> indicate that the highest occupied molecular orbital (HOMO) and lowest unoccupied molecular orbital (LUMO) are predominantly localized on the molecular backbone, whereas the HOMO-1 states are localized on the sulfur end groups.

Polarizability, the deformation of a molecule's (or assembly's) electrons in response to an electric field, is a convenient readout for molecule–substrate contact. Conjugated switch molecules such as oligo(phenylene ethynylene) are 2-6 times as polarizable as unconjugated alkanethiols.<sup>67</sup> However, binding to a metal surface further increases their polarizability due to coupling with substrate electrons.

Conductive molecules may be attached to metal electrodes using a variety of functional groups. Thiols (-SH) are most common, although other groups such as amines (-NH<sub>2</sub>), selenols (-SeH), and nitriles (-CN) are also used. The linker used can strongly impact molecular conductance. Theoretical calculations by Ratner and coworkers predict conductance differences of two orders of magnitude for *para*-difunctionalized benzenes between gold electrodes based on the functionality of the linker, due to both shifts in energy levels and spatial extents of the HOMOs and LUMOs.<sup>73</sup>

Experimental methods can also be used to measure differences in conductance based on attachment group.<sup>40,75,76</sup> Weiss and coworkers have performed STM measurements and demonstrated that for saturated chains, thiolate molecules are more conductive than their selenolate counterparts,<sup>76</sup> based on differences between calculated and apparent heights. While thiols are physically 0.2 Å shorter than the equivalent selenolates of the same alkyl chain length as part of a SAM, thiols appear 0.4 Å more protruding in STM images than the equivalent selenolates. Since STM images are a convolution of topography and electronic effects, this corresponds to a ~2.5-fold difference in contact conductance.

For a range of backbones, larger conductances of thiols vs. selenolates have been predicted in both directions.<sup>76-82</sup> Joachim and coworkers attributed this apparent conflict to orbital alignment changes based on the backbone interactions with the contact electronic structure.<sup>83</sup> Venkataraman, Hybertsen, and coworkers have since demonstrated that substitutions along the molecular backbone (*i.e.*, not in contact with the electrodes) do indeed impact conductance.<sup>84-88</sup> In substituted benzenes attached to gold electrodes via amine linkers, electron-donating groups increased the energy of the HOMO, increased the conductance by aligning the HOMO with the



Fermi level of the metal. When electron-withdrawing groups were attached, the HOMO energy level was lowered, decreasing conductance.<sup>86</sup>

Solvent can also play a role – in the diaminobenzene system described above, changes in solvent changed conductance by up to 50%,<sup>89</sup> attributed to solvent molecules binding to low coordination sites around the metal-molecule junction, increasing the Au contact work function and impacting energy level alignment.

Molecule-surface contact is also impacted by the geometry of the binding site. Thiolates have complicated binding to Au{111} that has been the subject of controversy. In some cases, thiolates bind to Au adatoms, which also have some mobility on the surface.<sup>48,90,91</sup> Changes in binding site result in significant changes in conductance.<sup>40,72,92,93</sup> Weiss and coworkers demonstrated experimentally that adamantaneselenolates bound to three-fold hollow sites have higher contact conductances than those at bridge sites.<sup>40</sup> Surface reconstruction also induces changes to molecular adsorption sites and can result in changes in contact conductances.

In the tunneling regime, molecular conductance can be described by the equation  $G = Ae^{-\beta n}$ ,<sup>76</sup> where A is constant, n is the length of the molecule, and  $\beta$  is an exponential tunneling decay factor that depends on the alignment of the molecular energy levels and the Fermi level of the substrate. For saturated alkanethiols,  $\beta = 0.5\text{--}1.0/\text{\AA}$  depending on the linker functionality.<sup>94</sup> More conductive molecules have lower  $\beta$  values: Chidsey and coworkers found  $\beta \approx 0.6/\text{\AA}$  for ferrocene-terminated oligo(phenylene ethynylene)s,<sup>95</sup> Venkataraman and coworkers found  $\beta = 0.4/\text{\AA}$  for diaminopolyphenyls,<sup>85</sup> and thiol- and isocyanide-functionalized oligoacenes have  $\beta \approx 0.5/\text{\AA}$ .<sup>96</sup>

Although conductance usually decreases with molecular length, exceptions exist. Ratner proposed that in the intermediate regime between the coherent superexchange range<sup>97</sup> and incoherent hopping range, conductance is nearly independent of length.<sup>98</sup> Tao and coworkers found experimentally that the conductances of oligothiophenes *increase* going from the three-ring to the four-ring molecule, which they attributed the HOMO shifting closer to the Fermi level for the longer molecule.<sup>99</sup>

### 1.2.3 OLIGO(PHENYLENE ETHYNYLENE)S AND PROPOSED SWITCHING MECHANISMS

Oligo(phenylene ethynylene)s (OPEs) are another well-studied class of extended  $\pi$ -conjugated systems that undergo reversible switching between different conductance states.<sup>24,45,47-49,100-119</sup> Allara and coworkers demonstrated that these functional molecules show several orders of magnitude higher conductance than saturated alkanethiols when attached to conductive electrodes.<sup>107</sup> The switching behavior of OPE has been well documented using a variety of techniques.<sup>47-49,106,112,116,120,121</sup> Several possible switching mechanisms were proposed, including rotation of functional groups,<sup>78</sup> twisting of the conjugated backbone,<sup>122</sup> reduction of functional groups,<sup>24,121</sup> intermolecular interactions,<sup>123</sup> and changes in the hybridization of metal molecule bond.<sup>43,44,47,124</sup> Molecular design variations and measurements were used to test all of these possibilities, by synthesizing molecules that could and could not exhibit each of the proposed mechanisms, ultimately leading to the understanding that switching occurs via hybridization change at the Au-S interface.

Both reduction and rotation of attached functional groups can affect electronic energy levels of the molecules, one possibility for conductance switching. Seminario *et al.* proposed

reduction as a mechanism for switching in amino- and nitro- functionalized molecules. Reduction of OPE occurs at  $\sim 1.7$  V at 0 K,<sup>24</sup> spatially extending the LUMO, which could increase conductance. Lang and coworkers suggested the alternative possibility that rotation in the amine or nitro groups alters in the HOMO–LUMO gap<sup>78</sup> to change conductance. However, in STM measurements by Weiss and coworkers, OPE switched under imaging potentials ( $-1$  V sample bias) much lower than the reduction potential and also without any tunneling current, when the tip was withdrawn from the surface, out of tunneling range. Figure 1.2A shows the structure of the molecule and high-resolution STM images of the molecule in its ON state (top) and OFF state (bottom).<sup>43</sup>

Other groups suggested that conductance switching arises from rotation of the phenyl rings in the OPE backbone,<sup>95,122,125</sup> with maximum conductance when all three rings are parallel with continuous  $\pi$ -orbital overlap, and decreased conductance when they are rotated with respect to each other, decreasing overlap (as for crossed polarizers). It was proposed that by attaching bulky functional groups to the phenyl rings, rotation could be hindered.<sup>122</sup> Barriers for such rotation at room temperature depend strongly on the environment around the molecules:  $\sim 0.04$  eV for free rotation and nearly two orders of magnitude greater ( $\sim 1.6$  eV) when restricted by a tightly packed matrix.<sup>24,123</sup> However, stochastic switching was observed for individual phenanthrene molecules (with fused rings) in an octanethiolate SAM matrix (Fig. 1.2B).<sup>49,126</sup>

Interactions between switches and the matrix have also been investigated as they relate to controlling switching. Introducing a nitro group (or other functionality) to the backbone of the OPE molecule increases the molecular dipole moment. Thus, the molecule experiences stronger electrostatic forces from electric field due to the applied bias between STM tip and the substrate.<sup>47</sup>

Nitro-OPE aligned normal to the surface when a positive sample bias was applied, protruding from the matrix. However, the molecules tilted when a negative sample bias was applied, decreasing their apparent height in STM images (Fig. 1.2C). Since the tilted molecules also switch to low-conductance (OFF) states, both physical and electronic factors contribute to the decrease in apparent height. Importantly, the use of a matrix containing amide functional groups allowed the OPE to hydrogen bond with the matrix, stabilizing the conductance states and decreasing stochastic switching. Thus, by engineering interactions between the switch and the matrix it is possible to achieve a higher degree of control over molecular switching.

Lindsay and coworkers investigated dithiol-functionalized OPE molecules with nanoparticles attached to one of the thiol terminus while the other end of the molecule was attached to the underlying Au surface. They proposed that the conductance switching observed in their STM measurements was due to the detachment of OPE molecules from the surface due to a “blinking” mechanism of the Au-thiol bond.<sup>120</sup> However, their mechanism required the nanoparticles to be covalently bound to the substrate in the high conductance state and detached from the surface in the low conductance state. Weiss and coworkers have shown that nanoparticles not tethered to the substrate can be differentiated from those that are, and the former are easily swept away by the STM tip.<sup>61</sup> Thus, we discount this detachment mechanism, but not that hybridization changes fulfill the same role of changing conductance through bonding changes.

Interactions with neighboring switch molecules (in contrast to interactions with the matrix) were also proposed to play a role in conductance switching.<sup>123</sup> Since single molecules were shown to function as switches, this mechanism could be ruled out.<sup>43,49</sup>

Since thiolates on Au{111} can migrate on the surface, particularly near surface defects, such migration was also investigated as a possible switching mechanism. Thiolated OPEs adsorbed on Au{111} near atomic step edges and vacancy islands can move up and down at the edge (Fig. 1.2D).<sup>48</sup> However, individual molecules near step edges nonetheless exhibited ON and OFF states both above and below the edge.<sup>48</sup>

The mechanism consistent with the STM measurements is a hybridization change at the S-Au interface. Molecules oriented normal to the surface have *sp* hybridization with the substrate; hybridization changes to *sp*<sup>3</sup> if a tilted conformation is adopted.<sup>124</sup> In contrast with reduction or rotation in a packed matrix, hybridization changes have a much lower activation energy (~0.1 eV)<sup>127</sup> consistent with switching under STM imaging conditions. Additional mechanistic possibilities exist for molecules unrestricted by surrounding matrices.

In the OPE switching measurements described above, the molecule is covalently bound to only one electrode – the substrate. It is also possible to perform break junction measurements in which the molecule is thiolated on both ends, and covalently bound to both electrodes. This configuration has been used to measure electronic spectra for symmetrically and asymmetrically functionalized OPE molecules, which have symmetric and asymmetric current-voltage (I-V) curves, respectively.<sup>128</sup> Break junction measurements also demonstrated that the position of the thiol on the terminal phenyl ring impacts conductance. Molecules thiolated in the *para* position (at the end of the long molecular axis) were more conductive than those thiolated at the *meta* position (to one side of the axis).<sup>129</sup>

All of the factors discussed above (anchoring chemistry, backbone structure and functionalization, adsorption geometry, metal composition, and neighboring molecules) affect

HOMO and LUMO alignment with respect to the metal Fermi level and therefore conductance. Due to this complex interplay between molecular structure and conductance, designing and optimizing new switch molecules and their contacts is not straightforward. If understood and made predictable, these factors will ultimately provide useful degrees of control over switch assembly and function.

### 1.3 PHOTOCROMIC SWITCHES

Photochromic switches undergo reversible conformational changes when exposed to light of specific wavelengths. Typically, two conformers have different energies and different absorption spectra, so if the molecule has been switched into its higher energy form using light, it can either relax back thermally, or be switched back by light of a different wavelength.<sup>130</sup> Since their discovery in the late 1880s, studies of photochromic molecules have explored an increasing range of species and function; the most-studied classes include spiropyran, spirooxazine, diarylethene, azobenzene, and quinones.<sup>4,8,13</sup> Immobilizing photochromic molecules on surfaces presents special challenges since the addition of an anchoring group must not strongly impact the stability of either conformation, or the overlap of their absorption spectra.<sup>15</sup>

Since its synthesis and initial photochemical uses in 1950s, azobenzene has been one of the most widely studied molecular switches.<sup>53,131-143</sup> It has been used in porous materials to control release of absorbed molecules.<sup>144,145</sup> Because it has been extensively characterized both in solution and on surfaces, it provides a useful example of how the physical properties of such molecules are both studied on and impacted by surfaces. In its thermodynamically favorable state, azobenzene adopts a planar *trans* conformation. When exposed to ~365 nm UV irradiation (3.4 eV), it switches to a three-dimensional *cis* conformation. Two possible switching mechanisms exist. One is an inversion mechanism: a forbidden n-  $\pi^*$  excitation ( $S_0$  to  $S_1$ ),<sup>146</sup> with

in-plane bending of the C–N=N angle from  $\sim 120^\circ$  to  $\sim 240^\circ$ . The other is a rotation mechanism: an allowed  $\pi\text{--}\pi^*$  excitation ( $S_0$  to  $S_2$ ), resulting in out-of-plane rotation of the N=N bond (Fig. 1.3).<sup>146,147</sup> In solution, the absorption spectrum of the *trans* isomer exhibits a strong band at 318 nm due to the allowed  $\pi\text{--}\pi^*$  transition, and a weaker band at 440 nm due to the forbidden  $n\text{--}\pi^*$  transition.<sup>23,148–150</sup> Theoretical and experimental studies suggest both processes are possible, and that their relative probabilities change when the molecules are assembled on solid substrates.<sup>18,146,151–153</sup> Azobenzene can revert to its *trans* conformation either via thermal relaxation or when exposed to visible light of  $\sim 420$  nm (2.95 eV).<sup>146,153,154</sup>

The photophysics of azobenzene isomerization is unusual. When azobenzene relaxes following excitation, photon emission can occur from either  $S_1$  or  $S_2$  excited states, in violation of Kasha's rule, which states that molecules excited to the  $S_2$  state should first relax to the  $S_1$  state before emitting a photon as they drop to the ground ( $S_0$ ) state. Quantum yields for excited azobenzene in solution have been reported in the range of 0.2<sup>152</sup> to 0.36<sup>132</sup> for the  $S_1 \rightarrow S_0$  transition and 0.09<sup>152</sup> to 0.2<sup>132</sup> for the  $S_2 \rightarrow S_0$  transition. The implied uniqueness of the reaction mechanism via the  $S_2$  excited state has driven a number of studies of azobenzene in the gas phase, in solution, and when assembled on solid substrates.<sup>18,25,53,138,140,141,153,155–163</sup>

### 1.3.1 PHOTOCROMIC SWITCHES FUNCTION DIFFERENTLY ON SURFACES

While azobenzene readily photoisomerizes in both gas and solution phases,<sup>100,146,148,151</sup> adsorption directly on conductive surfaces quenches isomerization,<sup>160,164,165</sup> unless the molecule is electronically decoupled from the surface. Azobenzene adsorbs relatively flat on Au{111} surfaces, with both benzene groups associated with the surface. A number of decoupling strategies have been explored, including the addition of bulky legs to elevate the molecule, the

addition of a thin insulating layer separating the switch from the metal surface, the addition of an insulating SAM with switches covalently tethered within the domains of SAM, and the use of semiconducting surfaces.<sup>7</sup>

Interactions between the molecules and the substrate play important roles. Most surface switching studies have been carried out on Au{111}, which is relatively inert and flat. Azobenzenes on the more reactive Cu{100} and even on the somewhat corrugated Au{110} surface do not isomerize under similar conditions,<sup>166</sup> although in some cases, specific experimental conditions can be chosen to achieve different types of switching, for instance by forming a bond to the Cu(100) surface.<sup>161</sup>

One widely used approach for reducing molecule-substrate coupling is the addition of bulky legs as spacers. Crommie and coworkers varied steric bulk by attaching either 4,4'-di-*tert*-butyl (DTB) or 3,3',5,5'-tetra-*tert*-butyl (TTB) legs to both ends of azobenzene (Fig. 1.4A).<sup>160</sup> Azobenzenes with bulky TTB legs were successfully decoupled from the surface and isomerized after illumination with UV light (375 nm, 90 mW/cm<sup>2</sup>) for 3 h. Unfunctionalized azobenzenes and those with fewer legs remained coupled to the surface and did not isomerize when irradiated. Characterization by STM allows direct observation of the conformational changes produced by switching in individual molecules. Each molecule initially appeared as a four-lobed feature (Fig. 1.4A) in its *trans* conformation. After isomerization one of the phenyl rings bent up from the surface, resulting in a greater apparent height (protruding feature in Fig. 1.4A, bottom).

Highlighting the complexity of the isomerization process, these conditions resulted in a different isomerization mechanism than that observed in solution, believed to proceed via formation of a hole in the *d*-band of the metal surface and subsequent transfer of an electron



from the HOMO.<sup>167</sup> Photoisomerization efficiency for surface isomerization was much lower than that in solution, possibly due to decreased lifetime of the surface-modified photoexcited state or steric hindrance from neighboring molecules.<sup>160</sup>

Morgenstern and coworkers employed a different decoupling strategy on Ag{111},<sup>168</sup> depositing a thin insulating layer of sodium chloride (NaCl) and irradiating for up to 18 h (Fig. 1.4B). *Trans-cis* photoisomerization was observed under these conditions and in this case was correlated to direct molecular photoexcitation rather than *d*-band excitation.<sup>168</sup> Photoswitching under these conditions was irreversible, although reversible switching was possible using tunneling electrons from the STM tip as discussed later.<sup>163</sup>

An alternative decoupling strategy was employed by Weiss and coworkers, using azobenzene molecules functionalized with a thiol tether on one end and deposited within domains of an alkanethiol SAM matrix on Au{111}.<sup>53</sup> This covalent attachment strategy enables measurements under ambient conditions, with the saturated tether decoupling the photochromic azobenzene moiety from the surface. Tuning the number of methylene units in the tether adjusts the height of the functional molecule relative to the surrounding matrix. When the azobenzene does not protrude from the SAM matrix, photoisomerization efficiency is reduced by steric hindrance. Switching under ambient conditions using this deposition method revealed higher photoisomerization cross sections (relative to the low-temperature UHV experiments discussed above) (Fig. 1.4C)<sup>53</sup> at low illumination intensities ( $\sim 10 \text{ mW/cm}^2$ ). Switching was reversible, with the *cis-trans* back photoreaction induced by illumination at visible wavelengths ( $\sim 450 \text{ nm}$ ,  $< 10 \text{ mW/cm}^2$ ).

Azobenzene isomerization has also been observed on semiconducting surfaces. Recently, Crommie and coworkers demonstrated photoisomerization of TTB-functionalized azobenzene on GaAs(110). Most interestingly, when the domains of azobenzene were irradiated with UV light for several hours, stripes of protruding features appeared in STM images (Fig. 1.4D),<sup>169</sup> in contrast with the random photoswitching observed on Au{111}. Switching was enhanced near domain and island edges, suggesting that stronger intermolecular interactions on GaAs(110) increase photoisomerization efficiency.

### 1.3.2 ISOMERIZATION ON SURFACES INITIATED BY TUNNELING ELECTRONS

In addition to imaging the isomerization of single-molecule switches, the STM probe tip can also be used to inject electrons, initiating switching. It is thereby possible to induce isomerization in unfunctionalized azobenzene associated directly with metal surfaces, which do not photoisomerize.<sup>18,141,163</sup> Kuk and coworkers deposited azobenzene on Au{111} and observed dumbbell-shaped features (Fig. 1.5A) for the *trans* conformer due to the two phenyl rings in the azo moiety oriented parallel to the surface.<sup>141</sup> During I-V measurements over a single molecule, abrupt increases in tunneling current were observed at  $\sim 1.5$  V bias along with changes in the shape of the azo feature to an extended oval, corresponding to the *cis* conformer. Two orientations have been proposed for the *cis* conformer, with either one or both phenyl rings bent away from the surface.<sup>143</sup>

Functionalized azobenzenes can also be switched electronically. Morgenstern and coworkers showed irreversible electron-induced switching of 4-dimethylaminoazobenzene-4-sulfonic acid deposited on Au{111}.<sup>170</sup> In STM images, two protrusions appear due to the end groups from each molecule separated by a shallow protrusion due to the N=N double bond. By

positioning the STM probe tip over the shallow feature (marked by a dot in the middle of the feature in Fig. 1.5B), they were able to inject electrons into the N=N double bond and to induce conformational changes in the molecule by ramping the bias voltage from 100 mV to 1 V; isomerization occurs at 900 mV, marked by the arrow in I-V curve (Fig. 1.5B).

Although switching in the above examples was not reversible, reversible electron-induced isomerization has been achieved using anilino-nitroazobenzenes.<sup>163</sup> Each molecular feature had three distinct protrusions in STM images, two due to the azobenzene moiety and one due to the aniline functionality. A threshold voltage of 650 meV was required for the *trans-cis* reverse isomerization. After isomerization, the molecules still showed two distinct features from the azo moiety, as opposed to the observations made by Kuk and coworkers, indicating in-plane isomerization. The molecules were then switched back to the *trans* conformation using the same procedure with a calculated threshold of 640 meV. Interestingly, the energies of the electrons that induce these changes are in all cases substantially lower than the energy required to isomerize the molecule via the S<sub>1</sub> excited state (~3.5 eV); they proposed that the conformational changes are induced through vibrational excitation in the ground state. Furthermore, inversion of one of the N-C bonds of the azo moiety is hypothesized as an isomerization pathway since the rotation mechanism requires one of the phenyl rings to lift away from the surface.

The yield of electron-induced isomerization varied depending on the substrate:  $7 \times 10^{-8}/e^-$  for amino-nitroazobenzene on Au{111} vs.  $2 \times 10^{-8}/e^-$  on NaCl/Ag(111). Yield also depends on end group functionality; substitution of an aniline substituent for an amino group decreases quantum yield more than an order of magnitude, to  $2 \times 10^{-9}/e^-$  on Au{111}.

### 1.3.3 ISOMERIZATION ON SURFACES INITIATED BY ELECTRIC FIELD

Azobenzene isomerization can also be induced using an electric field. Grill and coworkers assembled TTB-functionalized azobenzene on Au{111}, forming islands in which each molecule appears as a four-lobed feature in STM images (Fig. 1.5C).<sup>140</sup> The STM probe tip was positioned over the middle of the island, at heights of 4 - 36 Å, and 2 V pulses were applied for 20 s each. After ~10 pulses, several molecules had isomerized to the *cis* conformation, increasing in apparent height as one phenyl ring lifted away from the surface. Switching was reversible using voltage pulses of the same magnitude. Switching of an isolated single-molecule, however, was not possible due to the diffusion of the molecules on the surface.

Three observations are important in distinguishing field-induced switching from the tunneling-induced switching discussed above. First, molecules isomerized at tip-sample separations (>35 Å) at which the electron tunneling current is negligible. Moreover, there is a linear correlation between the threshold voltage (required to drive the isomerization) and the tip height, consistent with the reaction depending on the applied electric field. Finally, although the STM tip was held at the same point for each pulse, molecules as far away as 150 Å isomerized, well outside the area addressed by tunneling.

### 1.3.4 COUPLED ISOMERIZATION ON SURFACES

Since switching is strongly impacted by interactions with surrounding molecules, it is useful to understand whether and how nearby switches can couple. A key challenge in this case is to assemble switch molecules in an ordered fashion to facilitate coupling. To this end, we fabricated one-dimensional chains of azobenzene assembled at the domain boundaries of a host decanethiol SAM matrix, using self- and directed-assembly (see Chapter 3). The chains formed herringbone structures with center-to-center distances of ~4.5 Å between nearest neighboring

molecules.<sup>57</sup> The functional molecules appear as  $\sim 2.2$  Å protrusions with respect to the neighboring decanethiolate matrix. Applying a bias of 2 V at a single point in the chain produced concerted switching of all molecules in the chain, visible as a decreased apparent height ( $\sim 0.5$  Å vs.  $\sim 2.2$  Å) with respect to the surrounding matrix. Since the energy required for the concerted switching process is significantly lower than the photon energy required for photoisomerization, isomerization is hypothesized to occur via a negative ion resonance state during which the central N=N double bond is elongated. This would enable the molecule to follow the rotation mechanism to isomerize to the *cis* conformation. Chains revert back to the *trans* conformation via thermal relaxation.

## 1.4 SUMMARY AND THESIS OUTLOOK

The assembly, measurements, and applications of some commonly studied molecular switches and motors on surfaces have been discussed in this chapter. Transferring the molecular switches and motors onto surfaces is a critical step in elucidating and exploiting the properties of these functional molecules both individually and collectively. Much progress has been made in assembling and patterning molecular switches and motors on surfaces, ranging from LB monolayers to SAMs to isolated single molecules or assemblies in well-controlled environments. To this end, surface characterization tools have been designed and built to explore molecular and supramolecular function, yielding new insights into the effects of physical environment on mechanical motion and switching (see chapter 2). In chapter 3, I discuss the cooperative motion of molecular assemblies due to external stimuli, studied by high-resolution STM technique. In chapter 4, the analysis of intermolecular (and dipole-dipole) interactions of such assemblies using highly sensitive SERS, high-resolution STM, and density functional theory will be

elaborated. In chapter 5, the effect of tether conductance on the efficiency of photoisomerization of molecular switches will be discussed. We designed, novel molecular switch candidates that require less spatial freedom to isomerize when assembled on Au{111}. I discuss the assembly and high sensitivity measurements of such molecules in chapter 6. Finally, this thesis aims to help understand molecular function and motion at both the single-molecule level and at ensemble scales.

While most of the molecule-level measurements are limited to planar surfaces, the study of these adsorbed on curved surfaces, such as nanoparticles and porous materials are important for such applications as drug delivery and catalysis. These studies, however, require new measurement tools compatible with curved surfaces. With the initial demonstration of applications, and continued efforts in molecular design, assembly, and measurements from many fields, we anticipate elucidating the ultimate limits of miniaturization and cooperative action.

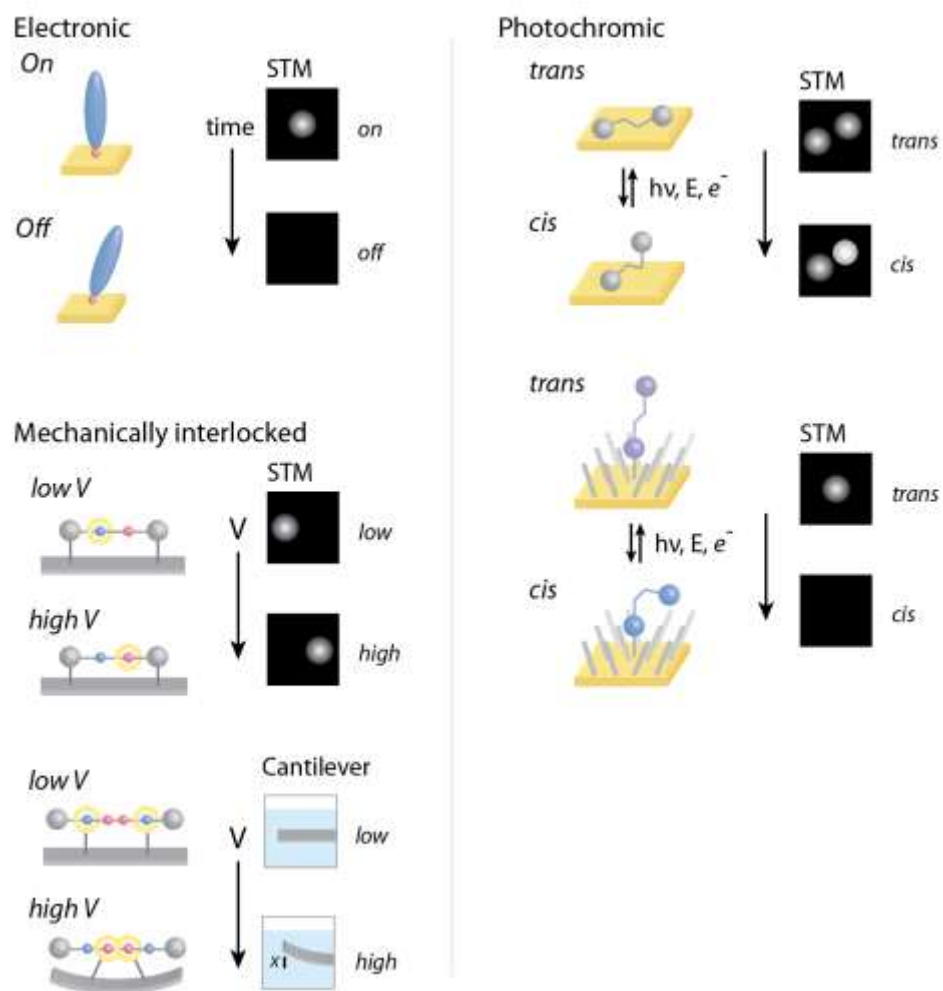


**Figure 1.1.** Overview of electronic, photochromic, and mechanically interlocked molecular switches.

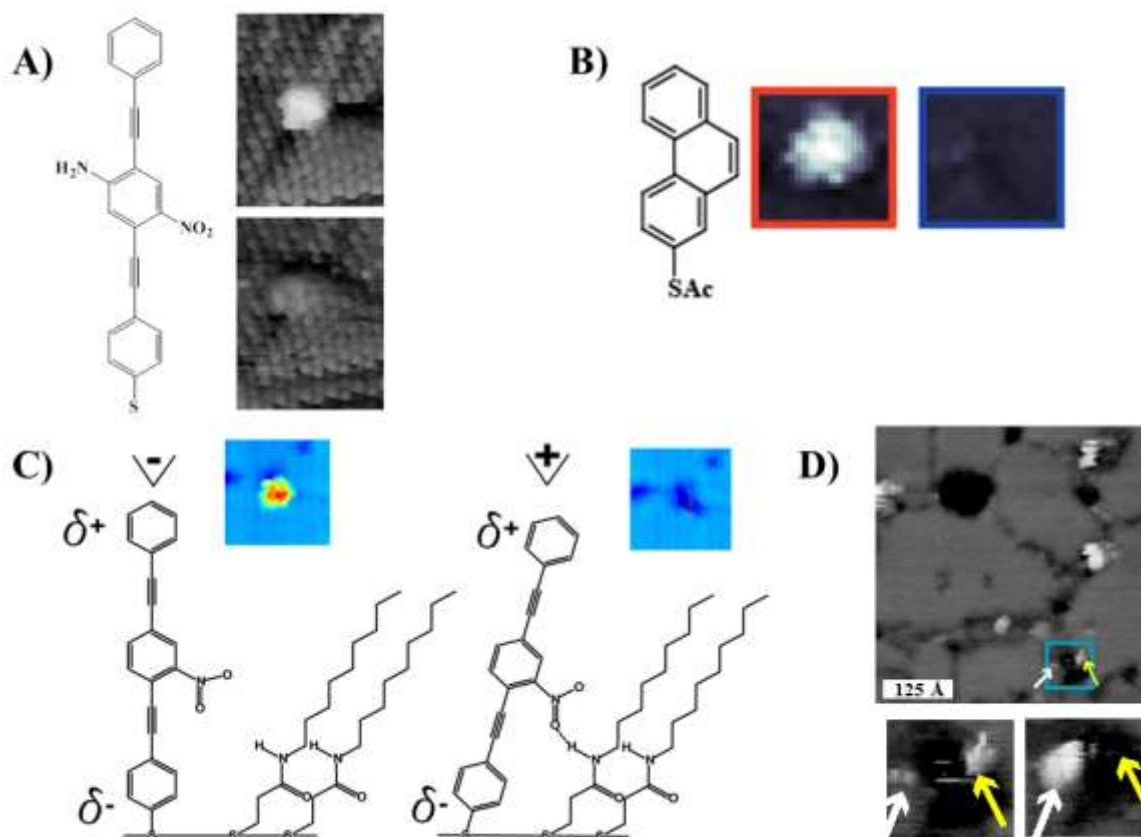


**Figure 1.2.** A) Reversible switching of an isolated single molecule inserted in an alkanethiolate matrix on Au{111} under imaging conditions of -1 V sample bias and 1 pA tunneling current. Figure reproduced with permission from reference 43. Copyright AAAS 2001. B) Phenanthracene molecule exhibits conduction switching even when the rotation of aromatic rings in the backbone is precluded. Figure reproduced with permission from reference 49. Copyright ACS 2006. C) The interaction of the dipole moment of the functionalized oligo(phenylene ethynylene) molecule with the electric field induced by the STM tip bias polarity changes the tilt angle of the molecule and leads to switching due to changes in the S-Au bond hybridization. Figure reproduced with permission from reference 47. Copyright ACS 2005. D) Dithiol-functionalized molecules are capable of moving up and down substrate step edges and also



changing conductance via tilt. Figure reproduced with permission from reference 48. Copyright ACS 2005.

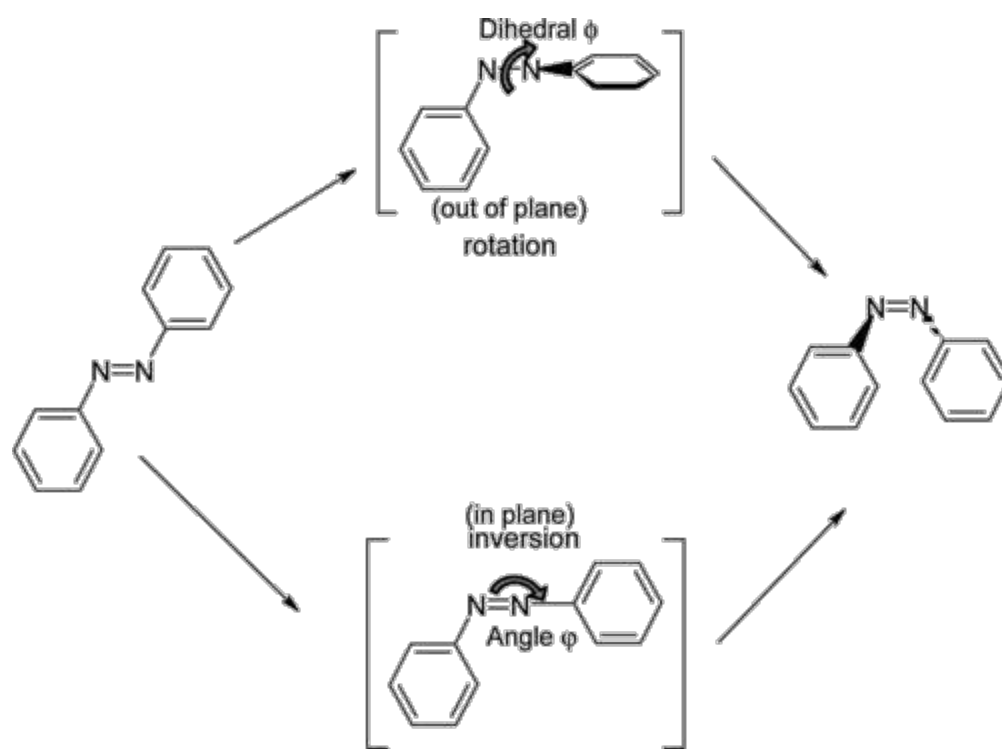


**Figure 1.3.** Simplified schematic depicting the *trans* to *cis* isomerization paths of azobenzene in the gas phase. Figure reproduced with permission from reference 147. Copyright ACS 2005.

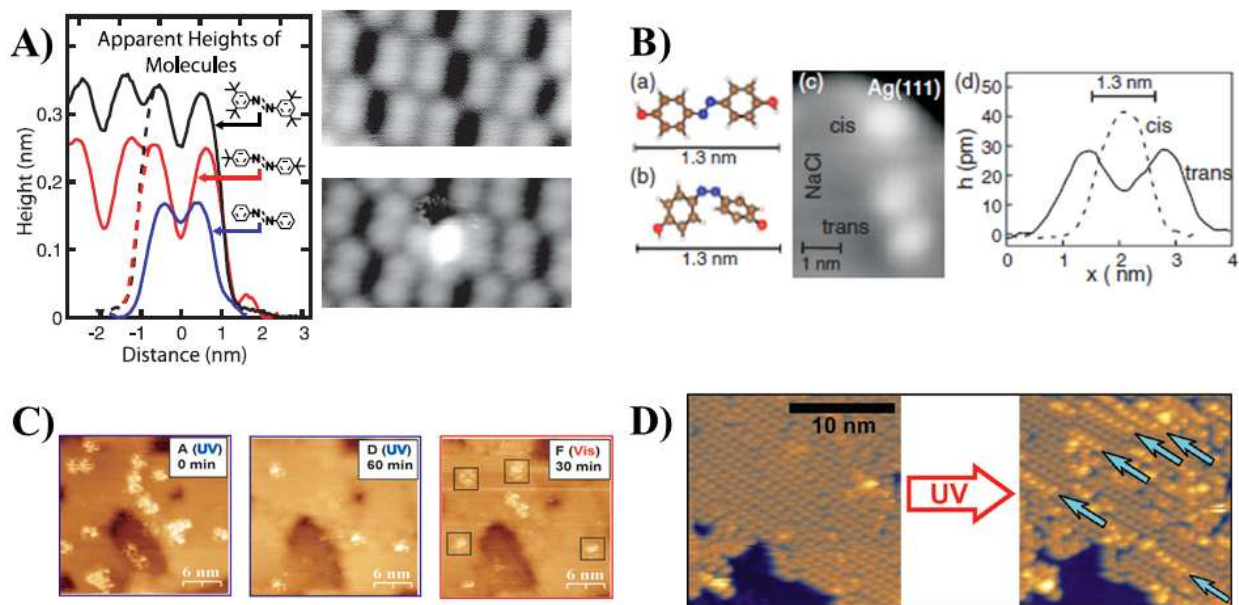


**Figure 1.4.** A) Unfunctionalized and 4,4'-di-*tert*-butyl-functionalized azobenzene did not exhibit isomerization, whereas 3,3',5,5'-tetra-*tert*-butyl-functionalized molecules switched reversibly, between *trans* and *cis* conformations under continuous UV light irradiation. Figure reproduced with permission from reference 160. Copyright APS 2007. B) Azobenzene deposited on a thin insulating NaCl layer on Ag(111) exhibits unidirectional *trans* to *cis* photoisomerization. Figure reproduced with permission from reference 168. Copyright APS 2012. C) Azobenzene molecules functionalized with linear chains exhibit reversible isomerization under ambient conditions. Figure reproduced with permission from reference 53. Copyright ACS 2008. D) 3,3',5,5'-tetra-*tert*-butyl azobenzene located at the edges of islands and at domains switched in bundles when assembled on GaAs(110) surface. Figure reproduced with permission from Reference 169. Copyright ACS 2011.

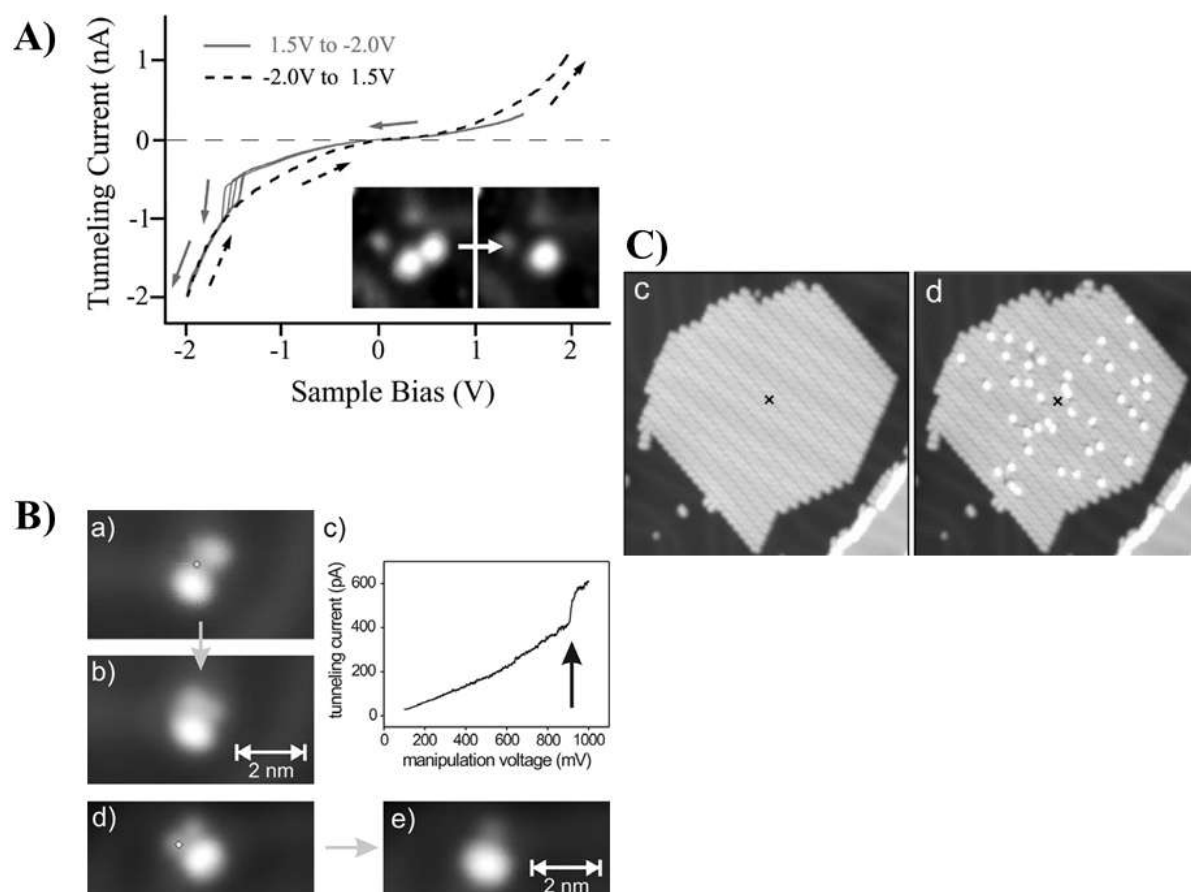


**Figure 1.5.** A) Unfunctionalized azobenzene switched from *trans* to *cis* conformation during current-voltage (I-V) measurements (sudden changes in current at -1.5 V bias can be seen, indicating changes in molecular conformation). Figure reproduced with permission from reference 141. Copyright APS 2006. B) Sequence of images showing unidirectional switching of amine-functionalized azobenzenes using tunneling electrons. Figure reproduced with permission from reference 170. Copyright Elsevier 2007. C) Electric field-induced isomerization of bundles of 3,3',5,5'-tetra-*tert*-butyl-functionalized molecules. Isolated single

molecules could not be isomerized due to diffusion on the surface. Figure reproduced with permission from reference 140. Copyright ACS 2006.

## 1.5 REFERENCES

1. Balzani, V.; Gomez-Lopez, M.; Stoddart, J. F. *Acc. Chem. Res.* **1998**, *31*, 405-414.
2. Balzani, V.; Credi, A.; Raymo, F. M.; Stoddart, J. F. *Angew. Chem. Int. Ed.* **2000**, *39*, 3349-3391.
3. Balzani, V.; Credi, A.; Venturi, M., *Molecular devices and machines: concepts and perspectives for the nanoworld*. Wiley-VCH: Weinheim, 2008.
4. Feringa, B. L.; van Delden, R. A.; Koumura, N.; Geertsema, E. M. *Chem. Rev.* **2000**, *100*, 1789-1816.
5. Katsonis, N.; Lubomska, M.; Pollard, M. M.; Feringa, B. L.; Rudolf, P. *Prog. Surf. Sci.* **2007**, *82*, 407-434.
6. Klajn, R. *Pure Appl. Chem.* **2010**, *82*, 2247-2279.
7. Morgenstern, K. *Prog. Surf. Sci.* **2011**, *86*, 115-161.
8. Feringa, B. L., *Molecular switches*. Wiley-VCH, Weinheim, Germany: 2001.
9. Collin, J. P.; Dietrich-Buchecker, C.; Gavina, P.; Jimenez-Molero, M. C.; Sauvage, J. P. *Acc. Chem. Res.* **2001**, *34*, 477-487.
10. Pace, G.; Ferri, V.; Grave, C.; Elbing, M.; von Hanisch, C.; Zharnikov, M.; Mayor, M.; Rampi, M. A.; Samori, P. *Proc. Natl. Acad. Sci.* **2007**, *104*, 9937-9942.
11. Dri, C.; Peters, M. V.; Schwarz, J.; Hecht, S.; Grill, L. *Nature Nanotech.* **2008**, *3*, 649-653.
12. London, G.; Carroll, G. T.; Landaluce, T. F.; Pollard, M. M.; Rudolf, P.; Feringa, B. L. *Chem. Commun.* **2009**, *13*, 1712.
13. Browne, W. R.; Feringa, B. L. *Annu. Rev. Phys. Chem.* **2009**, *60*, 407-428.
14. Davis, J. J.; Orlowski, G. A.; Rahman, H.; Beer, P. D. *Chem. Commun.* **2010**, *46*, 54-63.
15. Weiss, P. S. *Acc. Chem. Res.* **2008**, *41*, 1772-1781.

16. Cygan, M. T.; Dunbar, T. D.; Arnold, J. J.; Bumm, L. A.; Shedlock, N. F.; Burgin, T. P.; Jones, L.; Allara, D. L.; Tour, J. M.; Weiss, P. S. *J. Am. Chem. Soc.* **1998**, *120*, 2721-2732.
17. Barth, J. V.; Costantini, G.; Kern, K. *Nature* **2005**, *437*, 671-679.
18. Morgenstern, K. *Acc. Chem. Res.* **2009**, *42*, 213-223.
19. Smith, R. K.; Lewis, P. A.; Weiss, P. S. *Prog. Surf. Sci.* **2004**, *75*, 1-68.
20. Li, D.; Paxton, W. F.; Baughman, R. H.; Huang, T. J.; Stoddart, J. F.; Weiss, P. S. *MRS Bull.* **2009**, *34*, 671-681.
21. Saavedra, H. M.; Mullen, T. J.; Zhang, P. P.; Dewey, D. C.; Claridge, S. A.; Weiss, P. S. *Rep. Prog. Phys.* **2010**, *73*, 036501.
22. Claridge, S. A.; Schwartz, J. J.; Weiss, P. S. *ACS Nano* **2011**, *5*, 693-729.
23. Cattaneo, P.; Persico, M. *Phys. Chem. Chem. Phys.* **1999**, *1*, 4739-4743.
24. Seminario, J. M.; Zacarias, A. G.; Tour, J. M. *J. Am. Chem. Soc.* **2000**, *122*, 3015-3020.
25. Kurita, N.; Tanaka, S.; Itoh, S. *J. Phys. Chem. A* **2000**, *104*, 8114-8120.
26. Love, J. C.; Estroff, L. A.; Kriebel, J. K.; Nuzzo, R. G.; Whitesides, G. M. *Chem. Rev.* **2005**, *105*, 1103-1169.
27. Zheng, Y. B.; Pathem, B. K.; Hohman, J. N.; Thomas, J. C.; Kim, M.; Weiss, P. S. *Adv. Mater.* **2012**, *24*, in press. DOI: 10.1002/adma.201201532.
28. Bain, C. D.; Troughton, E. B.; Tao, Y. T.; Evall, J.; Whitesides, G. M.; Nuzzo, R. G. *J. Am. Chem. Soc.* **1989**, *111*, 321-335.
29. Nuzzo, R. G.; Dubois, L. H.; Allara, D. L. *J. Am. Chem. Soc.* **1990**, *112*, 558-569.
30. Buriak, J. M. *Chem. Rev.* **2002**, *102*, 1271-1308.
31. Coti, K. K.; Belowich, M. E.; Liong, M.; Ambrogio, M. W.; Lau, Y. A.; Khatib, H. A.; Zink, J. I.; Khashab, N. M.; Stoddart, J. F. *Nanoscale* **2009**, *1*, 16-39.

32. Kachian, J. S.; Wong, K. T.; Bent, S. F. *Acc. Chem. Res.* **2010**, *43*, 346-355.
33. Silva-Pinto, E.; Neves, B. R. A. *Nanotechnology* **2005**, *16*, 2923-2927.
34. Crego-Calama, M.; Reinhoudt, D. N. *Adv. Mater.* **2001**, *13*, 1171-4.
35. Flink, S.; van Veggel, F.; Reinhoudt, D. N. *J. Phys. Org. Chem.* **2001**, *14*, 407-415.
36. Basabe-Desmonts, L.; Beld, J.; Zimmerman, R. S.; Hernando, J.; Mela, P.; Garcia-Parajo, M. F.; van Hulst, N. F.; van den Berg, A.; Reinhoudt, D. N.; Crego-Calama, M. *J. Am. Chem. Soc.* **2004**, *126*, 7293-7299.
37. Li, X.-M.; Huskens, J.; Reinhoudt, D. N. *J. Mater. Chem.* **2004**, *14*, 2954-2971.
38. Malinsky, M. D.; Kelly, K. L.; Schatz, G. C.; Van Duyne, R. P. *J. Am. Chem. Soc.* **2001**, *123*, 1471-1482.
39. Bocking, T.; Kilian, K. A.; Gaus, K.; Gooding, J. J. *Adv. Funct. Mater.* **2008**, *18*, 3827-3833.
40. Hohman, J. N.; Kim, M.; Schüpbach, B.; Kind, M.; Thomas, J. C.; Terfort, A.; Weiss, P. *S. J. Am. Chem. Soc.* **2011**, *133*, 19422-19431.
41. Bain, C. D.; Whitesides, G. M. *Angew. Chem. Int. Ed.* **1989**, *28*, 506-512.
42. Hohman, J. N.; Claridge, S. A.; Kim, M.; Weiss, P. S. *Mat. Sci. Eng. R* **2010**, *70*, 188-208.
43. Donhauser, Z. J.; Mantooth, B. A.; Kelly, K. F.; Bumm, L. A.; Monnell, J. D.; Stapleton, J. J.; Price, D. W.; Rawlett, A. M.; Allara, D. L.; Tour, J. M.; Weiss, P. S. *Science* **2001**, *292*, 2303-2307.
44. Donhauser, Z. J.; Mantooth, B. A.; Pearl, T. P.; Kelly, K. F.; Nanayakkara, S. U.; Weiss, P. S. *Jpn. J. Appl. Phys., Part 1* **2002**, *41*, 4871-4877.



45. Kushmerick, J. G.; Holt, D. B.; Yang, J. C.; Naciri, J.; Moore, M. H.; Shashidhar, R. *Phys. Rev. Lett.* **2002**, *89*, 086802.
46. Lewis, P. A.; Inman, C. E.; Yao, Y. X.; Tour, J. M.; Hutchison, J. E.; Weiss, P. S. *J. Am. Chem. Soc.* **2004**, *126*, 12214-12215.
47. Lewis, P. A.; Inman, C. E.; Maya, F.; Tour, J. M.; Hutchison, J. E.; Weiss, P. S. *J. Am. Chem. Soc.* **2005**, *127*, 17421-17426.
48. Moore, A. M.; Mantooth, B. A.; Donhauser, Z. J.; Maya, F.; Price, D. W.; Yao, Y. X.; Tour, J. M.; Weiss, P. S. *Nano Lett.* **2005**, *5*, 2292-2297.
49. Moore, A. M.; Dameron, A. A.; Mantooth, B. A.; Smith, R. K.; Fuchs, D. J.; Ciszek, J. W.; Maya, F.; Yao, Y. X.; Tour, J. M.; Weiss, P. S. *J. Am. Chem. Soc.* **2006**, *128*, 1959-1967.
50. Bumm, L. A.; Arnold, J. J.; Cygan, M. T.; Dunbar, T. D.; Burgin, T. P.; Jones, L.; Allara, D. L.; Tour, J. M.; Weiss, P. S. *Science* **1996**, *271*, 1705-1707.
51. Tamada, K.; Akiyama, H.; Wei, T. X. *Langmuir* **2002**, *18*, 5239-5246.
52. Tamada, K.; Akiyama, H.; Wei, T.-X.; Kim, S.-A. *Langmuir* **2003**, *19*, 2306-2312.
53. Kumar, A. S.; Ye, T.; Takami, T.; Yu, B. C.; Flatt, A. K.; Tour, J. M.; Weiss, P. S. *Nano Lett.* **2008**, *8*, 1644-1648.
54. Pace, G.; Petitjean, A.; Lalloz-Vogel, M.-N.; Harrowfield, J.; Lehn, J.-M.; Samorì, P. *Angew. Chem. Int. Ed.* **2008**, *47*, 2484-2488.
55. Kim, M.; Hohman, J. N.; Cao, Y.; Houk, K. N.; Ma, H.; Jen, A. K. Y.; Weiss, P. S. *Science* **2011**, *331*, 1312-1315.
56. Zheng, Y. B.; Payton, J. L.; Chung, C. H.; Liu, R.; Cheunkar, S.; Pathem, B. K.; Yang, Y.; Jensen, L.; Weiss, P. S. *Nano Lett.* **2011**, *11*, 3447-3452.

57. Pathem, B. K.; Kumar, A. S.; Cao, Y.; Zheng, Y. B.; Corley, D. A.; Ye, T.; Aiello, V. J.; Crespi, V.; Houk, K. N.; Tour, J. M.; Weiss, P. S. **2012**, (to be submitted).
58. Zheng, Y. B.; Pathem, B. K.; Payton, J. L.; Bob, B.; Kumar, A. S.; Chung, C. H.; Corley, D. A.; Yang, Y.; Jensen, L.; Tour, J. M.; Weiss, P. S. **2012**, (to be submitted).
59. Donhauser, Z. J.; Price, D. W.; Tour, J. M.; Weiss, P. S. *J. Am. Chem. Soc.* **2003**, *125*, 11462-11463.
60. Mullen, T. J.; Srinivasan, C.; Hohman, J. N.; Gillmor, S. D.; Shuster, M. J.; Horn, M. W.; Andrews, A. M.; Weiss, P. S. *Appl. Phys. Lett.* **2007**, *90*, 063114.
61. Smith, R. K.; Nanayakkara, S. U.; Woehrle, G. H.; Pearl, T. P.; Blake, M. M.; Hutchison, J. E.; Weiss, P. S. *J. Am. Chem. Soc.* **2006**, *128*, 9266-9267.
62. Weck, M.; Jackiw, J. J.; Rossi, R. R.; Weiss, P. S.; Grubbs, R. H. *J. Am. Chem. Soc.* **1999**, *121*, 4088-4089.
63. Mullen, T. J.; Dameron, A. A.; Andrews, A. M.; Weiss, P. S. *Aldrichim. Acta* **2007**, *40*, 21-31.
64. Shuster, M. J.; Vaish, A.; Szapacs, M. E.; Anderson, M. E.; Weiss, P. S.; Andrews, A. M. *Adv. Mater.* **2008**, *20*, 164-167.
65. Vaish, A.; Shuster, M. J.; Cheunkar, S.; Singh, Y. S.; Weiss, P. S.; Andrews, A. M. *ACS Chem. Neurosci.* **2010**, *1*, 495-504.
66. Moore, A. M.; Mantooth, B. A.; Donhauser, Z. J.; Yao, Y. X.; Tour, J. M.; Weiss, P. S. *J. Am. Chem. Soc.* **2007**, *129*, 10352-3.
67. Moore, A. M.; Yeganeh, S.; Yao, Y.; Claridge, S. A.; Tour, J. M.; Ratner, M. A.; Weiss, P. S. *ACS Nano* **2010**, *4*, 7630-7636.

68. Shirakawa, H.; Louis, E. J.; MacDiarmid, A. G.; Chiang, C. K.; Heeger, A. J. *J. Chem. Soc., Chem. Commun.* **1977**, 578-580.
69. Yu, G.; Gao, J.; Hummelen, J. C.; Wudl, F.; Heeger, A. J. *Science* **1995**, 270, 1789-1791.
70. Thompson, B. C.; Fréchet, J. M. J. *Angew. Chem. Int. Ed.* **2008**, 47, 58-77.
71. Xue, Y.; Datta, S.; Ratner, M. A. *J. Chem. Phys.* **2001**, 115, 4292-4299.
72. Xue, Y.; Ratner, M. A. *Phys. Rev. B* **2003**, 68, 115407.
73. Xue, Y.; Ratner, M. A. *Phys. Rev. B* **2004**, 69, 085403.
74. Xue, Y.; Ratner, M. A. *Phys. Rev. B* **2003**, 68, 115406.
75. Monnell, J. D.; Stapleton, J. J.; Jackiw, J. J.; Dunbar, T.; Reinerth, W. A.; Dirk, S. M.; Tour, J. M.; Allara, D. L.; Weiss, P. S. *J. Phys. Chem. B* **2004**, 108, 9834-9841.
76. Monnell, J. D.; Stapleton, J. J.; Dirk, S. M.; Reinerth, W. A.; Tour, J. M.; Allara, D. L.; Weiss, P. S. *J. Phys. Chem. B* **2005**, 109, 20343-20349.
77. Yaliraki, S. N.; Kemp, M.; Ratner, M. A. *J. Am. Chem. Soc.* **1999**, 121, 3428-3434.
78. Di Ventra, M.; Kim, S. G.; Pantelides, S. T.; Lang, N. D. *Phys. Rev. Lett.* **2001**, 86, 288-291.
79. Ke, S.-H.; Baranger, H. U.; Yang, W. *J. Am. Chem. Soc.* **2004**, 126, 15897-15904.
80. Yasuda, S.; Yoshida, S.; Sasaki, J.; Okutsu, Y.; Nakamura, T.; Taninaka, A.; Takeuchi, O.; Shigekawa, H. *J. Am. Chem. Soc.* **2006**, 128, 7746-7747.
81. Adaligil, E.; Shon, Y.-S.; Slowinski, K. *Langmuir* **2009**, 26, 1570-1573.
82. de la Llave, E.; Scherlis, D. A. *Langmuir* **2009**, 26, 173-178.
83. Joachim, C.; Magoga, M. *Chem. Phys.* **2002**, 281, 347-352.
84. Venkataraman, L.; Klare, J. E.; Nuckolls, C.; Hybertsen, M. S.; Steigerwald, M. L. *Nature* **2006**, 442, 904-907.

85. Venkataraman, L.; Klare, J. E.; Tam, I. W.; Nuckolls, C.; Hybertsen, M. S.; Steigerwald, M. L. *Nano Lett.* **2006**, *6*, 458-462.
86. Quek, S. Y.; Venkataraman, L.; Choi, H. J.; Louie, S. G.; Hybertsen, M. S.; Neaton, J. B. *Nano Lett.* **2007**, *7*, 3477-3482.
87. Hybertsen, M. S.; Venkataraman, L.; Klare, J. E.; Cwhalley, A.; Steigerwald, M. L.; Nuckolls, C. *J. Phys.: Condens. Matter* **2008**, *20*.
88. Dell'Angela, M.; Kladnik, G.; Cossaro, A.; Verdini, A.; Kamenetska, M.; Tamblyn, I.; Quek, S. Y.; Neaton, J. B.; Cvetko, D.; Morgante, A.; Venkataraman, L. *Nano Lett.* **2010**, *10*, 2470-2474.
89. Fatemi, V.; Kamenetska, M.; Neaton, J. B.; Venkataraman, L. *Nano Lett.* **2011**, *11*, 1988-1992.
90. Stranick, S. J.; Parikh, A. N.; Allara, D. L.; Weiss, P. S. *J. Phys. Chem.* **1994**, *98*, 11136-11142.
91. Maksymovych, P.; Voznyy, O.; Dougherty, D. B.; Sorescu, D. C.; Yates Jr, J. T. *Prog. Surf. Sci.* **2010**, *85*, 206-240.
92. He, J.; Sankey, O.; Lee, M.; Tao, N.; Li, X.; Lindsay, S. *Faraday Discuss.* **2006**, *131*, 145-154.
93. Quek, S. Y.; Kamenetska, M.; Steigerwald, M. L.; Choi, H. J.; Louie, S. G.; Hybertsen, M. S.; Neaton, J. B.; Venkataraman, L. *Nature Nanotech.* **2009**, *4*, 230-234.
94. Engelkes, V. B.; Beebe, J. M.; Frisbie, C. D. *J. Am. Chem. Soc.* **2004**, *126*, 14287-14296.
95. Sachs, S. B.; Dudek, S. P.; Hsung, R. P.; Sita, L. R.; Smalley, J. F.; Newton, M. D.; Feldberg, S. W.; Chidsey, C. E. D. *J. Am. Chem. Soc.* **1997**, *119*, 10563-10564.

96. Kim; Beebe, J. M.; Jun, Y.; Zhu, X. Y.; Frisbie, C. D. *J. Am. Chem. Soc.* **2006**, *128*, 4970-4971.
97. Ratner, M. A. *J. Phys. Chem.* **1990**, *94*, 4877-4883.
98. Segal, D.; Nitzan, A.; Davis, W. B.; Wasielewski, M. R.; Ratner, M. A. *J. Phys. Chem. B* **2000**, *104*, 3817-3829.
99. Xu, B. Q.; Li, X. L.; Xiao, X. Y.; Sakaguchi, H.; Tao, N. J. *Nano Lett.* **2005**, *5*, 1491-1495.
100. Jones, L.; Schumm, J. S.; Tour, J. M. *J. Org. Chem.* **1997**, *62*, 1388-1410.
101. Prest, P. J.; Prince, R. B.; Moore, J. S. *J. Am. Chem. Soc.* **1999**, *121*, 5933-5939.
102. Fan, F. R. F.; Yang, J. P.; Cai, L. T.; Price, D. W.; Dirk, S. M.; Kosynkin, D. V.; Yao, Y. X.; Rawlett, A. M.; Tour, J. M.; Bard, A. J. *J. Am. Chem. Soc.* **2002**, *124*, 5550-5560.
103. Mantooth, B. A.; Weiss, P. S. *Proc. IEEE* **2003**, *91*, 1785-1802.
104. Robertson, N.; McGowan, C. A. *Chem. Soc. Rev.* **2003**, *32*, 96-103.
105. Stapleton, J. J.; Harder, P.; Daniel, T. A.; Reinard, M. D.; Yao, Y. X.; Price, D. W.; Tour, J. M.; Allara, D. L. *Langmuir* **2003**, *19*, 8245-8255.
106. Blum, A. S.; Yang, J. C.; Shashidhar, R.; Ratna, B. *Appl. Phys. Lett.* **2003**, *82*, 3322-3324.
107. Cai, L. T.; Skulason, H.; Kushmerick, J. G.; Pollack, S. K.; Naciri, J.; Shashidhar, R.; Allara, D. L.; Mallouk, T. E.; Mayer, T. S. *J. Phys. Chem. B* **2004**, *108*, 2827-2832.
108. Richter, L. J.; Yang, C. S. C.; Wilson, P. T.; Hacker, C. A.; van Zee, R. D.; Stapleton, J. J.; Allara, D. L. *J. Phys. Chem. B* **2004**, *108*, 12547-12559.
109. Nielsen, M.; Thomsen, A. H.; Clo, E.; Kirpekar, F.; Gothelf, K. V. *J. Org. Chem.* **2004**, *69*, 2240-2250.

110. Maya, F.; Flatt, A. K.; Stewart, M. P.; Shen, D. E.; Tour, J. M. *Chem. Mater.* **2004**, *16*, 2987-2997.
111. Xiao, X. Y.; Nagahara, L. A.; Rawlett, A. M.; Tao, N. J. *J. Am. Chem. Soc.* **2005**, *127*, 9235-9240.
112. Cai, L. T.; Cabassi, M. A.; Yoon, H.; Cabarcos, O. M.; McGuinness, C. L.; Flatt, A. K.; Allara, D. L.; Tour, J. M.; Mayer, T. S. *Nano Lett.* **2005**, *5*, 2365-2372.
113. Yin, X.; Liu, H.; Zhao, J. *J. Chem. Phys.* **2006**, *125*.
114. Li, X. L.; Xu, B. Q.; Xiao, X. Y.; Yang, X. M.; Zang, L.; Tao, N. J. *Faraday Discuss.* **2006**, *131*, 111-120.
115. Long, M.-Q.; Chen, K.-Q.; Wang, L.; Zou, B. S.; Shuai, Z. *Appl. Phys. Lett.* **2007**, *91*.
116. Yeganeh, S.; Galperin, M.; Ratner, M. A. *J. Am. Chem. Soc.* **2007**, *129*, 13313-13320.
117. Wu, S.; Gonzalez, M. T.; Huber, R.; Grunder, S.; Mayor, M.; Schoenenberger, C.; Calame, M. *Nature Nanotech.* **2008**, *3*, 569-574.
118. Liu, K.; Li, G.; Wang, X.; Wang, F. *J. Phys. Chem. C* **2008**, *112*, 4342-4349.
119. Lu, Q.; Liu, K.; Zhang, H.; Du, Z.; Wang, X.; Wang, F. *ACS Nano* **2009**, *3*, 3861-3868.
120. Ramachandran, G. K.; Hopson, T. J.; Rawlett, A. M.; Nagahara, L. A.; Primak, A.; Lindsay, S. M. *Science* **2003**, *300*, 1413-1416.
121. He, J.; Fu, Q.; Lindsay, S.; Cizek, J. W.; Tour, J. M. *J. Am. Chem. Soc.* **2006**, *128*, 14828-14835.
122. Cornil, J.; Karzazi, Y.; Brédas, J. L. *J. Am. Chem. Soc.* **2002**, *124*, 3516-3517.
123. Seminario, J. M.; Zacarias, A. G.; Tour, J. M. *J. Am. Chem. Soc.* **1998**, *120*, 3970-3974.
124. Sellers, H.; Ulman, A.; Shnidman, Y.; Eilers, J. E. *J. Am. Chem. Soc.* **1993**, *115*, 9389-9401.

125. Busse, C.; Weigelt, S.; Petersen, L.; Laegsgaard, E.; Besenbacher, F.; Linderroth, T. R.; Thomsen, A. H.; Nielsen, M.; Gothelf, K. V. *J. Phys. Chem. B* **2007**, *111*, 5850-5860.
126. Dameron, A. A.; Ciszek, J. W.; Tour, J. M.; Weiss, P. S. *J. Phys. Chem. B* **2004**, *108*, 16761-16767.
127. Tao, Y.-T.; Wu, C.-C.; Eu, J.-Y.; Lin, W.-L.; Wu, K.-C.; Chen, C.-h. *Langmuir* **1997**, *13*, 4018-4023.
128. Reichert, J.; Ochs, R.; Beckmann, D.; Weber, H. B.; Mayor, M.; Löhneysen, H. v. *Phys. Rev. Lett.* **2002**, *88*, 176804.
129. Mayor, M.; Weber, H. B.; Reichert, J.; Elbing, M.; von Hänisch, C.; Beckmann, D.; Fischer, M. *Angew. Chem. Int. Ed.* **2003**, *42*, 5834-5838.
130. Irie, M. *Chem. Rev.* **2000**, *100*, 1683-1684.
131. Caldwell, W. B.; Campbell, D. J.; Chen, K. M.; Herr, B. R.; Mirkin, C. A.; Malik, A.; Durbin, M. K.; Dutta, P.; Huang, K. G. *J. Am. Chem. Soc.* **1995**, *117*, 6071-6082.
132. Zimmerman, G.; Chow, L. Y.; Paik, U. J. *J. Am. Chem. Soc.* **1958**, *80*, 3528-3531.
133. Shinkai, S.; Nakaji, T.; Nishida, Y.; Ogawa, T.; Manabe, O. *J. Am. Chem. Soc.* **1980**, *102*, 5860-5865.
134. Ikeda, T.; Tsutsumi, O. *Science* **1995**, *268*, 1873-1875.
135. Evans, S. D.; Johnson, S. R.; Ringsdorf, H.; Williams, L. M.; Wolf, H. *Langmuir* **1998**, *14*, 6436-6440.
136. Ichimura, K.; Oh, S. K.; Nakagawa, M. *Science* **2000**, *288*, 1624-1626.
137. Hugel, T.; Holland, N. B.; Cattani, A.; Moroder, L.; Seitz, M.; Gaub, H. E. *Science* **2002**, *296*, 1103-1106.
138. Fliegl, H.; Kohn, A.; Hattig, C.; Ahlrichs, R. *J. Am. Chem. Soc.* **2003**, *125*, 9821-9827.

139. Zhang, C.; Du, M. H.; Cheng, H. P.; Zhang, X. G.; Roitberg, A. E.; Krause, J. L. *Phys. Rev. Lett.* **2004**, *92*, 158301.
140. Alemani, M.; Peters, M. V.; Hecht, S.; Rieder, K. H.; Moresco, F.; Grill, L. *J. Am. Chem. Soc.* **2006**, *128*, 14446-14447.
141. Choi, B. Y.; Kahng, S. J.; Kim, S.; Kim, H.; Kim, H. W.; Song, Y. J.; Ihm, J.; Kuk, Y. *Phys. Rev. Lett.* **2006**, *96*, 156106.
142. Henzl, J.; Mehlhorn, M.; Gawronski, H.; Rieder, K. H.; Morgenstern, K. *Angew. Chem. Int. Ed.* **2006**, *45*, 603-606.
143. Wagner, S.; Leyssner, F.; Koerdel, C.; Zarwell, S.; Schmidt, R.; Weinelt, M.; Rueck-Braun, K.; Wolf, M.; Tegeder, P. *Phys. Chem. Chem. Phys.* **2009**, *11*, 6242-6248.
144. Liu, Dunphy, D. R.; Atanassov, P.; Bunge, S. D.; Chen, Z.; López, G. P.; Boyle, T. J.; Brinker, C. J. *Nano Lett.* **2004**, *4*, 551-554.
145. Yuan Q, Zhang Y, Chen T, Lu D, Zhao Z, Zhang X, Li Z, Yan C-H, Tan W. *ACS Nano* **2012**, in press. DOI: 10.1021/nn3018365.
146. Rau, H.; Luddecke, E. *J. Am. Chem. Soc.* **1982**, *104*, 1616-1620.
147. Crecca, C. R.; Roitberg, A. E. *J. Phys. Chem. A* **2006**, *110*, 8188-8203.
148. Lednev, I. K.; Ye, T. Q.; Hester, R. E.; Moore, J. N. *J. Phys. Chem.* **1996**, *100*, 13338-13341.
149. Lednev, I. K.; Ye, T. Q.; Matousek, P.; Towrie, M.; Foggi, P.; Neuwahl, F. V. R.; Umaphathy, S.; Hester, R. E.; Moore, J. N. *Chem. Phys. Lett.* **1998**, *290*, 68-74.
150. Lednev, I. K.; Ye, T. Q.; Abbott, L. C.; Hester, R. E.; Moore, J. N. *J. Phys. Chem. A* **1998**, *102*, 9161-9166.
151. Rau, H. *J. Photochem.* **1984**, *26*, 221-225.



152. Bortolus, P.; Monti, S. *J. Phys. Chem.* **1987**, *91*, 5046-5050.
153. Cembran, A.; Bernardi, F.; Garavelli, M.; Gagliardi, L.; Orlandi, G. *J. Am. Chem. Soc.* **2004**, *126*, 3234-3243.
154. Bohm, N.; Materny, A.; Kiefer, W.; Steins, H.; Muller, M. M.; Schottner, G. *Macromolecules* **1996**, *29*, 2599-2604.
155. Barrett, C. J.; Natansohn, A. L.; Rochon, P. L. *J. Phys. Chem.* **1996**, *100*, 8836-8842.
156. Tsuji, T.; Takeuchi, H.; Egawa, T.; Konaka, S. *J. Am. Chem. Soc.* **2001**, *123*, 6381-6387.
157. Banghart, M.; Borges, K.; Isacoff, E.; Trauner, D.; Kramer, R. H. *Nature Neurosci.* **2004**, *7*, 1381-1386.
158. Briquet, L.; Vercauteren, D. P.; Perpete, E. A.; Jacquemin, D. *Chem. Phys. Lett.* **2006**, *417*, 190-195.
159. Briquet, L.; Vercauteren, D. P.; Andre, J.-M.; Perpete, E. A.; Jacquemin, D. *Chem. Phys. Lett.* **2007**, *435*, 257-262.
160. Comstock, M. J.; Levy, N.; Kirakosian, A.; Cho, J. W.; Lauterwasser, F.; Harvey, J. H.; Strubbe, D. A.; Frechet, J. M. J.; Trauner, D.; Louie, S. G.; Crommie, M. F. *Phys. Rev. Lett.* **2007**, *99*, 038301.
161. Henningsen, N.; Rurali, R.; Franke, K. J.; Fernandez-Torrente, I.; Pascual, J. I. *Appl. Phys. A* **2008**, *93*, 241-246.
162. Cho, J.; Berbil-Bautista, L.; Levy, N.; Poulsen, D.; Frechet, J. M. J.; Crommie, M. F. *J. Chem. Phys.* **2010**, *133*, 234707.
163. Henzl, J.; Morgenstern, K. *Phys. Chem. Chem. Phys.* **2010**, *12*, 6035-6044.
164. Zhou, X. L.; Zhu, X. Y.; White, J. M. *Surf. Sci. Rep.* **1991**, *13*, 73-220.
165. Qiu, X. H.; Nazin, G. V.; Ho, W. *Science* **2003**, *299*, 542-546.

166. Alemani, M.; Selvanathan, S.; Ample, F.; Peters, M. V.; Rieder, K.-H.; Moresco, F.; Joachim, C.; Hecht, S.; Grill, L. *J. Phys. Chem. C* **2008**, *112*, 10509-10514.
167. Hagen, S.; Kale, P.; Leyssner, F.; Nandi, D.; Wolf, M.; Tegeder, P. *J. Chem. Phys.* **2008**, *129*, 164102.
168. Henzl, J.; Puschnig, P.; Ambrosch-Draxl, C.; Schaate, A.; Ufer, B.; Behrens, P.; Morgenstern, K. *Phys. Rev. B* **2012**, *85*, 035410.
169. Pechenezhskiy, I. V.; Cho, J.; Nguyen, G. D.; Berbil-Bautista, L.; Giles, B. L.; Poulsen, D. A.; Fréchet, J. M. J.; Crommie, M. F. *J. Phys. Chem. C* **2011**, *116*, 1052-1055.
170. Henzl, J.; Bredow, T.; Morgenstern, K. *Chem. Phys. Lett.* **2007**, *435*, 278-282.

**CHAPTER 2**  
***INSTRUMENTATION***

## 2.1 SCANNING TUNNELING MICROSCOPY

Since its invention by Binnig and Rohrer in 1981,<sup>1-4</sup> STM has developed into one of the most widely employed surface characterization techniques.<sup>5-14</sup> The basic principle behind the operation of STM is quantum mechanical tunneling.<sup>2,3,15</sup> An atomically sharp metal probe tip is brought in to close proximity (typically, a few Ångströms) above a surface and a voltage is applied between the two. In classical mechanics, when the energy of the electron is smaller than the potential difference between the probe tip and the metal surface, the electron transfer over this barrier is forbidden. However, due to the overlap of the electron wave functions of the two metals that decays into the gap between them, there exists a finite probability for electron tunneling, resulting in current flow between the metals. The bias is applied between the tip and the sample and the net tunneling direction depends on this bias polarity (Fig. 2.1). For a positive sample bias, the electrons tunnel from occupied states of the tip to the unoccupied states of the sample and for a negative sample bias, the electrons tunnel from the occupied states of the surface to the unoccupied states of the tip. Moreover, this tunneling current is exponentially dependent upon the distance between the metals and it varies inversely by an order of magnitude with an Ångström change in tip-surface distance. Mathematically, the wave function of the tunneling electrons can be depicted as follows:

$$\psi(z) = \psi(0)e^{-kz},$$

where

$$k = \frac{\sqrt{2m(V-E)}}{\hbar},$$

$z$  is the tip-sample distance,  $m$  is the mass of the electron,  $V$  is the potential barrier,  $E$  is the energy of tunneling electron, and  $\hbar$  is Planck's constant.<sup>16,17</sup>

The STM is typically operated in one of two modes: constant-current mode and constant-height mode. In constant-current mode, the tunneling current between the tip and the sample is held constant by employing a feedback loop that controls a scanning piezoelectric tube to extend or to retract the probe tip. In this way, when the tip rasters over the sample in  $x$  and  $y$  directions, a topographic map of the surface is obtained. Note that, the STM image is a convolution of both topography and conductivity of the surface. The probe tip retracts or extends in order to compensate for the spatial variations of local density of states. The piezoelectric transducer itself is made out of a ceramic that deforms when a voltage is applied to it. Typically, piezoelectric materials can sustain a voltage of  $\sim 100$  V and can deform by  $\sim 0.1$  Å/V. Thus, the maximum scan area of a typical STM head is about  $1 \mu^2$ . Due to this highly precise piezoelectric control, STM can reveal a wealth of information both at single molecule and atomic scales, which would be otherwise difficult to obtain. Although many STM measurements are performed in UHV and at low temperatures in order to retain the purity of the sample and to minimize external noise, all the STM measurements discussed henceforth in this thesis were performed at room temperature and under ambient conditions.

## **2.2 SURFACE-ENHANCED RAMAN SPECTROSCOPY**

Raman spectroscopy works on the principle of light scattering when a molecule is irradiated with incoming beam of light.<sup>18</sup> When incident light interacts with a molecule in its ground vibrational state, the molecule can be raised to a real resonant state or a virtual nonresonant state of higher energy. In Rayleigh and Raman scattering, the excited electron

relaxes back to the ground state immediately resulting in the process of emission of a photon. In this latter process, if the electron relaxes back to its original state, then the wavelength of the scattered light will be the same as the incident light. This process is referred to as Rayleigh scattering (Fig 2.2a). If the electron relaxes to a state different from the original state, the energy of the emitted photon will be different from the initial energy and this is Raman scattering. When the electron relaxes to an energy state higher than the initial state, the emitted energy will be smaller than the incident energy, this scattering is called Stokes scattering (Fig 2.2b). If the emitted energy is higher than the incident energy, the process is referred to as anti-Stokes scattering (Fig. 2.2c). The resulting spectrum of emitted photons is the Raman spectrum. When a molecule is placed in an electric field, due to the displacements in the electrons and the nuclei, an induced dipole moment is produced within the molecule. This induced dipole moment can be expressed as

$$\mu = \alpha E,^{19-21}$$

where

$\alpha$  is the polarizability of the molecule and  $E$  is the electric field.

The electric field of an incident beam of light can be expressed as

$$E = E' \cos(2\pi\vartheta t),$$

where  $E'$  is constant,  $\vartheta$  is the frequency of radiation, and  $t$  is time.

The dipole moment is thus

$$\mu = \alpha E' \cos(2\pi\vartheta t).^{19-21}$$

This result indicates that the molecular dipole oscillates with the same frequency as the incident light.

However, the polarizability of the molecule changes with the vibrational states of the molecule, and can be expressed as follows:

$$\alpha = \alpha' + (r - r') \frac{\partial \alpha}{\partial r},^{19-21}$$

where  $\alpha'$  is the equilibrium polarizability of the molecule,  $r$  and  $r'$  are the bond lengths at any given instant and at equilibrium, respectively.

If the molecule oscillates in a simple harmonic motion, then  $r - r'$  can be expressed as  $R \cos(2\pi \vartheta' t)$

where  $R$  is the maximum separation between the two atoms relative to their equilibrium positions.

Thus,  $\alpha$  can be expressed as  $\alpha' + R \cos(2\pi \vartheta' t) \frac{\partial \alpha}{\partial r}$ . Substituting  $\alpha$  in  $\mu$  gives

$$\begin{aligned} \mu &= (\alpha' + R \cos(2\pi \vartheta' t) \frac{\partial \alpha}{\partial r}) (E' \cos(2\pi \vartheta t)) \\ &= \alpha' E' \cos(2\pi \vartheta t) + \frac{\partial \alpha}{\partial r} \frac{R E'}{2} [\cos(2\pi(\vartheta - \vartheta'))t + \cos(2\pi(\vartheta + \vartheta'))t], \end{aligned}$$

where the first term is the contribution from Rayleigh scattering and the second and the third terms correspond to Stokes and anti-Stokes scattering.<sup>19-21</sup> Thus, if the molecular polarizability does not change ( $\frac{\partial \alpha}{\partial r} = 0$ ), the vibrational mode is not Raman active; this is the selection rule of

Raman spectroscopy. The resulting intensities in the Raman spectrum are proportional to the square of the magnitude of electric field incident on the molecule.

Surface-enhanced Raman spectroscopy is highly sensitive and is capable of single molecule detection and characterization.<sup>22-27</sup> The first SERS results were discovered in 1974, when Fleischmann and coworkers designed experiments to increase the surface area of a silver electrode by roughening the surface and subsequently exposing the metal to a solution of pyridine.<sup>28</sup> They discovered that the rough silver surface produces six orders of magnitude intense Raman spectrum. Although the mechanism behind SERS is still a matter of great debate, two processes have been proposed to play major roles: electromagnetic enhancement<sup>22,25,29-34</sup> and chemical enhancement.<sup>35-39</sup> While electromagnetic enhancements has been credited with greater part of SERS, about two orders of magnitude enhancements have been correlated to chemical enhancement.<sup>25</sup>

Electromagnetic enhancement is correlated to the surface roughness of the material. The size, shape, and thus the surface roughness of the material can be precisely controlled and tuned by various chemical and lithographic techniques. Most commonly, nanoholes,<sup>40-44</sup> nanodisks,<sup>42,45-48</sup> and nanoparticles<sup>49-52</sup> are employed in SERS measurements. As mentioned above, the intensity of the Raman signal is proportional to the electromagnetic field incident upon the molecule. If a molecule is adsorbed to a nanoparticle, the electromagnetic field experienced by the molecule can be given by the equation:

$$E = E^0 + E^{np},^{53}$$

where  $E^0$  is the electromagnetic field on the molecule in the absence of nanoparticle and  $E^{np}$  is the field emitted due to the surface roughness of the nanoparticle.



Since the source of the incident radiation is usually far away, the field experienced by the molecule is low and hence the Raman intensity in the absence of the nanoparticle will be very small. However, when the incident radiation illuminates the nanoparticles (that possess a complex dielectric constant), due to the coherent oscillation of the free electrons generating surface plasmons, the electromagnetic field in their vicinity is greatly modified. Moreover, due to the direct adsorption of the molecule to the rough surface of the nanoparticle and due to the extreme proximity, the contribution of  $E^{np}$  is quite large when compared to  $E^0$ . The enhancement factor is given by the ratio of the field at the position of the molecule and the incident field,  $E/E^0$ . This result implies that the scattered radiation is enhanced by a factor of  $(E/E^0)^2$ . However, the local field enhancement factor does not take into consideration the enhancement in the electric field polarization. It has to be considered that the Stokes and anti-Stokes fields are enhanced if the light is in resonance with the surface plasmons of the nanoparticles, resulting in an enhancement factor of  $(E'/E^0)^2$ . Thus, the total enhancement due to SERS can be expressed as  $(E/E^0)^2 (E'/E^0)^2$ . However, in most scenarios, the Raman shift is small or when compared to the Stokes shift, the plasmon width is quite large, resulting in a more generalized approximation of the SERS enhancement to be  $(E/E^0)^4$ .<sup>20,21</sup>

Chemical enhancement, on the other hand, is considered to arise from the modification of the molecular polarizability due to the metal-molecule charge transfer interactions.<sup>20,54</sup> When an incident photon creates an electron-hole pair in the metal nanoparticle, the electron gets excited as a hot electron and tunnels into the LUMO of the adsorbate molecule, thus creating a negative ion. The equilibrium geometry of this anion will be different from that of the neutral molecule and this additional electron then transfers back to the metal, while relaxing the adsorbate molecule during this process. The electron recombines with the hole in the metal resulting in the

formation of a vibrationally excited neutral molecule and the release of a photon. As can be understood, this enhancement depends on the covalent binding of the molecule and the metal and thus is dependent upon the binding site, energy level difference of the adsorbate, and binding geometry.

Although it is difficult to differentiate between the two mechanisms experimentally, studies have shown the presence of chemical enhancement while the electromagnetic enhancement is widely accepted to be the dominant contributor to the SERS effect.<sup>20,51</sup> As will be demonstrated in subsequent chapters, SERS can be employed as a characterization tool to follow the molecular behavior at the single-molecule scale and to understand the intermolecular interactions that dictate the cooperative functions of nanoscale assemblies.<sup>55</sup> Substrate preparations and the characterization techniques will be detailed in following chapters.

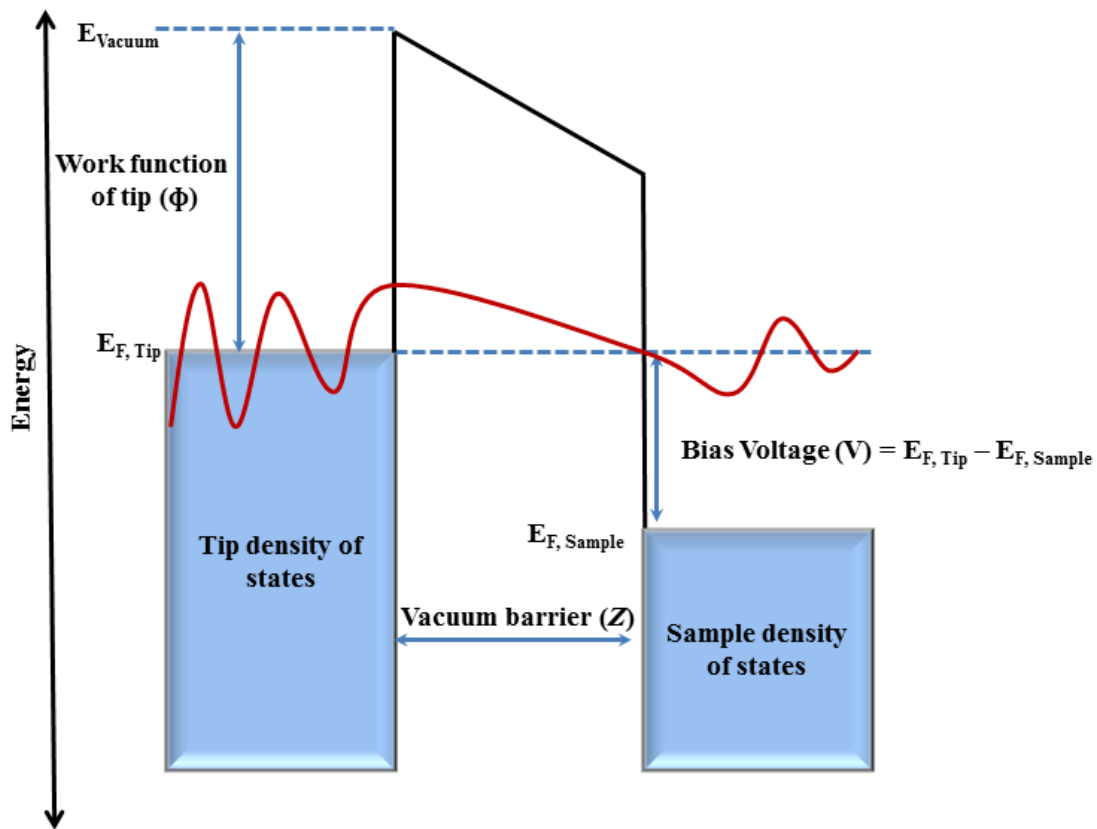


**Figure 2.1.** Energy level diagram depicting a one-dimensional electron tunneling junction in scanning tunneling microscopy. A positive sample bias is shown in the schematic, which results in the electron tunneling from the probe to the sample.

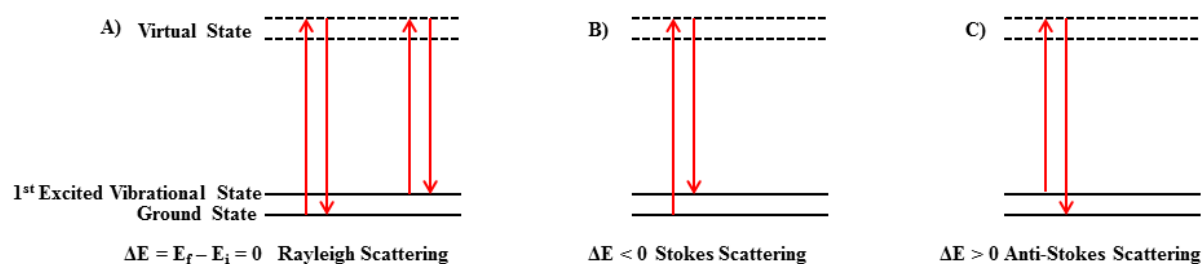


**Figure 2.2.** Schematics depicting: A) Rayleigh scattering in which the excited electron relaxes to the same energy level resulting in no net change in the energy of the emitted photon, B) Stokes scattering, in which the excited electron relaxes to an energy level higher than the initial state resulting in a net loss of energy of the emitted photon, and C) anti-Stokes scattering, in which the excited electron relaxes to an energy level lower than the initial state, resulting in a net increase in the energy of the scattered photon.

## 2.3 REFERENCES

1. Binnig, G.; Rohrer, H. *Helv. Phys. Acta* **1982**, *55*, 726-735.
2. Binnig, G.; Rohrer, H.; Gerber, C.; Weibel, E. *Appl. Phys. Lett.* **1982**, *40*, 178-180.
3. Binnig, G.; Rohrer, H. *Surf. Sci.* **1983**, *126*, 236-244.
4. Binnig, G.; Rohrer, H. *Rev. Mod. Phys.* **1987**, *59*, 615-625.
5. Barth, J. V.; Brune, H.; Ertl, G.; Behm, R. J. *Phys. Rev. B* **1990**, *42*, 9307-9318.
6. Eigler, D. M.; Schweizer, E. K. *Nature* **1990**, *344*, 524-526.
7. Crommie, M. F.; Lutz, C. P.; Eigler, D. M. *Science* **1993**, *262*, 218-220.
8. Andres, R. P.; Bein, T.; Dorogi, M.; Feng, S.; Henderson, J. I.; Kubiak, C. P.; Mahoney, W.; Osifchin, R. G.; Reifenberger, R. *Science* **1996**, *272*, 1323-1325.
9. Bumm, L. A.; Arnold, J. J.; Cygan, M. T.; Dunbar, T. D.; Burgin, T. P.; Jones, L.; Allara, D. L.; Tour, J. M.; Weiss, P. S. *Science* **1996**, *271*, 1705-1707.
10. Poirier, G. E. *Chem. Rev.* **1997**, *97*, 1117-1127.
11. Stipe, B. C.; Rezaei, M. A.; Ho, W. *Science* **1998**, *280*, 1732-1735.
12. Wildoer, J. W. G.; Venema, L. C.; Rinzler, A. G.; Smalley, R. E.; Dekker, C. *Nature* **1998**, *391*, 59-62.
13. Donhauser, Z. J.; Mantooth, B. A.; Kelly, K. F.; Bumm, L. A.; Monnell, J. D.; Stapleton, J. J.; Price, D. W.; Rawlett, A. M.; Allara, D. L.; Tour, J. M.; Weiss, P. S. *Science* **2001**, *292*, 2303-2307.
14. Barth, J. V.; Costantini, G.; Kern, K. *Nature* **2005**, *437*, 671-679.
15. Hansma, P. K.; Tersoff, J. *J. Appl. Phys.* **1987**, *61*, R1-R23.
16. Chen, C. J. in *Introduction to Scanning Tunneling Microscopy*, Oxford University press, Oxford (1993).

17. Bonnell, D. A. in *Scanning Probe Microscopy and Spectroscopy: Theory, Techniques, and Applications*, Wiley-VCH, Inc., New York (2001).
18. Raman, C. V.; Krishnan, K. S. *Nature* **1928**, *121*, 501-502.
19. Smith, E.; Dent, G. in *Modern Raman Spectroscopy – A Practical Approach*, John Wiley & Sons, Ltd, Hoboken (2005).
20. Willets, K. A.; Van Duyne, R. P. *Annu. Rev. Phys. Chem.* **2007**, *58*, 267-297.
21. Stiles, P. L.; Dieringer, J. A.; Shah, N. C.; Van Duyne, R. P. *Annu. Rev. Anal. Chem.* **2008**, *1*, 601-626.
22. Moskovits, M. *Rev. Mod. Phys.* **1985**, *57*, 783-826.
23. Nie, S. M.; Emery, S. R. *Science* **1997**, *275*, 1102-1106.
24. Kneipp, K.; Wang, Y.; Kneipp, H.; Perelman, L. T.; Itzkan, I.; Dasari, R.; Feld, M. S. *Phys. Rev. Lett.* **1997**, *78*, 1667-1670.
25. Campion, A.; Kambhampati, P. *Chem. Soc. Rev.* **1998**, *27*, 241-250.
26. Xu, H. X.; Bjerneld, E. J.; Kall, M.; Borjesson, L. *Phys. Rev. Lett.* **1999**, *83*, 4357-4360.
27. Kneipp, K.; Kneipp, H.; Itzkan, I.; Dasari, R. R.; Feld, M. S. *Chem. Rev.* **1999**, *99*, 2957-2976.
28. Fleischman, M.; Hendra, P. J.; McQuillan, A. J. *Chem. Phys. Lett.* **1974**, *26*, 163-166.
29. Jeanmaire, D. L.; Vanduyne, R. P. *J. Electroanal. Chem.* **1977**, *84*, 1-20.
30. Gersten, J.; Nitzan, A. *J. Chem. Phys.* **1980**, *73*, 3023-3037.
31. Otto, A. *J. Raman Spectrosc.* **1991**, *22*, 743-752.
32. Otto, A.; Mrozek, I.; Grabhorn, H.; Akemann, W. *J. Phys.: Condens. Matter* **1992**, *4*, 1143-1212.
33. Xu, H. X.; Aizpurua, J.; Kall, M.; Apell, P. *Phys. Rev. E* **2000**, *62*, 4318-4324.

34. Hao, E.; Schatz, G. C. *J. Chem. Phys.* **2004**, *120*, 357-366.
35. Albrecht, M. G.; Creighton, J. A. *J. Am. Chem. Soc.* **1977**, *99*, 5215-5217.
36. Lin Lin, Z.; Jensen, L.; Schatz, G. C. *Nano Lett.* **2006**, *6*, 1229-34.
37. Morton, S. M.; Jensen, L. *J. Am. Chem. Soc.* **2009**, *131*, 4090-4098.
38. Morton, S. M.; Ewusi-Annan, E.; Jensen, L. *Phys. Chem. Chem. Phys.* **2009**, *11*, 7424-7429.
39. Valley, N.; Jensen, L.; Autschbach, J.; Schatz, G. C. *J. Chem. Phys.* **2010**, *133*.
40. Brolo, A. G.; Arctander, E.; Gordon, R.; Leathem, B.; Kavanagh, K. L. *Nano Lett.* **2004**, *4*, 2015-2018.
41. Yu, Q.; Golden, G. *Langmuir* **2007**, *23*, 8659-8662.
42. Yu, Q.; Guan, P.; Qin, D.; Golden, G.; Wallace, P. M. *Nano Lett.* **2008**, *8*, 1923-1928.
43. Anema, J. R.; Brolo, A. G.; Marthandam, P.; Gordon, R. *J. Phys. Chem. C* **2008**, *112*, 17051-17055.
44. Lee, S. H.; Bantz, K. C.; Lindquist, N. C.; Oh, S.-H.; Haynes, C. L. *Langmuir* **2009**, *25*, 13685-13693.
45. Abu Hatab, N. A.; Oran, J. M.; Sepaniak, M. J. *ACS Nano* **2008**, *2*, 377-385.
46. Banholzer, M. J.; Osberg, K. D.; Li, S.; Mangelson, B. F.; Schatz, G. C.; Mirkin, C. A. *ACS Nano* **2010**, *4*, 5446-5452.
47. Tripathy, S.; Marty, R.; Lin, V. K.; Teo, S. L.; Ye, E.; Arbouet, A.; Saviot, L.; Girard, C.; Han, M. Y.; Mlayah, A. *Nano Lett.* **2011**, *11*, 431-437.
48. Juluri, B. K.; Chaturvedi, N.; Hao, Q.; Lu, M.; Velegol, D.; Jensen, L.; Huang, T. J. *ACS Nano* **2011**, *5*, 5838-5847.
49. Cao, Y. W. C.; Jin, R. C.; Mirkin, C. A. *Science* **2002**, *297*, 1536-1540.

50. Talley, C. E.; Jackson, J. B.; Oubre, C.; Grady, N. K.; Hollars, C. W.; Lane, S. M.; Huser, T. R.; Nordlander, P.; Halas, N. J. *Nano Lett.* **2005**, *5*, 1569-1574.
51. Anker, J. N.; Hall, W. P.; Lyandres, O.; Shah, N. C.; Zhao, J.; Van Duyne, R. P. *Nature Mater.* **2008**, *7*, 442-453.
52. Qian, X.; Peng, X.-H.; Ansari, D. O.; Yin-Goen, Q.; Chen, G. Z.; Shin, D. M.; Yang, L.; Young, A. N.; Wang, M. D.; Nie, S. *Nat. Biotechnol.* **2008**, *26*, 83-90.
53. Kneipp, K.; Kneipp, H.; Itzkan, I.; Dasari, R. R.; Feld, M. S. *J. Phys.: Condens. Matter* **2002**, *14*, R597-R624.
54. Doering, W. E.; Nie, S. M. *J. Phys. Chem. B* **2002**, *106*, 311-317.
55. Zheng, Y. B.; Payton, J. L.; Chung, C.-H.; Liu, R.; Cheunkar, S.; Pathem, B. K.; Yang, Y.; Jensen, L.; Weiss, P. S. *Nano Lett.* **2011**, *11*, 3447-3452.



### **CHAPTER 3**

#### ***COORDINATED DRIVEN MOTION OF ASSEMBLED ONE-DIMENSIONAL CHAINS OF TETHERED FUNCTIONAL MOLECULES***

### 3.1 INTRODUCTION

Research in molecular-scale devices has accelerated, largely due to experimental evidence showing reversible control over the conductance switching of organic molecules at the single-molecule scale.<sup>1-6</sup> However, the successful integration of molecular devices to act cooperatively remains limited by a number of key challenges that include fabricating precise molecular systems, connecting them together, and coordinating their action by finding strong coupling mechanisms. Understanding the limits of cooperativity and interferences in functional supramolecular systems at the smallest scales is critical to realizing the goal of building functional devices from the bottom up.<sup>7-10</sup>

Although atomic and molecular manipulation to create 1D systems using STM has been demonstrated,<sup>11-14</sup> such serial techniques are impractical for the production of devices. Molecular self- and directed assembly, however, may be exploited to fabricate 1D, 2D, and 3D structures on solid substrates, spontaneously, under ambient conditions.<sup>15-19</sup> Self-assembly can be used to fabricate molecular switches into nanoscale wires that can then be controlled by external stimuli such as light,<sup>4,5,20-22</sup> electric field,<sup>23-25</sup> or tunneling electrons.<sup>26,27</sup> Theoretical calculations of charge propagation in 1D molecular wires have been performed,<sup>28-30</sup> but few experimental measurements have been made due to the practical challenge of connecting molecular wires and devices to microscale electrodes for measurement.<sup>13,31-34</sup>

Light and tunneling electrons offer straightforward means of manipulating molecular systems; thus, we have developed a technique for the self-assembly of 1D molecular chains of azobenzene-functionalized molecules, 4-[2-(4-phenylazo-phenyl)-ethoxy]-butane-1-thiol (**Azo**, shown in Fig. 3.1A), grown at the domain boundaries of host **C10** SAM matrices, and

observed the effects of concerted switching. We attribute this effect to be triggered by charge delocalization along the linear chains. We chose **Azo** molecules, since they represent a synthetic analogue of a biomolecular switch (such as naturally occurring retinal), which can undergo reversible isomerization between its thermodynamically stable planar *trans* conformation and a non-planar *cis* conformation upon exposure to UV and visible radiation, respectively.

Azobenzenes can isomerize either by rotation about their N=N bond or via in-plane inversion of the C-N=N bond. The C-N=N bond angle changes from 60° to -60°, facilitating the in-plane transition of the phenyl ring.<sup>35</sup> The inversion mechanism is generally accepted as the isomerization pathway. Due to the difference in planarity of the isomers, *trans-Azo* is approximately 100 times more conductive than the *cis* isomer.<sup>36</sup> Since STM images are convolutions of both topography and conductance of the molecules,<sup>37,38</sup> STM is an ideal tool to follow the reversible isomerization of these molecules assembled on a conductive substrate. Reversible isomerization of azobenzene between its more conductive *trans* (ON) state and less conductive *cis* (OFF) state at ensemble and single-molecule scales in vapor, liquid, and on solid substrates using external stimuli is well established.<sup>4,5,24,25,39-41</sup> Here, we discuss the assembly of these molecular switches into 1D chains at the domain boundaries of pre-existing **C10** SAM matrices. We have established control over the reversible isomerization of the 1D molecular chains using tunneling electrons from the STM probe tip, and thus, over the conductivity of the supramolecular wires.

### 3.2 METHODS

The **Azo** chains were prepared by immersing a flame-annealed Au{111} substrate in a 1 mM ethanolic solution of **C10** for 1 min. This results in the formation of highly disordered domains of **C10**. The sample was then rinsed with ethanol, blown dry with nitrogen, and

immersed in a 0.2 mM ethanolic solution of **Azo** molecule for 4 min. Isolated single or clusters of **Azo** molecules preferentially bind to defect sites, such as **C10** domain boundaries and substrate vacancy islands. The sample was then vapor annealed at 80 °C over **C10** for 2 h. This process resulted in the formation of 1D chains of **Azo** molecules in the **C10** domain boundaries.<sup>42</sup> All the measurements in this study were performed using a custom-built STM at ambient conditions while the sample was exposed to air.<sup>5</sup>

### 3.3 RESULTS AND DISCUSSIONS

In STM images, the **Azo** chains protrude from the surrounding **C10** matrix with an apparent height of  $\sim 2$  Å, consistent with our previous work.<sup>5</sup> Chains form herringbone structures composed of either single or double rows of **Azo** molecules (Figs. 3.1B, C). The two forms were equally abundant on the surface. Similar herringbone structures were previously reported in single-component azobenzene-based monolayers.<sup>43</sup> In single-row (**1R**) chains, neighboring azobenzene molecules were separated by center-to-center distances of  $4.5 \pm 0.3$  Å (Fig. 3.1B). In double-row (**2R**) chains, farthest molecular pairs forming a repetitive unit (Fig. 3.1C inset) were separated by center-to-center distances of  $8.8 \pm 0.4$  Å and the nearest neighboring molecules were separated by center-to-center distances of  $5.0 \pm 0.3$  Å (Fig. 3.1C). Lengths of **1R** and **2R** chains varied between 30 and 200 Å depending upon the initial sizes of the host **C10** domains.

Using sufficiently energetic electrons from the STM probe tip, we selectively induced isomerization of **Azo** molecules at one point on the 1D chains and subsequently measured the effects along the entire chain. Unlike photoexcitation, this stimulus gave us the ability to determine the precise location of excitation. During the isomerization from *trans* to *cis*, azobenzene requires energy from an external source in order to reach the excited electronic state

or a negative ion resonance state.<sup>2,44</sup> Here, we employed tunneling electrons from the STM probe tip to isomerize the azobenzene moieties. While the STM was operating in constant-current mode with a tunneling current of 1 pA, we positioned the STM probe tip at a point above a **1R** chain (yellow arrow in Fig. 3.2A) and applied a sample bias of 2.0 V for 2 min with the feedback loop still active (at a subthreshold sample bias of 1.0 V, no isomerization is observed). All subsequent images were recorded at  $V_s = 1.0$  V and  $I_t = 1$  pA. The STM topographs recorded before and after excitation are shown in Figure 3.2. All the molecules in the **1R** chain (~90 Å long) switched OFF (i.e., isomerized from *trans* to *cis*, Fig. 3.2B). High-resolution STM images showing reductions in apparent height (relative to the surrounding matrix) after isomerization to the *cis* conformation can be seen in Figures 3.2D and 2E. The apparent heights of the protrusions with respect to the surrounding matrix before and after isomerization were ~2.2 Å and ~0.5 Å, respectively (Figs. 3.2F, G). We attribute this difference in topography and change in the conductivity to isomerization of the **Azo** molecules, consistent with our previous measurements of single-molecule photoisomerization.<sup>5</sup> However, the concerted switching of the entire **Azo** chain based on stimulation at a single point is unprecedented. The key features of the process are: a) the entire chains switch OFF in *both* directions from the point of excitation and b) the isomerization stops at the point where there is a break in the continuity of the chain. We consider various mechanisms that could be responsible for this result.<sup>44</sup>

We propose that low energy electrons (tunneling from the STM probe tip) lead to the formation of a temporary negative ion resonance state that couples along the chain. The electron affinity of azobenzene has been measured by several techniques to be 1.38-1.58 eV.<sup>41,45</sup> Our computations indicate that the electron affinity of **Azo** is 0.05 eV less positive than that of azobenzene. Since the work function of bare gold is considerably higher than this (5.1 eV),<sup>46</sup> it

is necessary to apply a considerable voltage in order to populate the radical anion state of **Azo** on the gold surface. In our experiments, the switching of *trans* to *cis* occurs only at voltages above 1.8 eV and all the electron-induced switching experiments shown here were carried out at 2 eV. Figure 3.3 shows the computed energies of the *trans* and *cis* **Azo** in the ground and negative ion states, with the positions of neutral and anion placed according to their positions as indicated from the STM measurements. As described in a variety of computational studies, addition of an electron to the  $\pi^*$  LUMO of azobenzene lowers the N=N bond strength and reduces the energy required for *cis-trans* isomerization.<sup>41,47</sup> The *cis* geometry of the anionic state is still higher in energy than the *trans* by 0.69 eV, and hence cannot be populated readily. However, the anionic state of *trans-Azo* populated by electron tunneling at 2 eV is higher in energy than the transition state for *cis-trans* isomerization in the neutral, and the loss of the electron from the *trans-Azo* anionic state can be accompanied by simultaneous isomerization to the *cis-Azo* neutral. The N=N bond length in the transition state of the neutral conformation is 1.23 Å, whereas it is 1.34 Å in the anionic transition state. This 0.11 Å change in the bond distance weakens the N=N bond and enables the rotation of the molecule into its *cis* conformation. The relevant conformation coordinate for the inversion transition state of neutral **Azo** is the bond angle  $\angle$  (N=N-C) that changes from 64.7° (*trans*) to 0.1° (*transition state*) to -55.9° (*cis*). Whereas for the rotational transition state of **Azo**, the relevant conformation coordinate is the dihedral angle  $\angle$  (C-N=N-C), that changes from in-plane 180° (*trans*) to 91° (*transition state*) to 46° (*cis*). Note that the relative energies were calculated in the absence of SAM matrix and that the values could vary due to the steric effects from the matrix. All the calculations were performed using UB3LYP density functional theory and 6-31+G(d) basis sets by the Gaussian 09 suite of

programs. Similar results were found in both theoretical<sup>41</sup> and experimental<sup>47</sup> studies based on substituted azobenzene adsorbed on Au{111} surfaces.

It has previously been shown that anionic forms of substituted azobenzenes can undergo *trans* to *cis* isomerization of single molecules through a transient ion resonance state.<sup>41,47</sup> However, in that case the switching events were not precisely controlled due to surface diffusion of the adsorbed azobenzene. Moreover, application of the same voltage pulse yielded different conformations in different situations.<sup>47</sup> Here, we restricted the motion of the azobenzene moiety by decoupling it from the Au substrate via attachment of a saturated tether, thereby eliminating stochastic switching events; thus, the geometric changes in the molecule can only be attributed to isomerization. Moreover, we induced reversible isomerization between the *trans* and *cis* conformations resulting in controllable bistable changes in the conductivity of the 1D chains (Figs. 3.4A, B).

Tunneling electrons can transiently reduce the **Azo** molecules, then tunnel to the substrate through the tether or delocalize to electronically coupled neighboring molecules within the **Azo** chain. Since the entire chain switched OFF on timescales faster than the imaging timescale (milliseconds to minutes), we infer that delocalization of electrons occurs on a faster timescale, such that electrons are able to populate antibonding orbitals of all azobenzene moieties in the chain to some extent. Since tunneling is a localized phenomenon,<sup>48</sup> and since we observe isomerization of molecules (only) in the 1D wire far removed from the position of the STM tip, we deduce that the electrons delocalize along the chain via the **Azo**  $\pi$  cloud overlap, thereby creating a negative ion resonance state of the 1D *chain* and thus resulting in the concerted isomerization of all the molecules. Further evidence that delocalized electrons lead to isomerization can be observed in Figures 3.2A and 3.2B. The **1R** chain manipulated by the STM

tip completely isomerized; however, a second **1R** chain (red box in Fig. 3.2) that is decoupled from the first by  $\sim 14$  Å separation did *not* isomerize. This is in contrast to the results observed by Alemani *et al.* where the electric field from the STM probe tip induced isolated isomerization events in molecules that were as far away as 500 Å.<sup>24</sup> Also, we considered the possibility that a conformational change in one molecule mechanically induces isomerization in its neighboring molecule (in analogy to dominos or a cascade effect).<sup>36,49</sup> However, this mechanism is not consistent with our results, as azobenzene isomerization is endothermic;<sup>41,50</sup> changes in conformation of one molecule cannot provide sufficient free energy to drive the isomerization of so many neighboring molecules.

A 2.0 V sample bias was also applied to the **2R** chains, for 5 min. Note that even though the **2R** chain shown is  $\sim 130$  Å long, when the elevated bias was applied to one end, it switched OFF completely (Figs. 3.5A and 3.5B). After the **2R** chain was switched OFF, the sample was imaged with scanning parameters of  $V_s = 1.0$  V and  $I_t = 1$  pA. In this case, molecules switched back to the ON state after 30 min at room temperature via thermal relaxation (Fig. 3.5C).<sup>51</sup> Line scans showing the apparent changes in height can be seen below the respective STM images. Isomerization of **Azo** chains was observed to be a completely reversible and repeatable process. That such long chains switched in a concerted fashion, whereas decoupled **1R** chains (such as the one in the red box in Fig. 3.2A) did not, is consistent with our hypothesis that delocalized electrons in molecular chains induce isomerization at long range, but molecules electronically decoupled from the chains are not isomerized.

Typical manipulation times required to switch the **1R** and **2R** chains were 2 and 5 min, respectively. We attribute this variation in time to the position of the tip above the molecules, to the lifetime of switching event of the azobenzene moiety within the chains, and to the



thicknesses of the chains. The custom-built STM operating in ambient conditions had a lateral drift of  $<0.5 \text{ \AA}/\text{min}$ ;<sup>5</sup> thus, the position of the STM probe drifts to some extent during the stimulation period of 5 min but still remains positioned over only one molecule.

Photoisomerization of the chains was also investigated and the efficiencies of switching **1R** and **2R** chains were compared with those of isolated single molecules. It was observed that the photoswitching efficiency of tethered azobenzene decreases when arranged in linear assemblies and with increasing chain thickness. Isolated single-molecule photoisomerization was observed over tens of minutes of UV light irradiation in our previous study.<sup>5</sup> We observed that the switching efficiencies of 1D molecular chains are significantly lower than those of isolated single molecules. The molecules in the narrowest 1D chains switched after an average 30 min of UV light irradiation. Again, all the molecules in coupled chains switched in concert (Figs. 3.6A, B), in stark contrast to single-molecule isomerization, where photoisomerization occurred independently for isolated molecules during UV exposure. All the molecules in 1D chains exhibit *trans* to *cis* isomerization. The molecules in chains can switch back to *trans* conformations via thermal relaxation at room temperature (Fig. 3.6C). It was observed that the switching efficiency further decreased with increasing chain thickness. Figures 3.6D and 3.6E show an example of photoisomerization of a **2R** chain. It was found that the wider **2R** chains exhibit *partial* switching; the molecules shown in the red box did not all isomerize. We attribute this difference to local degradation of the SAM matrix domain boundary due to prolonged exposure to UV light.<sup>52</sup> Due to this degradation, molecules aggregate and form 2D islands, presumably leading to steric hindrance and thus preventing coordinated isomerization. The parts of the chain that did isomerize exhibited concerted switching similar to **1R** chains. Thus,

molecular assembly and the local environment influence the efficiency of photoswitching of the chains.

### **3.4 CONCLUSIONS AND FUTURE PROSPECTS**

Based on the straightforward and robust nature of the 1D structure growth process, the techniques demonstrated here could be applied to fabricate and to study novel supramolecular assemblies by tuning the functional moieties and coupling of the functional molecules. Further, the interchain electronic coupling could be measured by studying the likelihood that neighboring chains could be isomerized when one is excited. Most importantly, electronic coupling between molecules can be used to induce concerted action of precisely assembled molecules.

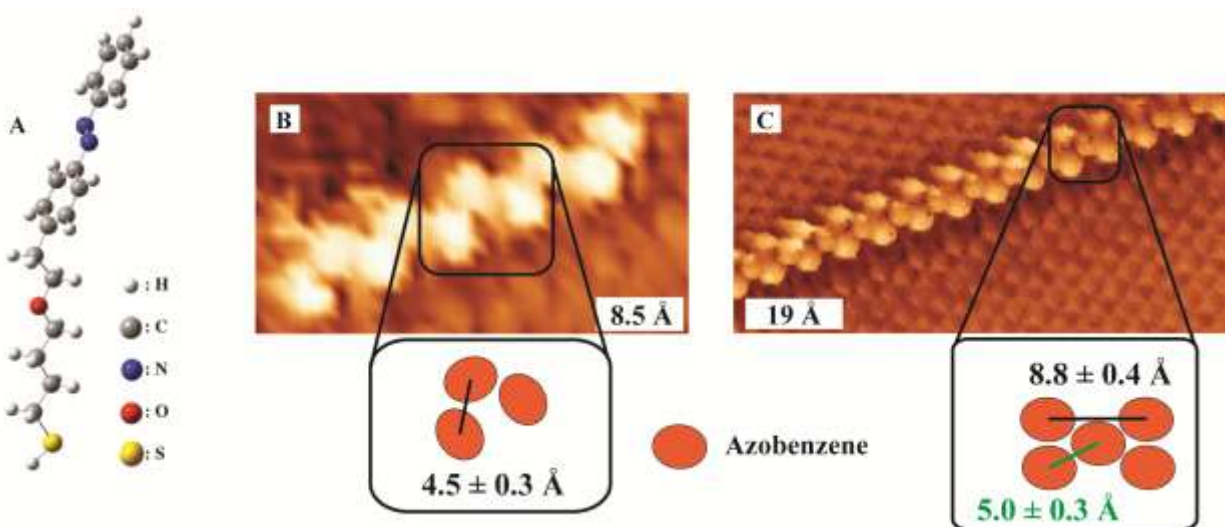


**Figure 3.1.** (A) Structure of the azobenzene-functionalized molecule (4-[2-(4-phenylazo-phenyl)-ethoxy]-butane-1-thiol), **Azo**. Scanning tunneling microscope images of (B) single-row chain of **Azo** molecules assembled at the domain boundaries of a decanethiol self-assembled monolayer matrix on Au{111} with a nearest neighbor distance of  $4.5 \pm 0.3 \text{ \AA}$  (see inset) and (C) double-row chain of **Azo** molecules. Inset: Herringbone arrangements with center-to-center intermolecular distances of  $8.8 \pm 0.4 \text{ \AA}$  and  $5.0 \pm 0.3 \text{ \AA}$  between the farthest and the nearest neighbors in the repeating unit cell. Imaging conditions:  $V_s = 1.0 \text{ V}$  and  $I_t = 1 \text{ pA}$ .

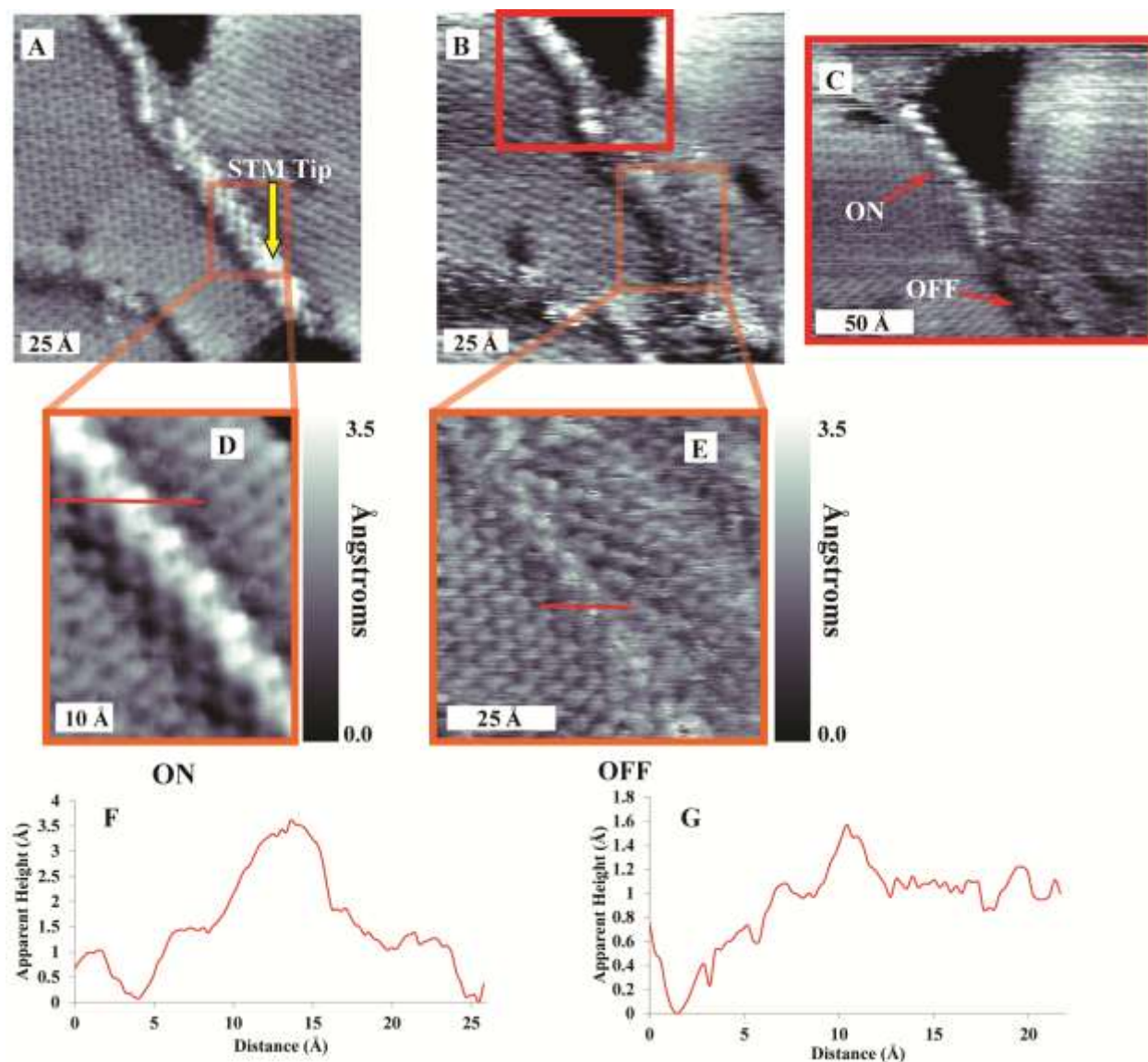


**Figure 3.2.** Scanning tunneling microscope images following tunneling-electron-induced isomerization of a 1D chain of **Azo**. (A) All the molecules are initially found in their thermodynamically stable *trans* (ON) state. The sample bias was then increased to 2.0 V and the scanning tunneling microscope probe tip positioned over the chain at the position indicated (yellow arrow) for 2 min. (B) All the coupled molecules in the chain switched to the *cis* conformation, as is evident by the change in the apparent heights of the molecules. (C) A nearby chain that was not electronically coupled (red box) did not isomerize. (D, E) High-resolution

images of the 1D chain before and after isomerization. Line scans (F) before and (G) after isomerization, showing apparent reduction in height with respect to the surrounding self-assembled monolayer matrix (red lines from D and E). Imaging conditions:  $V_s = 1.0$  V and  $I_t = 1$  pA.

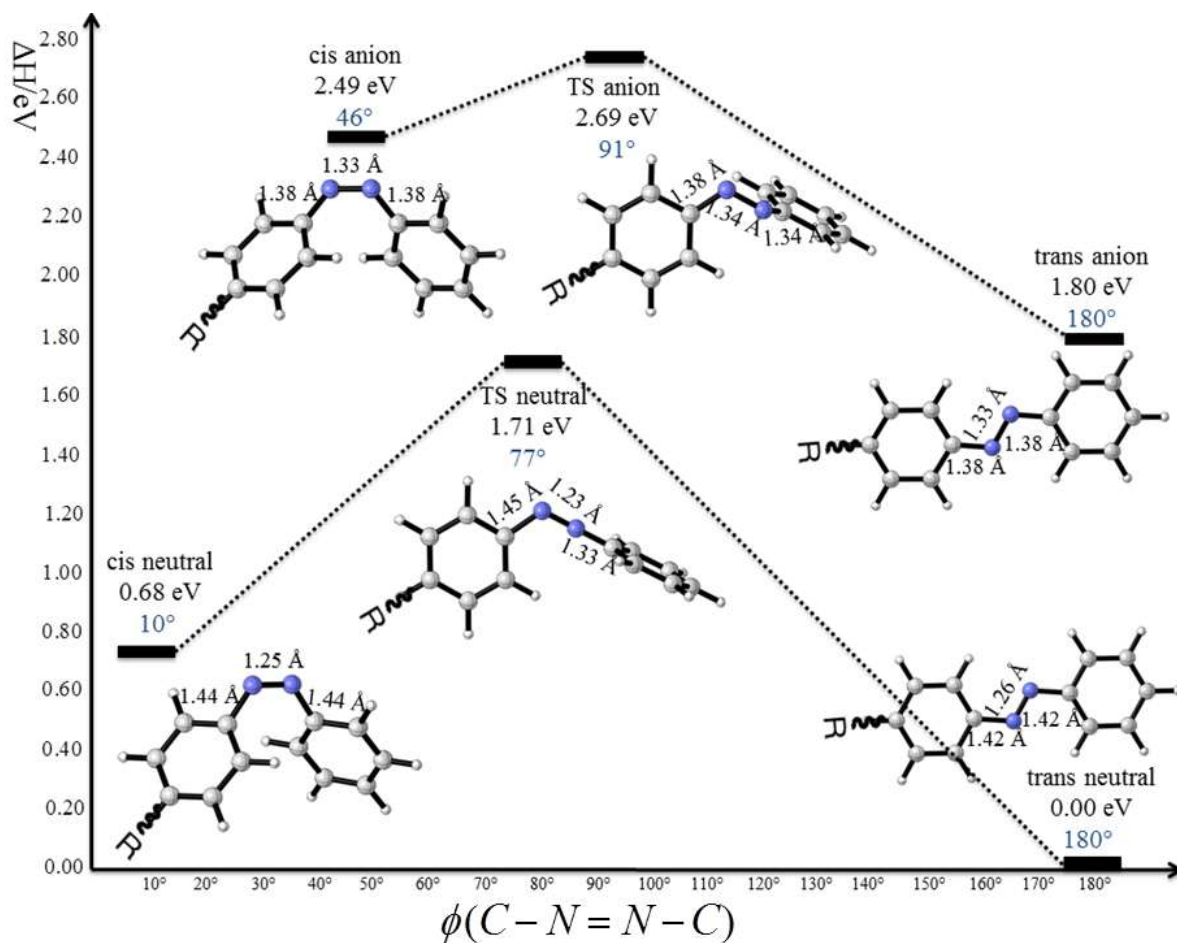


**Figure 3.3.** The transition states of neutral **Azo**, following an inversion mechanism for isomerization with a calculated barrier of 1.71 eV and anionic **Azo**, following a rotation mechanism for isomerization with a calculated barrier of 0.89 eV. The tether (**R**) has been removed in the plot for clarity. The dihedral angles are shown below the energy levels of each state.

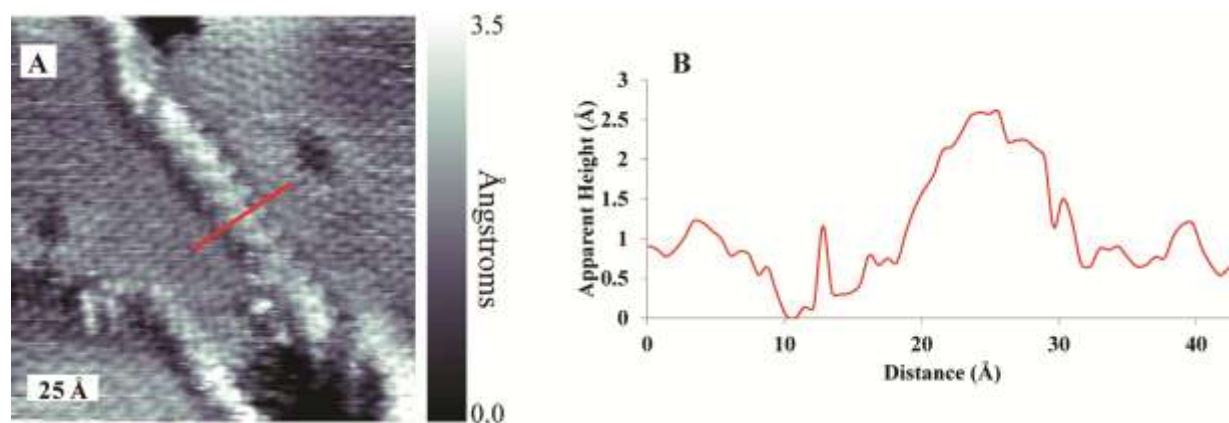


**Figure 3.4.** (A) Scanning tunneling microscope image after the chain switches back to the *trans* conformation via thermal relaxation. (B) Line scan showing increment in apparent height with respect to surrounding matrix (See red line from Fig. 3.4A). Image conditions:  $V_s = 1.0$  V and  $I_t = 1$  pA.

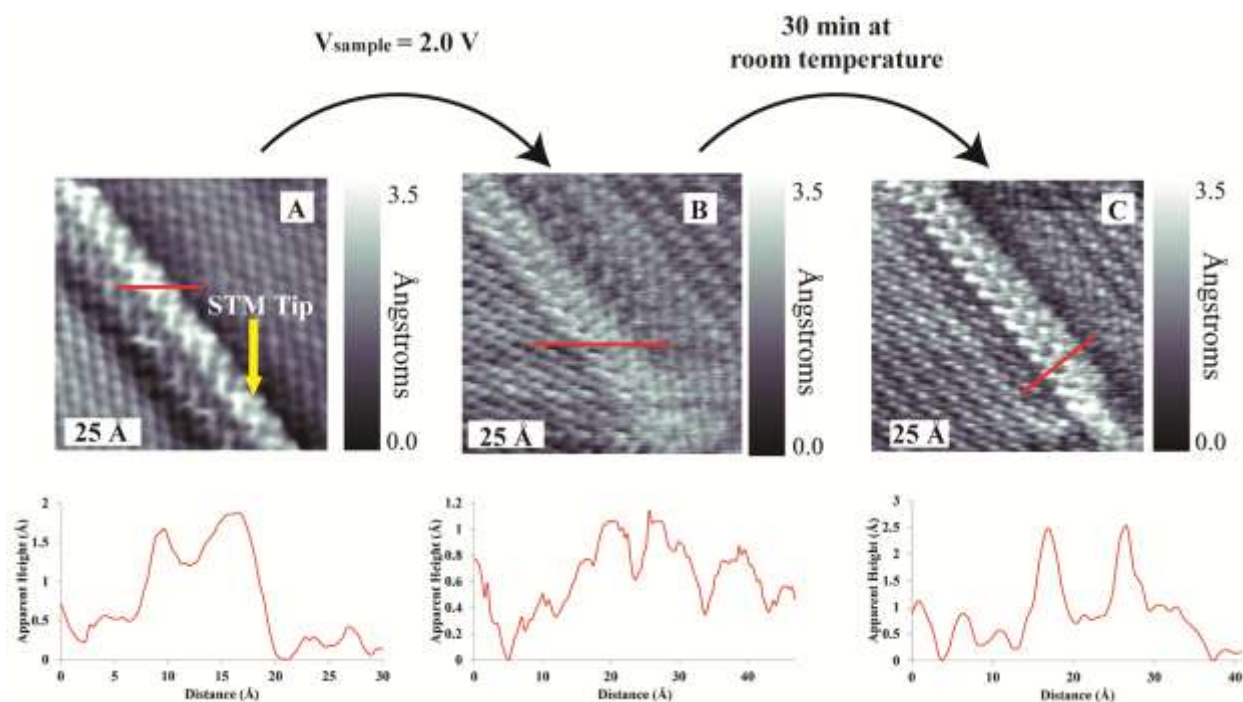


**Figure 3.5.** Double-row chains (A) Before isomerization, all the molecules are in the more stable *trans* conformation. Sample bias was increased to 2.0 V and the scanning tunneling microscope probe tip was positioned over the chain (yellow arrow) for 5 min. (B) After isomerization, all the molecules switch OFF (*cis* conformation) and (C) molecules isomerize back to their *trans* conformation after 30 min at room temperature via thermal relaxation. Imaging conditions:  $V_s = 1.0$  V and  $I_t = 1$  pA.



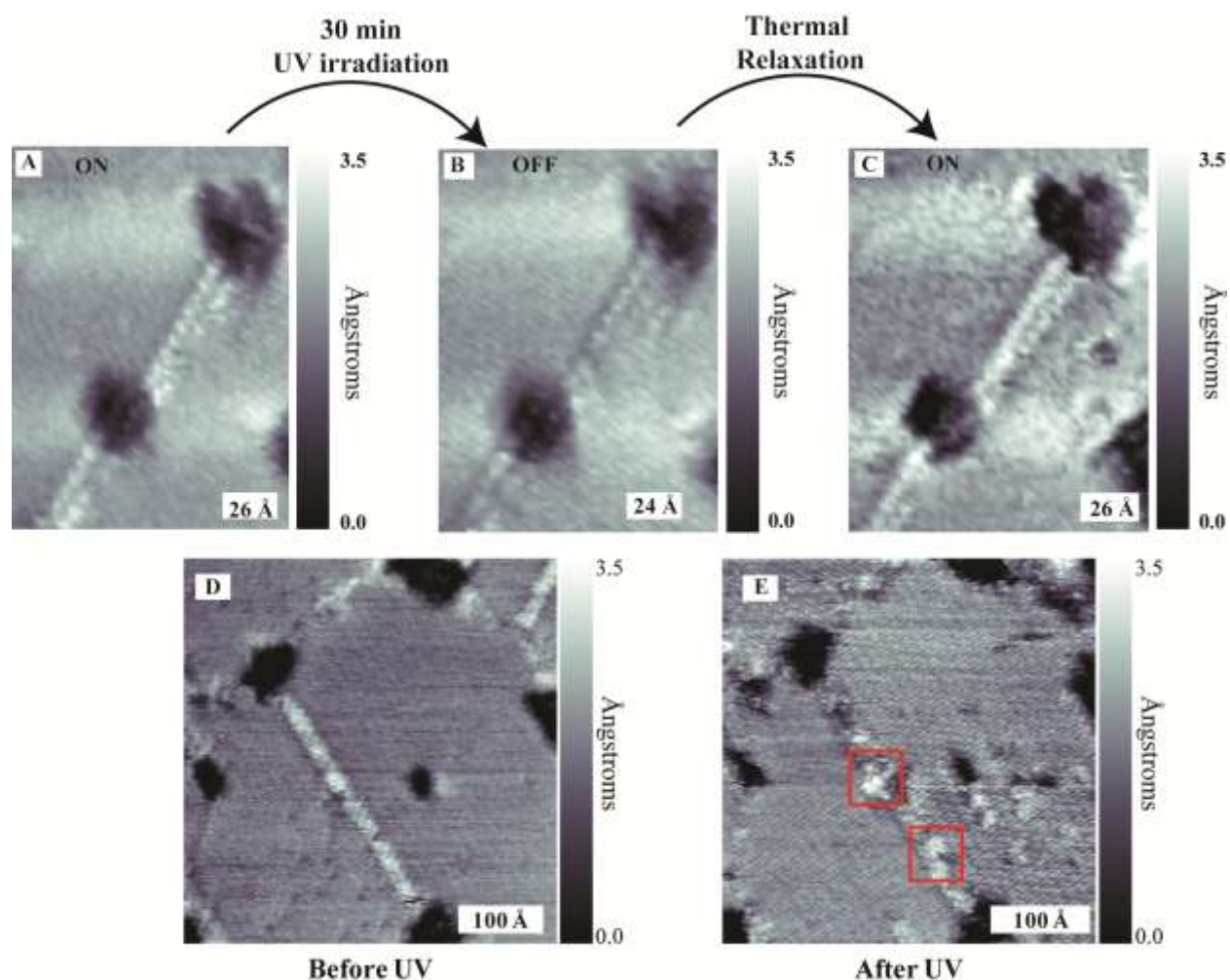


**Figure 3.6.** Scanning tunneling microscope images following the photoinduced isomerization of chains: Both **1R** and **2R** chains switched OFF upon irradiation with UV light for 30 min at  $\sim 12 \text{ mW/cm}^2$ . (A) A chain in its initial ON state, (B) All molecules in the **1R** chain switched OFF (*cis* conformation) after 30 min UV irradiation, (C) The chain switches back to ON (*trans* conformation) via thermal relaxation after 30 min at room temperature. (D) Initial state of **2R** chain before UV irradiation. (E) Parts of the **2R** chain did not switch OFF (red squares), presumably due to steric hindrance. All scanning tunneling microscope images were recorded at  $V_s = 1 \text{ V}$  and  $I_t = 1 \text{ pA}$ .

### 3.5 REFERENCES

1. Donhauser, Z. J.; Mantooth, B. A.; Kelly, K. F.; Bumm, L. A.; Monnell, J. D.; Stapleton, J. J.; Price, D. W.; Rawlett, A. M.; Allara, D. L.; Tour, J. M.; Weiss, P. S. *Science* **2001**, 292, 2303-2307.
2. Feringa, B. L., *Molecular Switches*. Wiley-VCH, Weinheim, Germany: 2001.
3. Henzl, J.; Mehlhorn, M.; Gawronski, H.; Rieder, K. H.; Morgenstern, K. *Angew. Chem. Int. Ed.* **2006**, 45, 603-606.
4. Comstock, M. J.; Levy, N.; Kirakosian, A.; Cho, J. W.; Lauterwasser, F.; Harvey, J. H.; Strubbe, D. A.; Frechet, J. M. J.; Trauner, D.; Louie, S. G.; Crommie, M. F. *Phys. Rev. Lett.* **2007**, 99, 38301.
5. Kumar, A. S.; Ye, T.; Takami, T.; Yu, B. C.; Flatt, A. K.; Tour, J. M.; Weiss, P. S. *Nano Lett.* **2008**, 8, 1644-1648.
6. Ye, T.; Kumar, A. S.; Saha, S.; Takami, T.; Huang, T. J.; Stoddart, J. F.; Weiss, P. S. *ACS Nano* **2010**, 4, 3697-3701.
7. Tseng, G. Y.; Ellenbogen, J. C. *Science* **2001**, 294, 1293-1294.
8. Ratner, M. *Nature* **2005**, 435, 575-577.
9. Weiss, P. S. *Acc. Chem. Res.* **2008**, 41, 1772-1781.
10. Li, D.; Paxton, W. F.; Baughman, R. H.; Huang, T. J.; Stoddart, J. F.; Weiss, P. S. *MRS Bull.* **2009**, 34, 671-681.
11. Eigler, D. M.; Schweizer, E. K. *Nature* **1990**, 344, 524-526.
12. Avouris, P. *Acc. Chem. Res.* **1995**, 28, 95-102.
13. Wallis, T. M.; Nilius, N.; Ho, W. *Phys. Rev. Lett.* **2002**, 89, 236802.

14. Takami, T.; Ye, T.; Pathem, B. K.; Arnold, D. P.; Sugiura, K.-i.; Bian, Y.; Jiang, J.; Weiss, P. S. *J. Am. Chem. Soc.* **2010**, *132*, 16460-16466.
15. Yokoyama, T.; Yokoyama, S.; Kamikado, T.; Okuno, Y.; Mashiko, S. *Nature* **2001**, *413*, 619-621.
16. Weiss, P. S. *Nature* **2001**, *413*, 585-586.
17. Whitesides, G. M.; Grzybowski, B. *Science* **2002**, *295*, 2418-2421.
18. Barth, J. V.; Costantini, G.; Kern, K. *Nature* **2005**, *437*, 671-679.
19. Saavedra, H. M.; Mullen, T. J.; Zhang, P. P.; Dewey, D. C.; Claridge, S. A.; Weiss, P. S. *Rep. Prog. Phys.* **2010**, *73*, 036501.
20. Feringa, B. L.; van Delden, R. A.; Koumura, N.; Geertsema, E. M. *Chem. Rev.* **2000**, *100*, 1789-1816.
21. Katsonis, N.; Lubomska, M.; Pollard, M. M.; Feringa, B. L.; Rudolf, P. *Prog. Surf. Sci.* **2007**, *82*, 407-434.
22. Kim, M.; Hohman, J. N.; Cao, Y.; Houk, K. N.; Ma, H.; Jen, A. K. Y.; Weiss, P. S. *Science* **2011**, *331*, 1312-1315.
23. Joachim, C.; Gimzewski, J. K.; Aviram, A. *Nature* **2000**, *408*, 541-548.
24. Alemani, M.; Peters, M. V.; Hecht, S.; Rieder, K. H.; Moresco, F.; Grill, L. *J. Am. Chem. Soc.* **2006**, *128*, 14446-14447.
25. Byoung-Young, C.; Se-Jong, K.; Seungchul, K.; Hajin, K.; Hyo Won, K.; Young Jae, S.; Ihm, J.; Kuk, Y. *Phys. Rev. Lett.* **2006**, *96*, 156106.
26. Moresco, F.; Meyer, G.; Rieder, K. H.; Tang, H.; Gourdon, A.; Joachim, C. *Phys. Rev. Lett.* **2001**, *86*, 672-675.
27. Safiei, A.; Henzl, J.; Morgenstern, K. *Phys. Rev. Lett.* **2010**, *104*, 216102.

28. Lang, N. D.; Avouris, P. *Phys. Rev. Lett.* **2000**, *84*, 358-361.
29. Kirczenow, G.; Piva, P. G.; Wolkow, R. A. *Phys. Rev. B Condens. Matter* **2005**, *72*, 245306-1-17.
30. Geng, W. T.; Oda, M.; Nara, J.; Kondo, H.; Ohno, T. *J. Phys. Chem. B* **2008**, *112*, 2795-2800.
31. Lopinski, G. P.; Wayner, D. D. M.; Wolkow, R. A. *Nature* **2000**, *406*, 48-51.
32. Akai-Kasaya, M.; Shimizu, K.; Watanabe, Y.; Saito, A.; Aono, M.; Kuwahara, Y. *Phys. Rev. Lett.* **2003**, *91*, 255501.
33. Temirov, R.; Soubatch, S.; Luican, A.; Tautz, F. S. *Nature* **2006**, *444*, 350-353.
34. Chen, L.; Li, H.; Wee, A. T. S. *Nano Lett.* **2009**, *9*, 4292-4296.
35. Hugel, T.; Holland, N. B.; Cattani, A.; Moroder, L.; Seitz, M.; Gaub, H. E. *Science* **2002**, *296*, 1103-1106.
36. Zhang, C.; Du, M. H.; Cheng, H. P.; Zhang, X. G.; Roitberg, A. E.; Krause, J. L. *Phys. Rev. Lett.* **2004**, *92*, 158301.
37. Eigler, D. M.; Weiss, P. S.; Schweizer, E. K.; Lang, N. D. *Phys. Rev. Lett.* **1991**, *66*, 1189-1192.
38. Cygan, M. T.; Dunbar, T. D.; Arnold, J. J.; Bumm, L. A.; Shedlock, N. F.; Burgin, T. P.; Jones, L.; Allara, D. L.; Tour, J. M.; Weiss, P. S. *J. Am. Chem. Soc.* **1998**, *120*, 2721-2732.
39. Zimmerman, G.; Chow, L. Y.; Paik, U. J. *J. Am. Chem. Soc.* **1958**, *80*, 3528-3531.
40. Rau, H.; Luddecke, E. *J. Am. Chem. Soc.* **1982**, *104*, 1616-1620.
41. Fuchsel, G.; Klamroth, T.; Dokic, J.; Saalfrank, P. *J. Phys. Chem. B* **2006**, *110*, 16337-16345.

42. Donhauser, Z. J.; Price, D. W.; Tour, J. M.; Weiss, P. S. *J. Am. Chem. Soc.* **2003**, *125*, 11462-11463.
43. Caldwell, W. B.; Campbell, D. J.; Chen, K. M.; Herr, B. R.; Mirkin, C. A.; Malik, A.; Durbin, M. K.; Dutta, P.; Huang, K. G. *J. Am. Chem. Soc.* **1995**, *117*, 6071-6082.
44. Schultz, T.; Quenneville, J.; Levine, B.; Toniolo, A.; Martinez, T. J.; Lochbrunner, S.; Schmitt, M.; Shaffer, J. P.; Zgierski, M. Z.; Stolow, A. *J. Am. Chem. Soc.* **2003**, *125*, 8098-8099.
45. Chen, E. C. M.; Herder, C.; Chen, E. S. *Chem. Phys. Lett.* **2007**, *440*, 180-186.
46. Singh-Miller, N. E.; Marzari, N. *Phys. Rev. B* **2009**, *80*.
47. Henningsen, N.; Franke, K. J.; Torrente, I. F.; Schulze, G.; Priewisch, B.; Ruck-Braun, K.; Dokic, J.; Klamroth, T.; Saalfrank, P.; Pascual, J. I. *J. Phys. Chem. C* **2007**, *111*, 14843-14848.
48. Binnig, G.; Rohrer, H.; Gerber, C.; Weibel, E. *Phys. Rev. Lett.* **1982**, *49*, 57-61.
49. Heinrich, A. J.; Lutz, C. P.; Gupta, J. A.; Eigler, D. M. *Science* **2002**, *298*, 1381-1387.
50. Nagele, T.; Hoche, R.; Zinth, W.; Wachtveitl, J. *Chem. Phys. Lett.* **1997**, *272*, 489-495.
51. Liu, Z. F.; Morigaki, K.; Enomoto, T.; Hashimoto, K.; Fujishima, A. *J. Phys. Chem.* **1992**, *96*, 1875-1880.
52. Ballav, N.; Weidner, T.; Zharnikov, M. *J. Phys. Chem. C* **2007**, *111*, 12002-12010.

## **CHAPTER 4**

### ***DIRECTED ASSEMBLY OF PRECISE SUPRAMOLECULAR STRUCTURES TO TUNE THEIR DIPOLE-DIPOLE INTERACTIONS***

## 4.1 INTRODUCTION

Building individual molecules into functional assemblies on surfaces opens up new vistas for controlling the properties and exploring supramolecular nanodevice concepts.<sup>1-11</sup> In such assemblies, the structural, optical, and electronic properties of the molecules are strongly affected by intermolecular interactions.<sup>12-19</sup> Therefore, measuring, understanding, and controlling these interactions is imperative for achieving and exploiting the desired precise supramolecular structures and properties of functional molecular devices.<sup>7</sup> However, dealing with these effects is often challenging because of the difficulties in tuning and measuring supramolecular structures with precision and in correlating the properties with intermolecular interactions such as van der Waals interactions, hydrogen-bonding, and metal-ligand interactions.<sup>20</sup> Even greater complexity arises when the external stimuli used for driving the molecular devices induce additional interactions such as optically induced dipole-dipole interactions.<sup>21,22</sup> As a result, the molecular systems and analytical tools that enable us to tune the supramolecular structure precisely and to probe and to separate each of the intermolecular interactions are at the core of our understanding and development of supramolecular devices. In this chapter, our self-assembly strategy to form precise assemblies of azobenzene-functionalized molecules with single-molecule precision in a controlled nanoscale environment will be discussed.<sup>23,24</sup> As an initial demonstration of these assemblies as a platform for understanding intermolecular interactions, we probe tunable light-induced dipole-dipole interactions. We apply SERS and STM to record the vibrational spectra of the azobenzene-functionalized molecules and to measure supramolecular structures, respectively. Due to its high selectivity and sensitivity, SERS is uniquely suited to probe assemblies of supramolecular structures by monitoring changes in vibrational spectra.<sup>25-32</sup> We reveal the tunability of the dipole-dipole interactions and their effects on the molecular signals by analyzing

the dependence of the SERS spectra and the molecular polarizability on the supramolecular structure. The experimental observations are supported by calculations based on density functional theory (DFT) and an analytical model.

## 4.2 METHODS

The chemicals dodecanethiolate, decanethiolate (Sigma-Aldrich, St. Louis, MO, USA), 200-proof ethanol (Pharmco, Brookfield, CT, USA), and 4-(1-mercaptopundec-11-yloxy)-azobenzene (ProChimia Surfaces, Poland, **Azo1**) were used as received. The Tour group at Rice University synthesized compound 4-[2-(4-phenylazo-phenyl)-ethoxy]-butane-1-thiol (**Azo2**). Cylindrical nanoholes in square arrays were fabricated into the Au{111} on mica substrates (Agilent Technologies) with focused ion beam (FIB) lithography (Nova 600 NanoLab, FEI Company, Hillsboro, OR, USA). Self-assembled monolayers were formed on the nanohole-patterned Au surfaces after annealing the substrates with a hydrogen flame. For SAMs with tunable structures of azobenzene-functionalized molecules, an initial sample is prepared by immersing a Au substrate in a 1 mM ethanolic solution of alkanethiol for 1 min. The sample is then rinsed with ethanol, blown dry with nitrogen, and immersed in a 0.2 mM ethanolic solution of azobenzene for 4 min, followed by vapor annealing for different time.<sup>33</sup> Vapor annealing of the SAMs was done at 80 °C over a 1 mM ethanolic solution of alkanethiol. For control experiments, samples that maintained their structure during vapor annealing were prepared *via* co-adsorption from solution, with the result that the azobenzene-functionalized molecules remained within the domains of the monolayer matrix.

All STM measurements were performed in a custom STM under ambient conditions.<sup>24</sup> All the images were recorded at sample bias  $V_s = 1.0$  V, and tunneling current  $I_t = 1$  pA.



Raman analyses were performed in a backscattering geometry in a confocal configuration at room temperature with polarized light using a Renishaw inVia Raman system (Renishaw, Inc., Chicago, Illinois, USA). A 632.8 nm He–Ne laser was used as the Raman excitation source; the laser power, beam diameter, and the integration time were 17 mW, 1  $\mu$ m, and 150 s, respectively.

All DFT calculations were performed within the NWCHEM software package<sup>34</sup> and employed the B3LYP functional and a 6-31G\* basis set.<sup>35</sup> The B3LYP/6-31G\* frequencies were scaled by 0.9614.<sup>36</sup>

### 4.3 RESULTS AND DISCUSSIONS

Figure 4.1a shows a cross-sectional view of azobenzene-functionalized molecules in SAM matrices of thiolates on Au{111}, illustrating the effects of light-induced intermolecular interactions on the Raman signal. The Au thin films, grown epitaxially on mica substrates, provide atomically flat terraces for high-quality self-assembly and STM imaging of the molecules. Cylindrical nanoholes in square arrays are fabricated in the Au films (inset in Fig. 4.1a). The nanoholes have a diameter of 175 nm; the array period is varied within a range from 280 to 450 nm to tune the plasmon resonances to the excitation laser wavelength for maximizing the enhancement of azobenzene Raman signals. Two types of azobenzene-functionalized molecules were tested in this study, **Azo1** and **Azo2**, with matrix molecules of dodecanethiolate (**C12**) and decanethiolate (**C10**) for **Azo1** and **Azo2**, respectively (Fig. 4.1b).<sup>24,31</sup>

Figure 4.1c illustrates how we tune the structures (from two isolated single molecules to a dimer in this example) of azobenzene-functionalized molecules inserted in alkanethiol matrices using the vapor-annealing method.<sup>33,37,38</sup> An initial sample is prepared by immersing a flame-

annealed Au substrate with nanoholes in a 1 mM ethanolic solution of alkanethiol for 1 min. This results in the formation of highly disordered domains of alkanethiol (indicated as grey dots). The sample is then rinsed with ethanol, blown dry with nitrogen, and immersed in a 0.2 mM ethanolic solution of azobenzene for 4 min. This results in isolated single azobenzene-functionalized molecules (indicated as blue dots) preferentially bound at alkanethiol SAM domain boundaries and substrate vacancy islands. To tune the structure, we vapor anneal the sample at 80 °C over the 1 mM ethanolic solution of alkanethiol. Vapor annealing inserts extra alkanethiol matrix molecules into the initial SAM and mobilizes the isolated single azobenzene-functionalized molecules to form dimers and larger structures.<sup>33,37,38</sup>

To track the changes in the supramolecular structure of azobenzene assemblies, we employed STM to image with molecular resolution. Figure 4.2 shows a series of STM images of **Azo2** in **C10** as a function of vapor-annealing time. In STM images, the azobenzene-functionalized molecules protrude from the surrounding matrix with an apparent height of  $\sim 2$  Å, consistent with our previous work.<sup>24</sup> Figure 4.2a is from the sample without annealing, revealing randomly distributed single, dimer, trimer, and larger clusters with the numbers of azobenzene-functionalized molecules,  $n = 4-7$ . After vapor annealing for 30 min, some of the azobenzene-functionalized molecules transformed into chain structures ( $n > 7$ ) where the molecules are aligned in herringbone structures (Fig. 4.2b). The lengths of the chains varied between 30 and 200 Å depending on the initial sizes of the alkanethiol domains. Extending the annealing time to 60 min increased the percentage of the azobenzene-functionalized molecules that were transformed into chains (Fig. 4.2c). Annealing the sample for 120 min transformed essentially *all* of the azobenzene-functionalized molecules into chains (Fig. 4.2d). To follow the annealing-induced changes in the molecular arrangements in the assemblies, we count the numbers of each

structure in the STM images and plot them as a function of annealing time and structure (Fig. 4.2e). Figure 4.2e reveals that increasing the annealing time leads to increases in the number of azobenzene-functionalized molecules forming chain structures and dramatic decreases in the population of isolated single molecules and clusters.

To probe the dipole-dipole interactions of azobenzene and their enablement by changes in supramolecular structure, we recorded a series of SERS spectra from the sample as a function of annealing time. To exclude the heating effects on the SERS spectra,<sup>39</sup> each measurement was taken after the sample was cooled down for 30 min following vapor annealing. Figure 4.3a shows the Raman spectra recorded from an **Azo1** sample after vapor annealing for different time periods (indicated by the number near each spectrum, in minutes). All the spectra show five peaks, which we assign as the C1, C2, C3, C4, and C5 modes.<sup>31</sup> To quantitate the effects of vapor annealing on the SERS spectra, we calculated the area intensities of the peaks by curve fitting using Wire 3.2 software (Renishaw, Inc.) and plotted the area intensities as a function of annealing time (Fig. 4.3b). All the modes exhibit decreased peak area intensities with increasing annealing time. However, the C5 mode decreases less than the rest of the modes, specifically during the initial 2 h of annealing when the major changes in supramolecular structure occur. Our previous study revealed that C5 is a mixture of the three moderately intense modes combining the NN stretch, the minor in-plane ring modes, and alkyl HCH bending.<sup>31</sup> This mode mixture makes C5 less sensitive to the dipole-dipole interactions among **Azo1** molecules. The STM studies revealed that vapor annealing could involve direct exchange of the **Azo1** molecules with **C12** vapor molecules or desorption of **Azo1** followed by opportunistic adsorption of **C12** vapor-phase molecules at the vacant substrate sites.<sup>34</sup> This result indicates that, although the annealing-induced loss of **Azo1** molecules can cause a decrease in the SERS intensity, the

dipole-dipole interactions account for the larger decrease in the SERS intensity for modes C1, C2, C3, and C4. The SERS spectra of the **Azo2** samples show similar evolution.

To test if the decreased peak area intensities in the SERS spectra were correlated to the evolution of supramolecular structure, we performed control experiments with samples that maintained their structure during vapor annealing. Figure 4.4a shows a STM image of the sample before annealing. The protruding azobenzene-functionalized molecules are found within the matrix domains. A STM image of the sample after vapor annealing for 120 min is shown in Fig. 4.4b. In contrast to the chains observed in Fig. 4.2d, the azobenzene-functionalized molecules in Fig. 4.4b remained isolated within the matrix. Figure 4.4c shows the Raman spectra recorded from the control sample after vapor annealing as a function of time (indicated by the number near each spectrum, in minutes). The spectra exhibit the same modes as those in Fig. 4.3a. However, in contrast to Fig. 4.3b, Fig. 4.4d shows that the peak area intensities increase as a function of annealing time for the control sample. The increases are likely due to increases in the tilt angles of azobenzene-functionalized molecules as the matrix gets tighter due to the vapor annealing. This would lead to the long axis of the azobenzene moiety aligning more closely to the surface normal and thus experiencing stronger electromagnetic enhancement.

We use density functional theory (DFT) to calculate the effects of supramolecular structure on the Raman spectra of azobenzene. An azobenzene pair was used as a model and the inter-azo distances from the STM analyses (Fig. 4.2) were used as references for setting the distances in the calculations. We define the inter-azo distance as the center-to-center length of the two closest azobenzene molecules. The dimer, trimer, clusters ( $n=4-7$ ), and chains have intermolecular distances of  $5.6 \pm 0.2$  Å,  $5.4 \pm 0.3$  Å,  $5.3 \pm 0.3$  Å, and  $4.4 \pm 0.1$  Å, respectively.

All DFT calculations were performed within the NWChem software package<sup>34</sup> and employed the B3LYP functional and a 6-31G\* basis set.<sup>35</sup> To represent the various orientations of azobenzene in the experiments, we construct three basic types of pair configurations: face-to-face (FF), face-to-side (FS), and side-to-side (SS) (Fig. 4.5a). We simulated the Raman spectra from each configuration as a function of the inter-molecular distance,  $R$ , ranging from 11.0 Å to roughly the van der Waals distances. Figure 4.5b shows the Raman spectra for the FF configuration, which exhibit reduced spectral intensity with decreased  $R$ . The calculated spectra match experimental data (Fig. 4.3a) with the five major modes indicated as C1, C2, C3, C4, and C5. The spectra for FS and SS configurations are similar to those for FF. In Figs. 4.5c-e, we have plotted the Raman differential cross section of modes C1-C5 as a function of inter-azo distance for FF, FS, and SS configurations, respectively. These trends match the experimental results (Fig. 4.3b).

To understand the physical mechanism behind the observed relationship between the Raman spectral intensity and inter-azo distance, we examine the trends in the polarizability and the Raman intensity as a function of inter-azo distance using a simple analytical model<sup>40,41</sup> and DFT. The analytical models describe the parallel and perpendicular interactions of two azobenzene molecules by considering them as two interaction point polarizable objects. In this way, the total polarizability of the complex can be written as:

$$\alpha_{\parallel} = \frac{\alpha_1 + \alpha_2 + \frac{4\alpha_1\alpha_2}{R^3}}{1 - \frac{4\alpha_1\alpha_2}{R^6}} \quad (1)$$

and

$$\alpha_{\perp} = \frac{\alpha_1 + \alpha_2 - \frac{2\alpha_1\alpha_2}{R^3}}{1 - \frac{\alpha_1\alpha_2}{R^6}}, \quad (2)$$

where  $\alpha_1$  and  $\alpha_2$  are the polarizability of the first and second azobenzene molecule, respectively, and  $R$  is the inter-azo distance. As shown in Fig. 4.5a the y-axis is the parallel axis while x- and z-axes are the perpendicular axes. Figure 4.6 shows the diagonal components of the polarizability tensor and the isotropic polarizability of the azobenzene pairs as calculated with DFT and the analytical model. The two methods are in good agreement. The perpendicular elements of the polarizability tensor,  $\alpha_{xx}$  and  $\alpha_{zz}$ , decrease at small inter-azo distances while the parallel element,  $\alpha_{yy}$ , increases, as the analytical model (eqs. (1) and (2)) predicts. The isotropic polarizability is an average of the diagonal components of the polarizability tensor. As seen in Fig. 4.6d, the perpendicular interactions dominate and reduce the polarizability for the FF and FS configurations. The polarizability for the SS configuration is only slightly reduced from the uncoupled limit to  $R \approx 8 \text{ \AA}$  by DFT and  $R \approx 6 \text{ \AA}$  by the analytical model. Thus, the Raman intensity is expected to decrease as well. At close distances, the SS configuration begins to increase its polarizability, implying that the Raman intensity may increase for this orientation.

More accurately, the Raman intensity of a given normal mode is proportional to the derivative of polarizability with respect to the mode. For two interacting polarizable bodies, the Raman intensity can be represented as:

$$I \propto \left| \frac{\partial \alpha}{\partial Q_1} \right|^2 + \left| \frac{\partial \alpha}{\partial Q_2} \right|^2, \quad (3)$$

where  $Q_1$  and  $Q_2$  are the normal modes for the first and second azobenzene molecules, respectively. If eqs. (1) and (2) are the polarizability function for eq. (3), we derive the follow expressions for the Raman intensity:

$$I_{\parallel} \propto \left| \frac{\partial \alpha_1}{\partial Q_1} \right|^2 \left( \frac{1 + \frac{2\alpha_2}{R^3}}{1 - \frac{4\alpha_1\alpha_2}{R^6}} \right)^4 + \left| \frac{\partial \alpha_2}{\partial Q_2} \right|^2 \left( \frac{1 + \frac{2\alpha_1}{R^3}}{1 - \frac{4\alpha_1\alpha_2}{R^6}} \right)^4 \quad (4)$$

and

$$I_{\perp} \propto \left| \frac{\partial \alpha_1}{\partial Q_1} \right|^2 \left( \frac{1 - \frac{\alpha_2}{R^3}}{1 - \frac{\alpha_1\alpha_2}{R^6}} \right)^4 + \left| \frac{\partial \alpha_2}{\partial Q_2} \right|^2 \left( \frac{1 - \frac{\alpha_1}{R^3}}{1 - \frac{\alpha_1\alpha_2}{R^6}} \right)^4, \quad (5)$$

where  $\left| \frac{\partial \alpha_1}{\partial Q_1} \right|^2$  and  $\left| \frac{\partial \alpha_2}{\partial Q_2} \right|^2$  are the Raman intensities for the first and second isolated azobenzene molecules, respectively. The factors to the fourth power can be viewed as enhancement or de-enhancement factors to the Raman spectrum. Since the  $R^6$  terms are practically zero where the analytical model is valid, we can safely ignore this term and only consider the numerator and  $R^3$  terms. With this simplification, we find that the Raman intensity for each of the isolated molecules is affected by the other molecule's polarizability. The physical interpretation of eqs. (4) and (5) is that the local fields generated by the induced dipoles of one azobenzene molecule affect the Raman spectrum of the other molecule positively for the parallel interactions (*i.e.*, eq. (4)'s numerators are additive) and negatively for the perpendicular interactions (*i.e.*, eq. (5)'s numerators are subtractive). Since the perpendicular interactions dominate the polarizability, we expect similar effects in Raman intensities (*i.e.*, eq. (5) to dominate the trends). Thus, the total Raman spectrum is expected to decrease as the azobenezene molecules have increased dipole-dipole interactions, which is observed in both DFT and experimental data.

## 4.4 CONCLUSIONS AND FUTURE PROSPECTS

By combining a precisely controllable self-assembly strategy with high-sensitivity and high-resolution SERS and STM analytical tools, we successfully revealed the tunable dipole-dipole interactions in the precise molecular assemblies. Experimental data are well supported by calculations based on both DFT and an analytical model. While our experiments observe destructive interference in the Raman spectra, further calculations reveal that both constructive and destructive interference are possible by better control of the dipole-dipole interactions through adjusting the orientations of the excitation light and molecular assemblies. This prediction challenges our experimental capabilities in designing and controlling the precise orientations of the molecular assemblies across the substrate. This work opens new avenues with which to control intermolecular distance precisely and paves the way toward new insights into intermolecular interactions both for studying fundamental physics and for controlling molecule and device functionality.



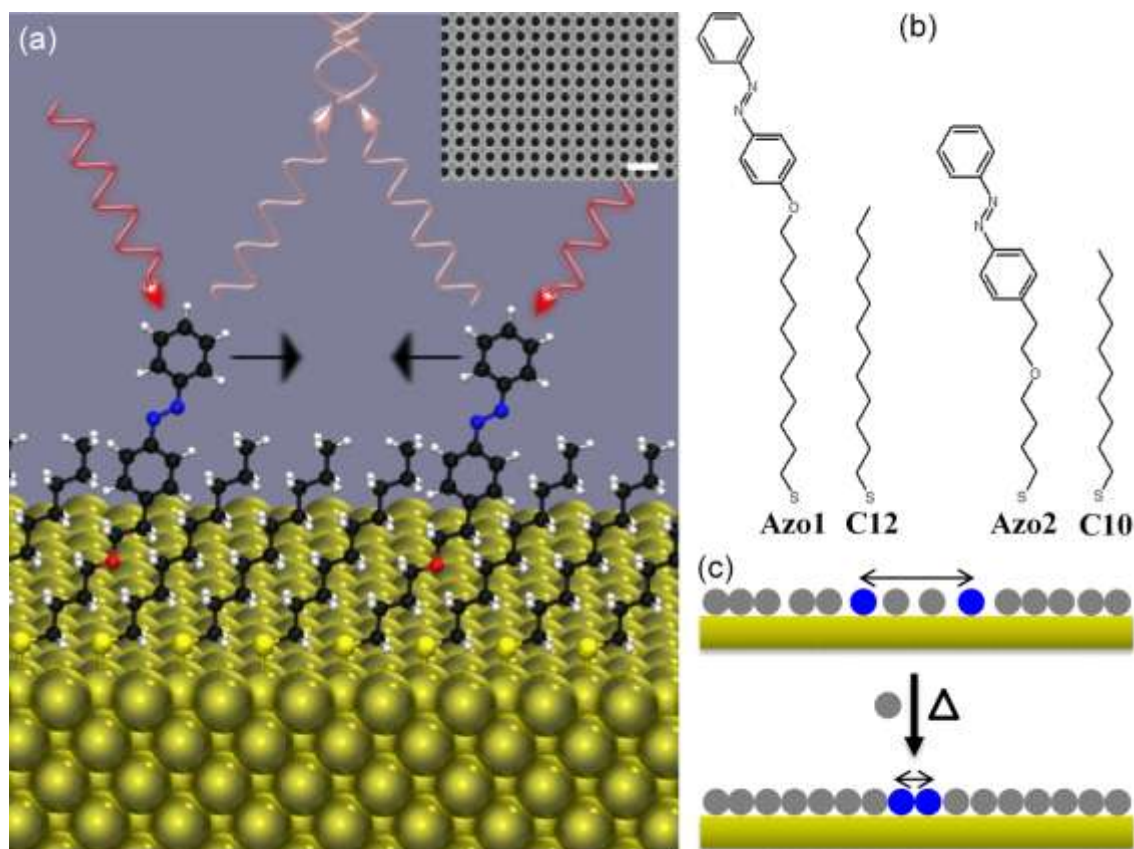


**Figure 4.1.** (a) A schematic of tethered azobenzene in self-assembled monolayer of thiolates on a Au surface, illustrating the effects of the light-induced intermolecular interactions (indicated by two black arrows) on the Raman signal. The red arrows indicate the excitation light and the purple arrows indicate the scattered light (*i.e.*, Raman signal). The inset shows a representative scanning electron micrograph of a nanohole array in a Au thin film. The scale bar in the inset is 600 nm. (b) Chemical structures of the two azobenzene-functionalized molecules studied, 4-(1-mercaptoundec-11-yloxy)-azobenzene (**Azo1**) and 4-[2-(4-phenylazo-phenyl)-ethoxy]-butane-1-thiol (**Azo2**), and the corresponding matrix molecules, dodecanethiolate (**C12**) and decanethiolate (**C10**). (c) An illustration of how the vapor-annealing method tunes the supramolecular structure of azobenzene-functionalized molecules. The gray and blue dots represent alkanethiol and azobenzene-functionalized molecules, respectively.

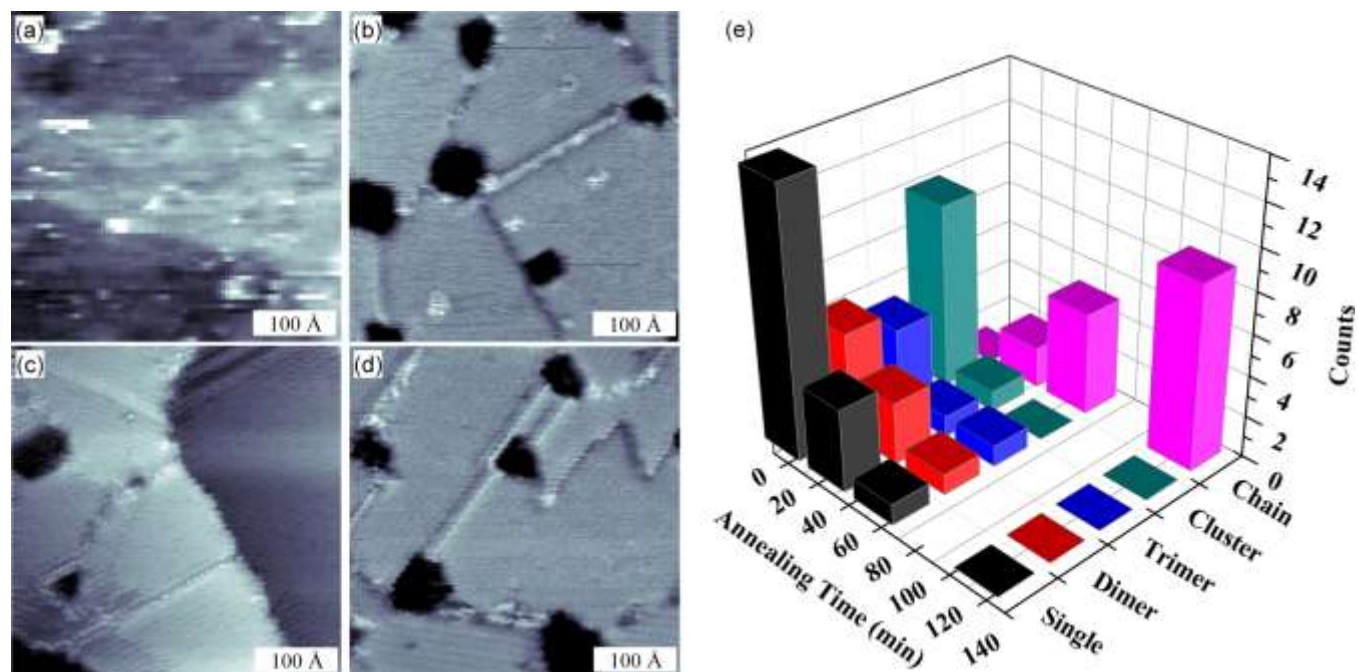


**Figure 4.2.** A series of scanning tunneling microscope images of **Azo2** in a decanethiol matrix as a function of vapor annealing time: (a) 0 min; (b) 30 min; (c) 60 min; and (d) 120 min. (e) The relative counts of each structure as a function of annealing time.

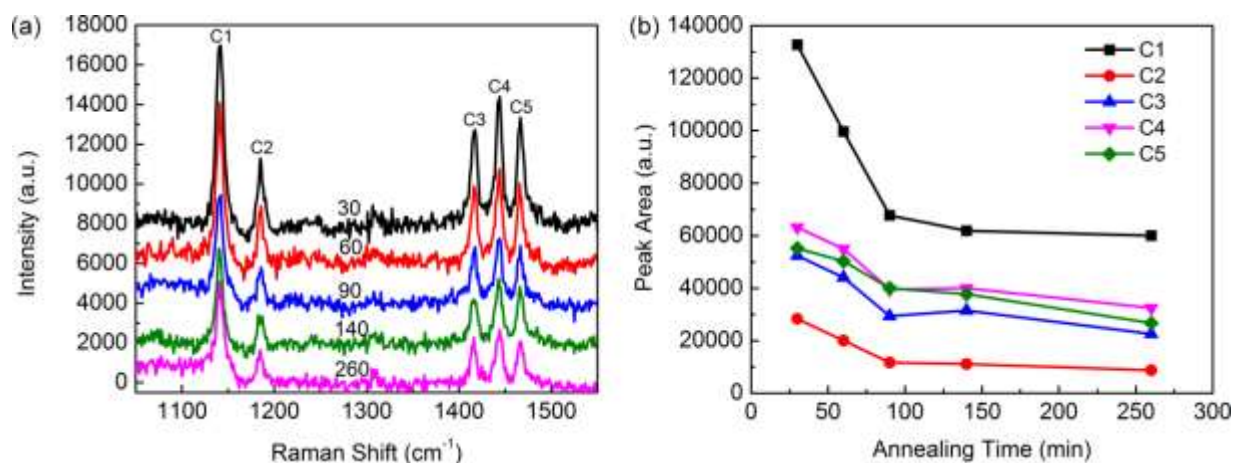


**Figure 4.3.** (a) A series of surface-enhanced Raman spectra of azobenzene-functionalized molecules (**Azo1**) as a function of annealing time. The numbers near the spectra indicate the annealing times in minutes; C1, C2, C3, C4, and C5 indicate the five modes observed. (b) Evolution of peak area intensities of the five modes as a function of annealing time.

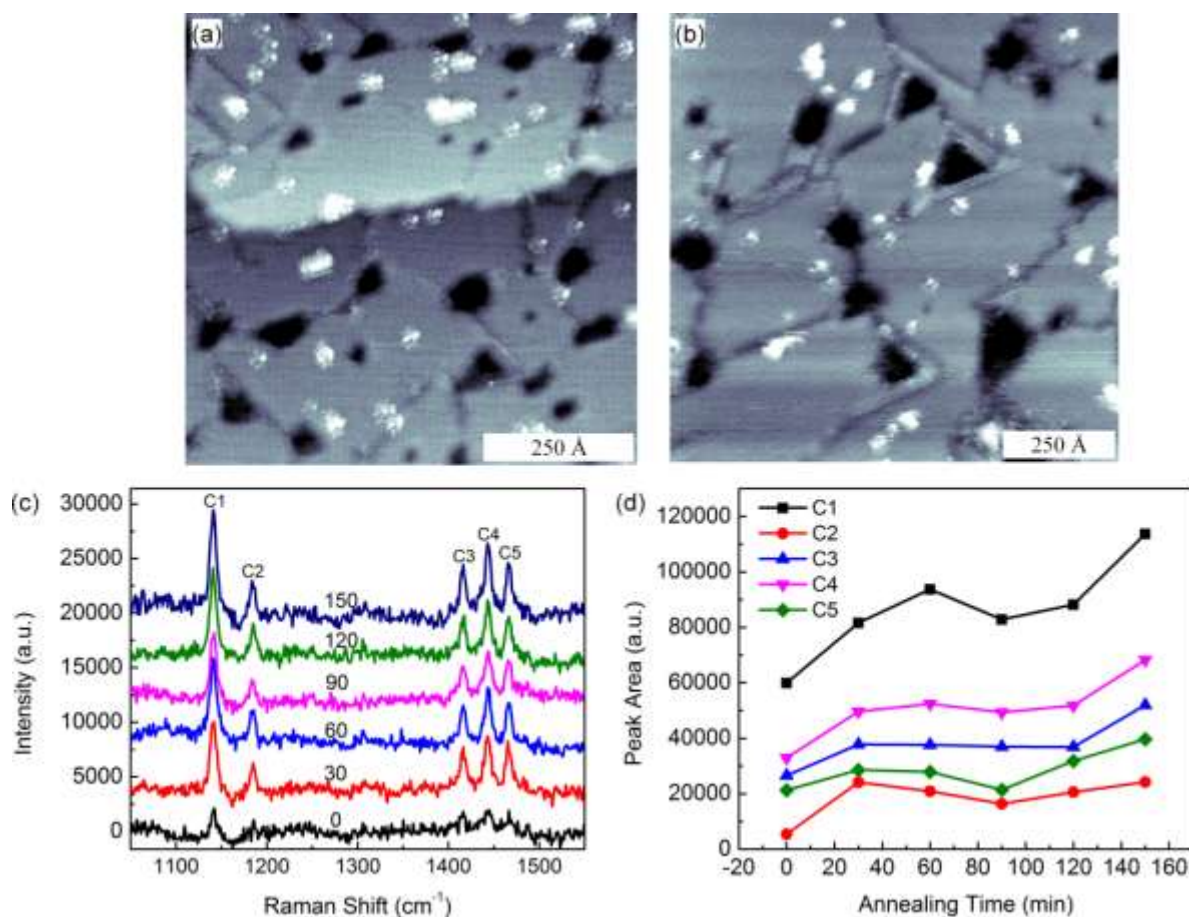


**Figure 4.4.** Control experiments with samples prepared by co-adsorption from solution. (a) Scanning tunneling microscope image of **Azo2** in a **C10** matrix without vapor annealing. (b) Scanning tunneling microscope image of **Azo2** in a **C10** matrix with vapor annealing for 120 min. (c) A series of surface-enhanced Raman spectra as a function of annealing time; the numbers near the spectra indicate the annealing time in minutes. C1, C2, C3, C4, and C5 indicate the five Raman modes observed. (d) Evolution of peak area intensities of the five modes as a function of annealing time.



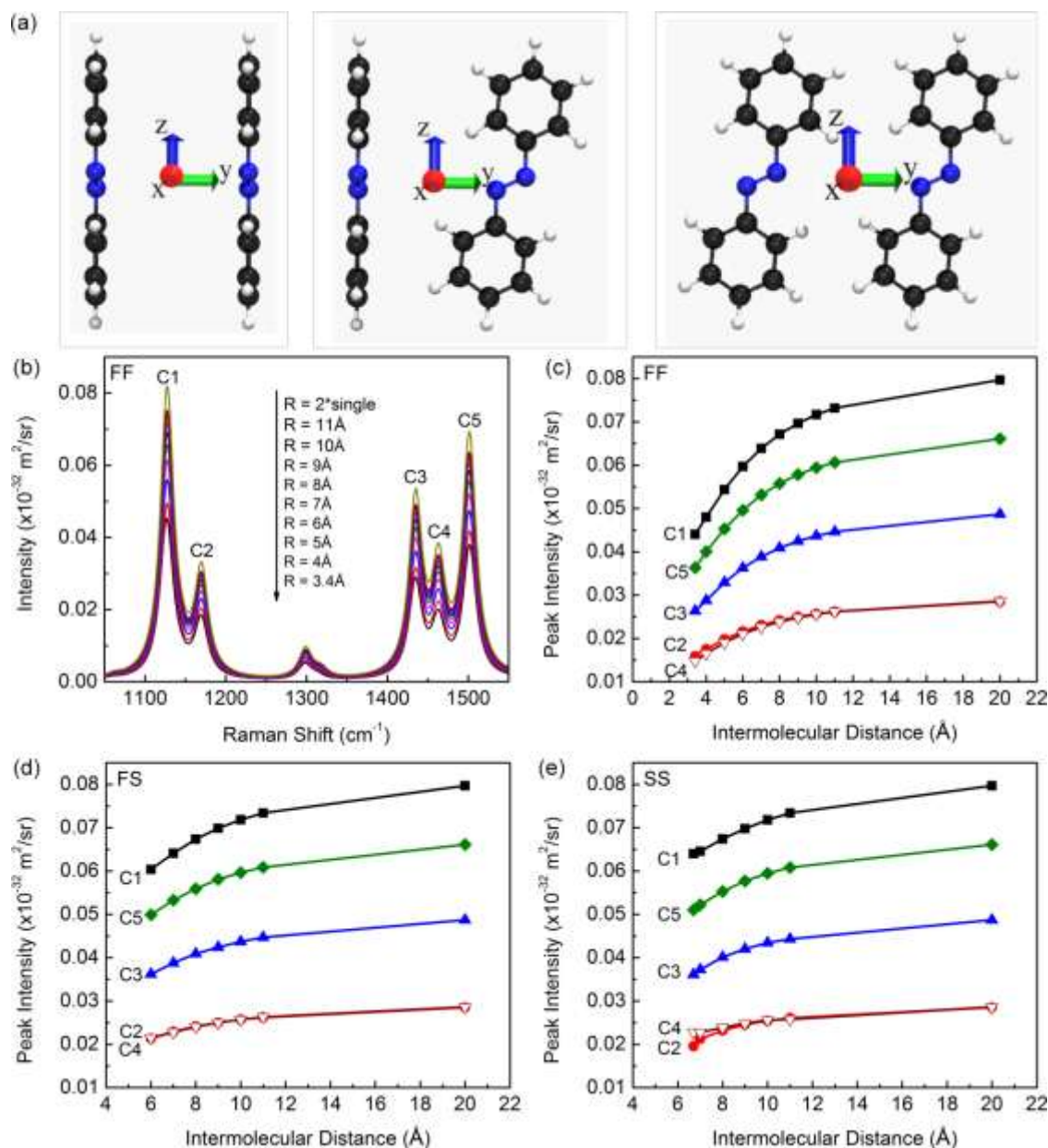


**Figure 4.5.** (a) Three basic types of configuration of the azobenzene pairs. Left: face-to-face (FF), middle: face-to-side (FS), and right: side-to-side (SS). (b) The B3LYP/6-31G\* Raman spectra of azobenzene pairs in FF configurations as a function of the intermolecular distance  $R$ . The five major modes are indicated as C1-C5. The arrow indicates the spectra from high to low intensities corresponding to the  $R$  values.  $R=2*\text{single}$  indicates the spectrum obtained by doubling the single azobenzene spectrum. (c-e) The Raman differential cross sections of modes

C1-C5 as a function of inter-azo distance for FF, FS, and SS configurations, respectively. R=2\*single is assumed to be 20 Å for a better perspective of the figures. The B3LYP/6-31G\* frequencies were scaled by 0.9614.<sup>36</sup>

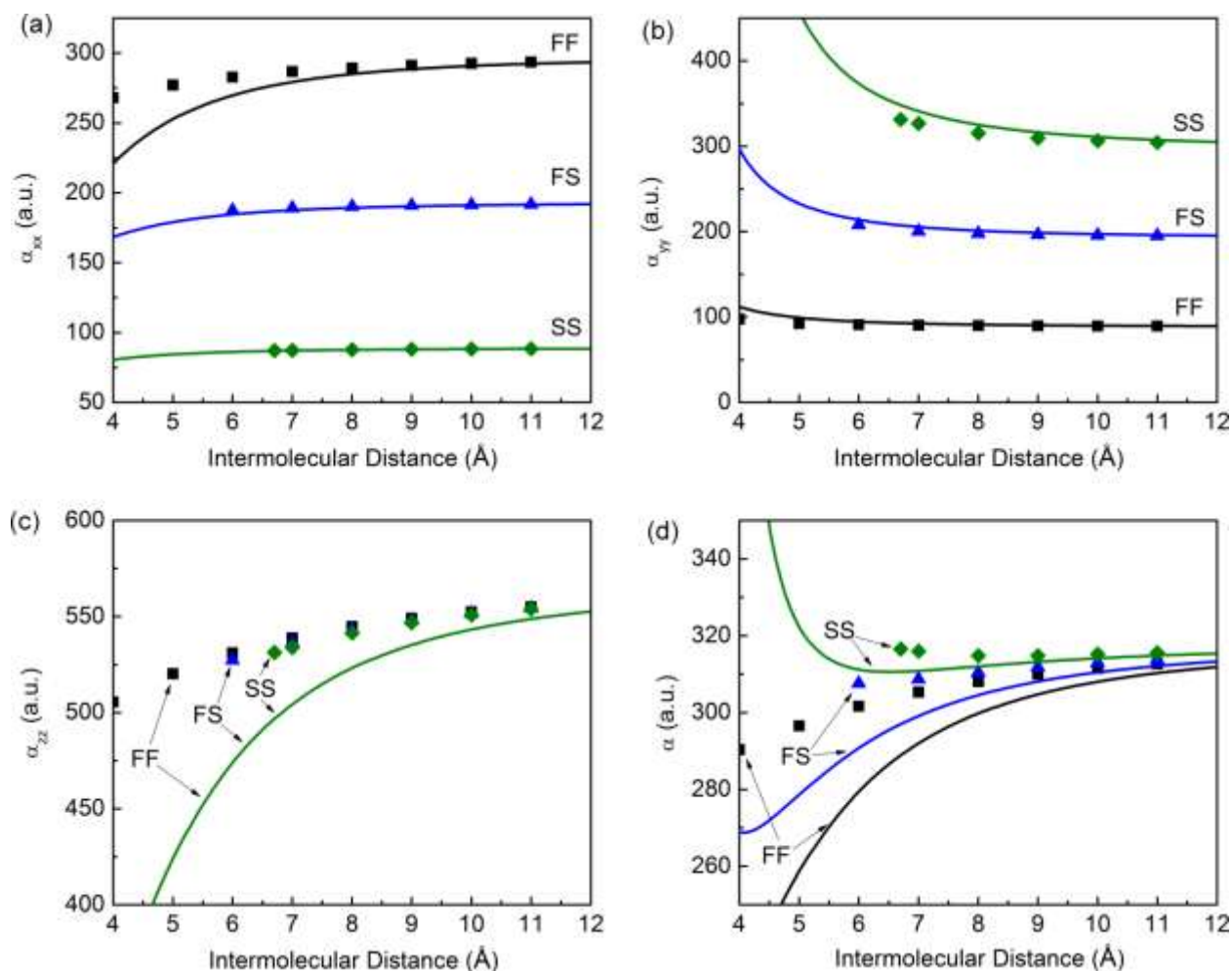


**Figure 4.6.** The polarizability of azobenzene pairs as function of intermolecular distance for the FF (black), FS (blue), and SS (olive) configurations where (a), (b), and (c) are the  $xx$ ,  $yy$ , and  $zz$  diagonal components of polarizability tensor, respectively, and (d) is the total isotropic polarizability. The solid curves are the polarizabilities calculated by the analytical model, while the points are the B3LYP/6-31G\* polarizabilities. As shown in Fig. 4.5a, the  $y$ -axis is the parallel axis while the  $x$ - and  $z$ -axes are the perpendicular axes.

## 4.5 REFERENCES

1. Balzani, V.; Credi, A.; Venturi, M., *Molecular Devices and Machines: Concepts and Perspectives for the NanoWorld*. Wiley-VCH: Weinheim, 2008.
2. Klajn, R. *Pure Appl. Chem.* **2010**, 82, 2247-2279.
3. Ciesielski, A.; Samori, P. *Nanoscale* **2011**, 3, 1397-1410.
4. Davis, J. J.; Orlowski, G. A.; Rahman, H.; Beer, P. D. *Chem. Commun.* **2010**, 46, 54-63.
5. Browne, W. R.; Feringa, B. L. *Annu. Rev. Phys. Chem.* **2009**, 60, 407-428.
6. Weiss, P. S. *Nature* **2011**, 479, 187-188.
7. Weiss, P. S. *Acc. Chem. Res.* **2008**, 41, 1772-1781.
8. Berna, J.; Leigh, D. A.; Lubomska, M.; Mendoza, S. M.; Perez, E. M.; Rudolf, P.; Teobaldi, G.; Zerbetto, F. *Nature Mater.* **2005**, 4, 704-710.
9. Ariga, K.; Mori, T.; Hill, J. P. *Soft Matter* **2012**, 8, 15-20.
10. Barth, J. V. *Annu. Rev. Phys. Chem.* **2007**, 58, 375-407.
11. Juluri, B. K.; Kumar, A. S.; Liu, Y.; Ye, T.; Yang, Y. W.; Flood, A. H.; Fang, L.; Stoddart, J. F.; Weiss, P. S.; Huang, T. J. *ACS Nano* **2009**, 3, 291-300.
12. Song, H.; Lee, H.; Lee, T. *J. Am. Chem. Soc.* **2007**, 129, 3806-3807.
13. Reuter, M. G.; Solomon, G. C.; Hansen, T.; Seideman, T.; Ratner, M. A. *J. Phys. Chem. Lett.* **2011**, 2, 1667-1671.



14. Reuter, M. G.; Seideman, T.; Ratner, M. A. *Nano Lett.* **2011**, *11*, 4693-4696.
15. Milani, A.; Brambilla, L.; Del Zoppo, M.; Zerbi, G. *J. Phys. Chem. B* **2007**, *111*, 1271-1276.
16. Milani, A.; Del Zoppo, M.; Tommasini, M.; Zerbi, G. *J. Phys. Chem. B* **2008**, *112*, 1619-1625.
17. Li, D. B.; Paxton, W. F.; Baughman, R. H.; Huang, T. J.; Stoddart, J. F.; Weiss, P. S. *MRS Bull.* **2009**, *34*, 671-681.
18. Jensen, S. C.; Baber, A. E.; Tierney, H. L.; H. Sykes, E. C. *ACS Nano* **2007**, *1*, 423-428.
19. Bombis, C.; Weigelt, S.; Knudsen, M. M.; Nørgaard, M.; Busse, C.; Lægsgaard, E.; Besenbacher, F.; Gothelf, K. V.; Linderroth, T. R. *ACS Nano* **2009**, *4*, 297-311.
20. Ciesielski, A.; Palma, C. A.; Bonini, M.; Samori, P. *Adv. Mater.* **2010**, *22*, 3506-3520.
21. Klajn, R.; Bishop, K. J. M.; Grzybowski, B. A. *Proc. Natl. Acad. Sci.* **2007**, *104*, 10305-10309.
22. Gahl, C.; Schmidt, R.; Brete, D.; McNellis, E. R.; Freyer, W.; Carley, R.; Reuter, K.; Weinelt, M. *J. Am. Chem. Soc.* **2010**, *132*, 1831-1838.
23. Pathem, B. K., Kumar, A. S., Cao, Y., Zheng, Y. B., Corley, D. A., Ye, T., Aiello, V. J., Crespi, V. H., Houk, K. N., Tour, J. M., Weiss, P. S. *In preparation*.
24. Kumar, A. S.; Ye, T.; Takami, T.; Yu, B.-C.; Flatt, A. K.; Tour, J. M.; Weiss, P. S. *Nano Lett.* **2008**, *8*, 1644-1648.

25. Witlicki, E. H.; Johnsen, C.; Hansen, S. W.; Silverstein, D. W.; Bottomley, V. J.; Jeppesen, J. O.; Wong, E. W.; Jensen, L.; Flood, A. H. *J. Am. Chem. Soc.* **2011**, *133*, 7288-7291.
26. Witlicki, E. H.; Andersen, S. S.; Hansen, S. W.; Jeppesen, J. O.; Wong, E. W.; Jensen, L.; Flood, A. H. *J. Am. Chem. Soc.* **2010**, *132*, 6099-6107.
27. Heyns, J. B.; Sears, L. M.; Corcoran, R. C.; Carron, K. T. *Anal. Chem.* **1994**, *66*, 1572-1574.
28. Hill, W.; Wehling, B.; Gibbs, C. G.; Gutsche, C. D.; Klockow, D. *Anal. Chem.* **1995**, *67*, 3187-3192.
29. McNally, A.; Forster, R. J.; Keyes, T. E. *Phys. Chem. Chem. Phys.* **2009**, *11*, 848-856.
30. Wei, A.; Kim, B.; Sadtler, B.; Tripp, S. L. *ChemPhysChem* **2001**, *2*, 743-745.
31. Zheng, Y. B.; Payton, J. L.; Chung, C. H.; Liu, R.; Cheunkar, S.; Pathem, B. K.; Yang, Y.; Jensen, L.; Weiss, P. S. *Nano Lett* **2011**, *11*, 3447-52.
32. Zheng, Y. B.; Pathem, B. K.; Hohman, J. N.; Thomas, J. C.; Kim, M.; Weiss, P. S. *Adv. Mater.* **2012**, *24*, in press. DOI: 10.1002/adma.201201532.
33. Donhauser, Z. J.; Price, D. W.; Tour, J. M.; Weiss, P. S. *J. Am. Chem. Soc.* **2003**, *125*, 11462-11463.
34. Valiev, M.; Bylaska, E. J.; Govind, N.; Kowalski, K.; Straatsma, T. P.; Van Dam, H. J. J.; Wang, D.; Nieplocha, J.; Apra, E.; Windus, T. L.; de Jong, W. *Comput. Phys. Commun.* **2010**, *181*, 1477-1489.
35. Becke, A. D. *J. Chem. Phys.* **1993**, *98*, 5648-5652.

36. Merrick, J. P.; Moran, D.; Radom, L. *J. Phys. Chem. A* **2007**, *111*, 11683-11700.
37. Saavedra, H. M.; Mullen, T. J.; Zhang, P. P.; Dewey, D. C.; Claridge, S. A.; Weiss, P. S. *Rep. Prog. Phys.* **2010**, *73*.
38. Smith, R. K.; Lewis, P. A.; Weiss, P. S. *Prog. Surf. Sci.* **2004**, *75*, 1-68.
39. Kho, K. W.; Shen, Z. X.; Lei, Z.; Watt, F.; Soo, K. C.; Olivo, M. *Anal. Chem.* **2007**, *79*, 8870-8882.
40. Silberstein, L. *Philos. Mag.* **1917**, *33*, 521-533.
41. Jensen, L.; Astrand, P.-O.; Osted, A.; Kongsted, J.; Mikkelsen, K. V. *J. Chem. Phys.* **2002**, *116*, 4001-4010.

## **CHAPTER 5**

### ***EFFECT OF TETHER CONDUCTIVITY ON THE EFFICIENCY OF PHOTOISOMERIZATION OF AZOBENZENE-FUNCTIONALIZED MOLECULES ON Au{111}***

## 5.1 INTRODUCTION

Precise control over the reversible isomerization of functional molecules when assembled on solid surfaces is of great importance in order to understand the rules of molecular and supramolecular-scale action.<sup>1-14</sup> Various kinds of photochromic molecules such as azobenzene,<sup>15-24</sup> diarylethene,<sup>9,25-27</sup> spiropyran,<sup>28,29</sup> and more recently dihydroazulene<sup>30-33</sup> have been investigated as possible candidates for molecular switches. These families of functional molecules have relative advantages and disadvantages due to factors such as their ease of molecular assembly on substrates, quantum yield of photoisomerization, reversibility of isomerization, and quenching of isomerization by the underlying substrate. Of these families of photochromic molecules, azobenzenes have thus far attracted the greatest attention.

Azobenzene (henceforth **Azo**) exists in a near-planar *trans* conformation in its thermodynamically stable state with nearly zero dipole moment.<sup>34,35</sup> When irradiated with UV light at ~365 nm, the molecule isomerizes to a non-planar *cis* conformation via rotation of a phenyl group out of the plane of the azobenzene moiety, carrying a dipole moment of 3 D.<sup>35</sup> Upon subsequent irradiation with ~420 nm visible light, the *cis* conformation reverts back to its original *trans* conformation, although thermal relaxation from *cis* to *trans* has also been shown to be a common pathway for the reverse reaction where relaxation times typically depend upon the substituents on the azobenzene moiety ranging from minutes (for alkyl-substituted molecules) to days (for unsubstituted azobenzenes). Due to their difference in planarity, it has been established that *trans* form is approximately 100 times more conductive than *cis*<sup>16</sup> and hence, azobenzenes are considered to be a type of molecular switches.<sup>22</sup> Various theoretical and experimental studies have been performed to understand the mechanisms of photoisomerization of azobenzenes in the gas phase, in various solvents, and on solid substrates when isolated as single molecules or in

ensembles. For instance, it has been well established that photoisomerization of molecules such as azobenzenes is quenched when the molecules are adsorbed directly on conductive substrates such as Au{111}.<sup>20</sup> However, by attaching a relatively non-conductive tether to the azobenzene functional moiety, that the molecules can be spatially separated from the substrate, and a dramatic increase in the photoisomerization yield has been observed both at ensemble<sup>36</sup> and single-molecule scales.<sup>22,37-39</sup> Recently, SERS has been shown to be an excellent tool for following photoisomerization of functional molecules at the ensemble scale.<sup>14,36,40</sup>

Although, the effects of the surrounding environment,<sup>41,42</sup> the coupling of the functional moiety to the substrate using a tether,<sup>12,18,20-22,43,44</sup> the conductivity of the substrate,<sup>21,38,45</sup> the length and free volume of the tether,<sup>46,47</sup> the structure of the substrate,<sup>36,47-49</sup> and ways to circumvent steric interactions between the azobenzene moieties<sup>22,23,50,51</sup> have been reported previously, the effects of the conductivity of the tethers on photoisomerization have not been reported. In order to employ such molecular switches in a range of conditions and chemical environments, it is imperative to understand the roles of all the key aspects constituting the photoswitches and their supporting structures. To that end, we investigate the role of the conductivity of the tether on the photoisomerization of azobenzene molecules when assembled on Au{111}.

We designed tethers to functionalize azobenzene molecules so that they could be covalently bound to Au substrates and such that the functional moiety is spatially separated from the conductive substrate in order to avoid direct surface quenching. We assembled these functional molecules as isolated single molecules by a co-adsorption technique that we have reported previously.<sup>22</sup> This technique enables us to separate azobenzene-functionalized molecules from each other such that steric hindrance between neighboring molecules is

precluded. We employed azobenzene functionalized with two kinds of tethers in this study- a non-conductive, saturated linear alkyl chain tether (henceforth **Azo1**) and a more conductive tether (henceforth **Azo2**) (Fig. 5.1). We used SERS to follow the time course of photoisomerization of these azobenzene-functionalized molecules on Au{111} in sufficient numbers to have significant statistics.<sup>36,42,52-54</sup>

The phenylene ethynylene tether in **Azo2** is expected to be substantially more conductive than the alkyl tether in **Azo1**. If the conductance of a molecule is given by  $G=Ae^{-(\beta n)}$  (where A is constant, n is the length of the molecule), the term  $\beta$  is a measure of molecular conductivity vs. length. A number of studies have found that for saturated chains on Au  $\beta \approx 1.0 \pm 0.1 \text{ \AA}^{-1}$ ,<sup>55-63</sup> whereas for phenylene ethynylenes, with mixed sp and sp<sup>2</sup> hybridization, it is approximately a factor of two lower and  $\beta \approx 0.57 \pm 0.02 \text{ \AA}^{-1}$ .<sup>64,65</sup> Note that phenylene vinylene and other all sp<sup>2</sup> hybridized systems have  $\beta$  values another factor of two lower,<sup>66</sup> and thus are more conductive (and would be expected to quench even faster than the tether in **Azo2**).

We have previously reported an efficient way to follow the photoisomerization using SERS.<sup>36,54,67</sup> Using this method, Au substrates with regular nanohole arrays were shown to enhance the signals of azobenzene Raman vibrational modes. Here, we employed the same technique to follow the time course measurements of both **Azo1** and **Azo2** molecules.

## 5.2 METHODS

Focused ion beam (FIB) lithography (Nova 600 NanoLab, FEI Company, Hillsboro, OR, USA) was used to fabricate cylindrical nanoholes (with a diameter of 175 nm) in square arrays (with a period of 300 nm) into Au thin films. The samples were prepared in the dark by immersing the flame-annealed Au{111} nanohole array substrates in a 1:4 mixture of ethanolic

solutions of **Azo1** or **Azo2** and decanethiol (**C10**) (such that the final concentration of the solutions was 1 mM), for 24 h under nitrogen atmosphere. The samples were then vapor annealed over **C10** solutions at 80 °C for 2 h in order to backfill the **C10** matrix molecules.<sup>68</sup> This process, in which the substrate is heated and held over a neat liquid of **C10** molecules to be ordered, resulted in tight packing of the monolayer, thus hindering the surface mobility of the switch molecules.<sup>42,56,69,70</sup> The samples were then stored in the dark until further analysis.

A Renishaw inVia Raman system (Renishaw Inc., Illinois, USA) operating under ambient conditions was employed for Raman analysis. We chose a 632.8 nm He-Ne laser as the Raman excitation source considering the resonant wavelength of the Au substrates. Laser power and beam diameter were ~17 mW and ~1  $\mu$ m, respectively. Each measurement was a convolution of 50 sweeps in the wavelength range of interest with a set integration time of 150 s. Wire 3.2 (Renishaw Inc., Illinois, USA) and OriginPro software were used to analyze peak areas and to curve fit and to calculate decay constants, respectively.

In order to compare the experimental results with theory, simulations were performed to predict the Raman spectra of the *trans* and *cis* isomers of **Azo2** molecules attached to a Au<sub>3</sub> cluster. All calculation used the NWCHEM software package.<sup>71</sup> The B3LYP hybrid functional with the 6-31G\* basis set for N, C, S, and H atoms and the LANL2DZ effective core potential for Au atoms were employed for all calculations of the geometric structure and vibrational frequencies. Vibrational frequencies were scaled by 0.9614; no imaginary frequencies were found. The Raman differential cross sections were calculated with a three-point numerical differentiation of the analytical polarizabilities with LC- $\omega$ PBE functional ( $\omega=0.3$  Bohr<sup>-1</sup>,  $\alpha=0.0$ , and  $\beta=1.0$ ) and the same basis set. The Raman differential cross sections were broadened with a Lorentzian having a full-width-at-half-maximum of 20 cm<sup>-1</sup> and an incident light of 514.5 nm.



Raman signals for different mole fractions of the molecules were also calculated to gain a better understanding of the switching efficiencies of molecules on the substrate. The analogous calculations for **Azo1** (without the Au cluster) have been reported previously<sup>36</sup> and are used here in elucidating the role of the tether.

### 5.3 RESULTS AND DISCUSSIONS

Figure 5.2 shows the overlay of simulated Raman spectra of **Azo2** molecules attached to Au<sub>3</sub> clusters as a convolution of various mole fractions of *trans* and *cis* isomers. The spectra have been offset for clarity. Multiple peaks in the range of 1000 to 1700 cm<sup>-1</sup> were observed with major peaks at 1055, 1116, 1435, 1458, 1495, and 1573 cm<sup>-1</sup> (see Fig. 5.3 for schematics of all these modes in *trans* and *cis* conformations). After considering all the peaks in the simulated spectra, the peaks labeled P1 (1055 cm<sup>-1</sup>) and P2 (1116 cm<sup>-1</sup>) were identified as strong indicators of photoisomerization. Also, the area of peak at 1540 cm<sup>-1</sup> was observed to increase with *trans-cis* isomerization. This peak arises due to the vibration mode of the N=N double bond (Fig. 5.3) and is not prominent when the molecules are in the *trans* conformation; only when the molecule isomerizes, does this vibrational mode become Raman active. Although we identified this peak in our experiments, the peak area was usually at or below the detection limit; thus, it was not used for quantitative measurements. Whereas all the other peaks decrease in area, the areas of peaks at 1055 cm<sup>-1</sup> (P1) and 1573 cm<sup>-1</sup> show very little change.

The Raman intensity usually scales with the polarizability of a system (because the Raman intensity derives from the polarizability derivatives  $(\partial\alpha/\partial Q)^2$ ). Since the *trans* isomer (highly conjugated) is more polarizable, it is expected to have a stronger Raman signals than the less polarizable *cis* isomer (less conjugated), as observed in Figs. 5.2 and 5.5. To explain the

behavior of the P1 mode, we observe that the mode is mainly isolated to the tether ring, while P2 is mainly a ring breathing mode of the azobenzene unit (Fig. 5.4). The *trans* to *cis* isomerization reduces the conjugation and thus the polarizability of the azobenzene unit, but not that of the tether, at least not directly. Thus, it is not surprising to find that the P1 mode (that is isolated to the tether) is minimally affected by isomerization while P2 (an azobenzene mode) is significantly affected. Figure 5.4 shows the schematic of the vibrational modes of **Azo2** that contribute to the intensity of these peaks in the spectra.

We identified and used peaks P1 and P2 for quantification, due to their strong signals and relative sensitivity to isomerization. We followed the changes in these peak areas as a function of UV illumination time. As can be seen in Fig. 5.5, the peak area of P1 remains relatively unchanged, whereas, the peak area of P2 decreases with the duration of UV illumination. The simulated spectra and the experimental results are in close agreement. We chose P1 as an internal standard (due to the minimal effect on its peak area upon photoisomerization) and by comparing the rate of change of the peak area of P2 with respect to P1 a direct measurement of the photoisomerization kinetics of **Azo2** was achieved. We measure the ratio of peak areas of P1 to P2 and plot the change in the ratio as a function of UV illumination.

We measured the peak areas of P1 and P2 from the baseline-subtracted spectra for each data point from 0 to 90 min UV light exposure ( $\sim 365$  nm and power of  $\sim 1$  mW/cm<sup>2</sup>). We then plotted the ratios of peak areas of P1 to P2 versus the duration of UV light exposure. An exponential decay curve was derived by using the formula  $Y = Y_0 + Ae^{(R_0x)}$ , where  $R_0$  is the decay constant of the best fit curve, with units as time<sup>-1</sup>. The inverse of the calculated decay constant gave us the time constant  $\tau$ . We calculated the time constants for both molecules using the same procedure. Figure 5.6a shows the change in the ratio of peaks P1 to P2 as a function of

UV light illumination for the molecule **Azo2**. The plot was generated by taking the average of three data sets (peak area ratios of P1:P2) measured under identical conditions. Figure 5.6b shows the plot generated from simulated spectra. We have reported the decay plot for **Azo1** previously,<sup>67</sup> wherein we used the peak area ratios of vibrational modes, which were in agreement with the simulated spectra for **Azo1**. The time constant derived from the exponential decay curve of **Azo2** in Fig. 5.6a, was found to be  $\tau = 61 \pm 11$  min. The time constant from our previous study with **Azo1** was found to be  $\tau = 38 \pm 13$  min.<sup>67</sup>

The reverse isomerization of **Azo2** from *cis* to *trans* was also investigated by irradiating the sample with blue light (~450 nm and power of 6 mW/cm<sup>2</sup>). Whereas **Azo1** showed ~90% reversibility in isomerization within 100 minutes of visible light illumination,<sup>67</sup> **Azo2** did not exhibit complete reversibility, at least after 24 h of visible light illumination. Figure 5.7 shows a series of SERS spectra of the surface assembled with **Azo2** under constant visible light irradiation (spectra have been offset for clarity). Complete reversal in the peak area ratios was not observed after several hours of the time course study. The samples were then left under visible light illumination overnight and spectra were collected after 24 h. It can be seen that the peak areas of P1 and P2 increase dramatically and the ratio of the peak areas approached the initial ratio before UV illumination. The time constant derived from the experimental curve was found to be  $286 \pm 37$  min (Fig. 5.7) as opposed to the faster *cis* to *trans* photoisomerization of **Azo1**, which had a time constant of  $75 \pm 27$  min.<sup>67</sup>

Due to the increased conductivity in **Azo2**, the lifetime of the photoexcited state is lower than in the case of nonconductive tether, resulting in decreased numbers of molecules that undergo photoisomerization over a period of time, resulting in significant difference in the time constants. The experimental studies for both the molecules were performed under identical

conditions, *i.e.*, sample preparation, concentration of switch molecules, the nanohole array periodicity of the substrate, power of UV and visible light sources, and power and beam diameter of the Raman laser source. The only difference was the identity of the tether between the azobenzene functional group and the Au{111} substrate. Due to  $\sim 30^\circ$  tilt with respect to the surface normal, **Azo1** molecules align themselves in registry with the **C10** molecular tilt, whereas, it has previously been shown that molecules with tethers similar to **Azo2** assemble nominally perpendicular to the underlying Au{111} substrate,<sup>72</sup> we observed similar structures when **Azo2** was assembled on Au{111} (Fig. 5.8). Thus, even though the lengths of the tethers in **Azo1** and **Azo2** are different, after the assembly on Au{111}, the distances separating the azobenzene moieties in both the molecules from the underlying substrates are nearly the same. Since all the parameters are left constant other than the identity of the tether, the difference in the time constants can be directly correlated to the change in the conductivity of the tethers. We calculated the photoisomerization cross section of surface-bound **Azo1** and **Azo2** molecules by using the formula  $\sigma = hc/(\lambda\tau I_0)$ , where  $h$  is Planck's constant,  $c$  the speed of light,  $\lambda$  the wavelength of irradiation (365 nm),  $\tau$  the time constant, and  $I_0$  the power of the UV light source ( $570 \mu\text{W}/\text{cm}^2$ ). By holding all the experimental parameters constant we calculate and compare the surface-bound photoisomerization cross section of **Azo1** to be  $\sigma_1 = 4.5 (\pm 1.5) \times 10^{-19} \text{ cm}^2$  and of **Azo2** to be  $\sigma_2 = 2.5 (\pm 0.5) \times 10^{-19} \text{ cm}^2$ . These figures of merit indicate an order of magnitude reduction in cross section of surface-bound molecules when compared with the values in solution.<sup>51</sup> Moreover, the *cis-trans* isomerization cross section of nonconductive-tethered molecules is an order of magnitude larger than that of conductive-tethered molecules indicating the direct effect of tether conductivity on the photoisomerization of surface-bound molecules. Since it is critical to be able to tune the functionality of surface-bound molecular switches in

order to build efficient functional devices, this observation indicates a means to gain that ability by tuning the metal-molecule junction properties and to tailor the efficiency of photoisomerization.

## **5.4. CONCLUSIONS**

We have designed a new conductive tether and demonstrated its effect on the efficiency of photoisomerization of azobenzenes when assembled in precisely controlled nanoscale environments. We have employed SERS to monitor the photoisomerization kinetics of isolated single molecules in well-defined nanoscale environments. By directly comparing the time constants of non-conductive and conductive tethers, we have demonstrated that even when the azobenzene functional moiety is well separated from the substrate, the efficiency of photoisomerization decreases with increasing conductivity of the tether. This study helps elucidate how to tune the photoswitching efficiency of photochromic molecules for assembly and incorporation into nanoscale assemblies for actuation at the nanoscale.<sup>11</sup>

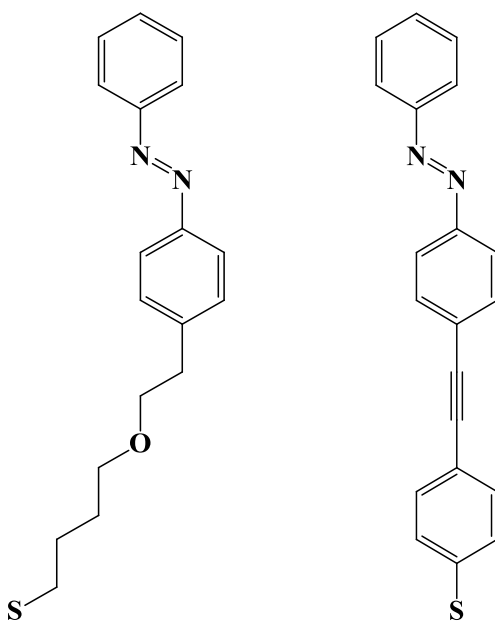


**Figure 5.1.** Schematic of (left) **Azo1** and (right) **Azo2**. Due to the linear alkyl chain **Azo1** assumes  $\sim 30^\circ$  tilt with respect to surface normal, whereas **Azo2** assumes a nominally perpendicular orientation with respect to the  $\text{Au}\{111\}$  surface (see Fig. 5.8).

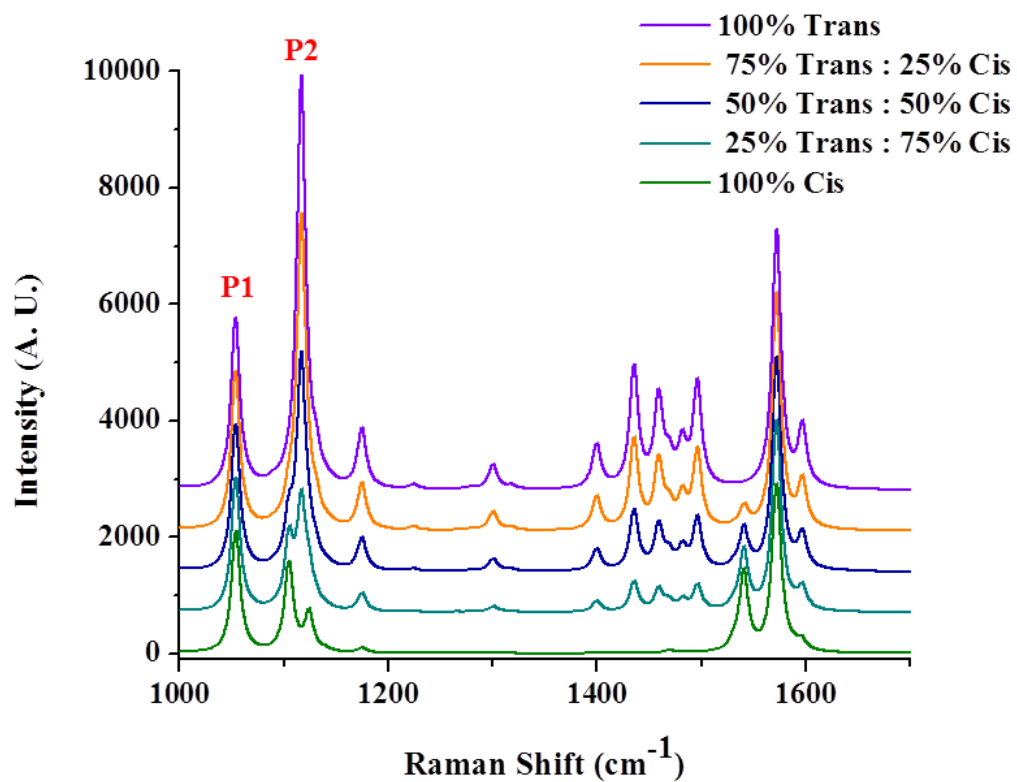


**Figure 5.2.** A) Simulated Raman spectra of *trans* and *cis* **Azo2** at various mole fractions as shown in the legend; The peaks labeled P1 and P2 were used to follow the kinetics of photoisomerization.

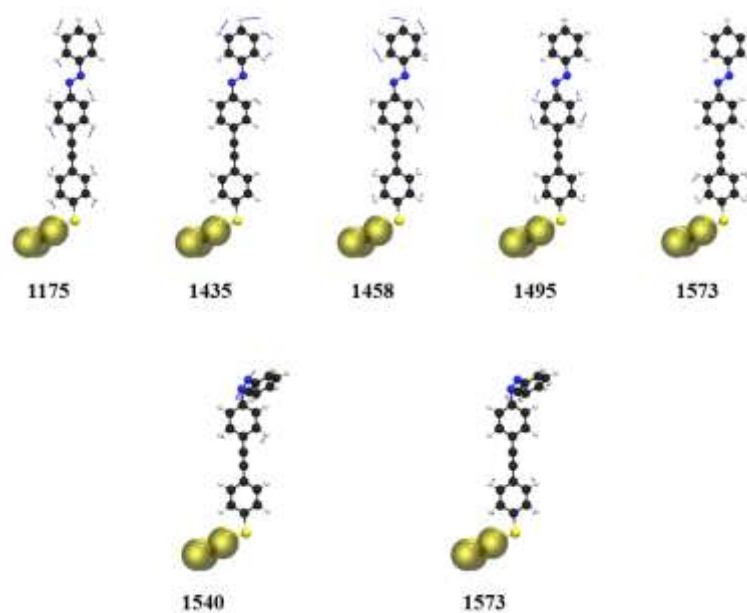


**Figure 5.3.** Calculated vibrational modes of all the prominent peaks of **Azo2** attached to a  $\text{Au}_3$  cluster observed in theoretical calculations in their *trans* and *cis* conformations, respectively.



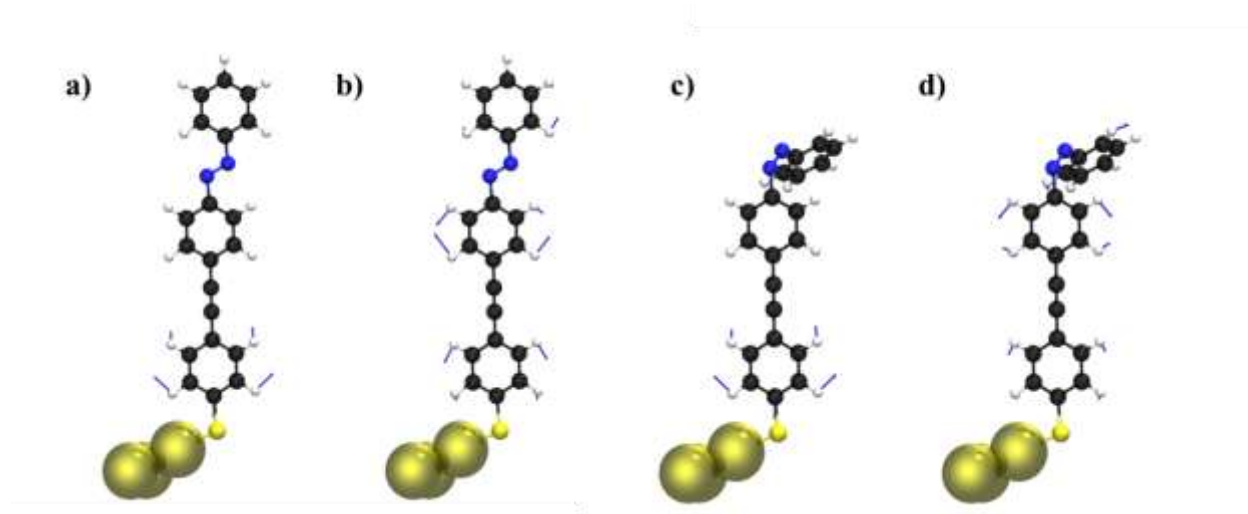


**Figure 5.4.** Schematics of the calculated vibrational modes of **Azo2** attached to a  $\text{Au}_3$  cluster in a) P1 *trans*, b) P2 *trans*, c) P1 *cis*, and d) P2 *cis* geometries. The contributions to Raman peaks P1 and P2 are due to the tether and the benzene rings (predominantly, the lower ring) of the azobenzene moiety, respectively.

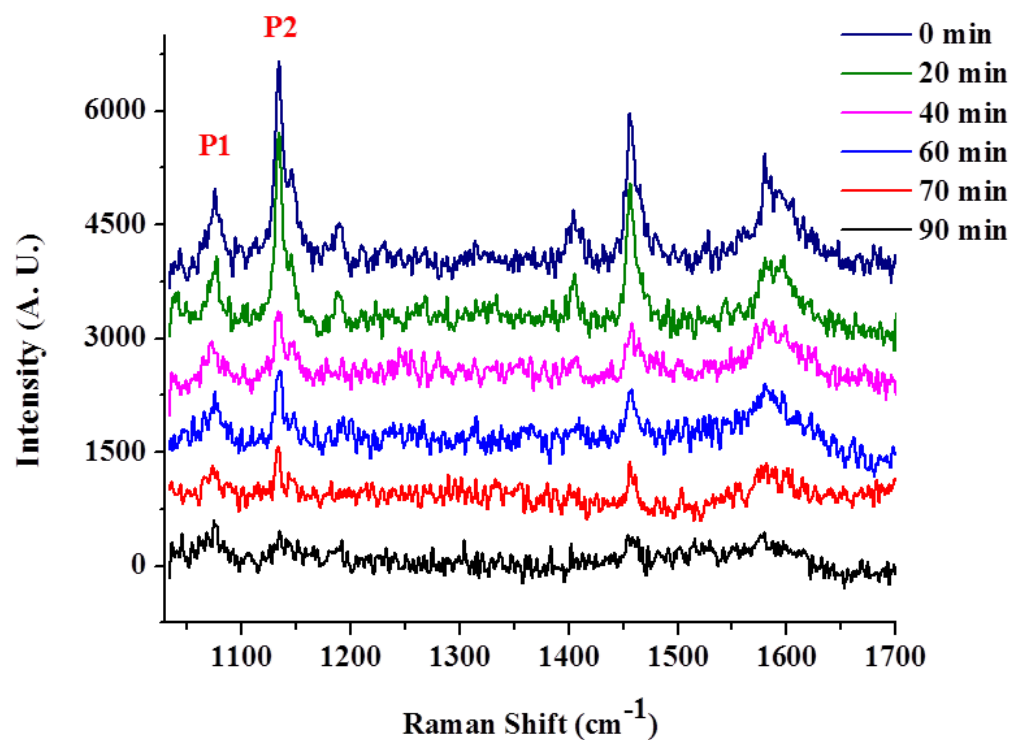


**Figure 5.5.** Experimental surface-enhanced Raman spectra of **Azo2** on Au{111} nanohole arrays as a function of UV irradiation time (see legend). The spectra have been offset for clarity. The peaks labeled P1 and P2 are used for monitoring the photoisomerization kinetics.

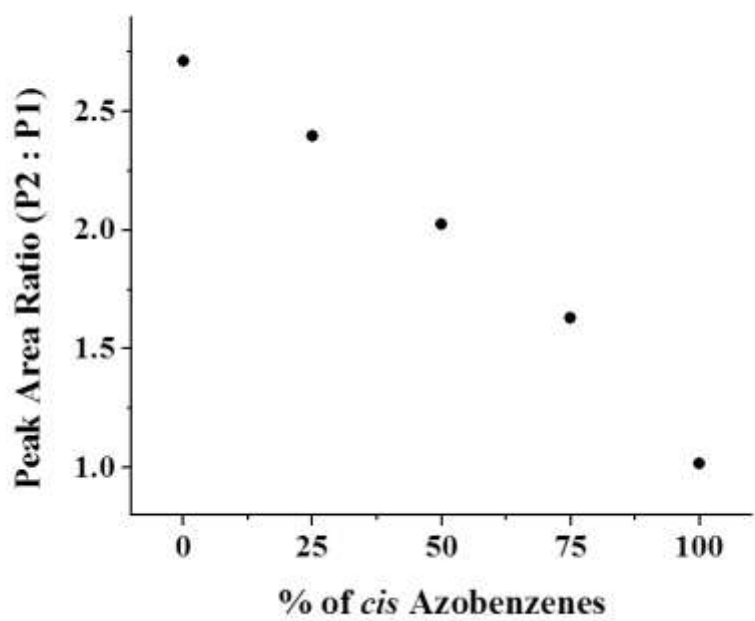
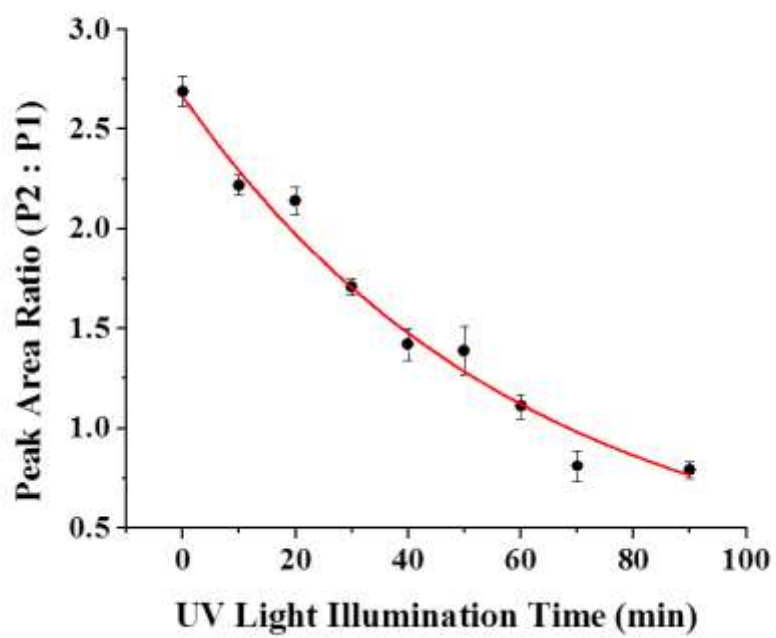


**Figure 5.6.** Top: Experimental decay plot of peak ratios tracking *trans* to *cis* conversion of **Azo2** on Au{111} nanohole array, demonstrating the reduction in the peak area ratio (P2:P1). The calculated time constant from the decay plot was  $61 \pm 11$  min. Bottom: Decay plot using peak area ratios from simulated SERS spectra showing the ratios expected as a function of photoconversion.

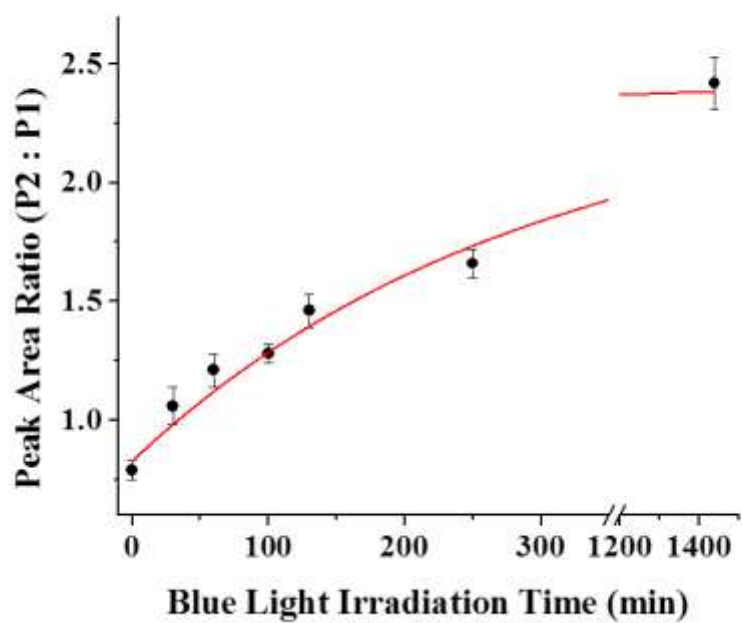
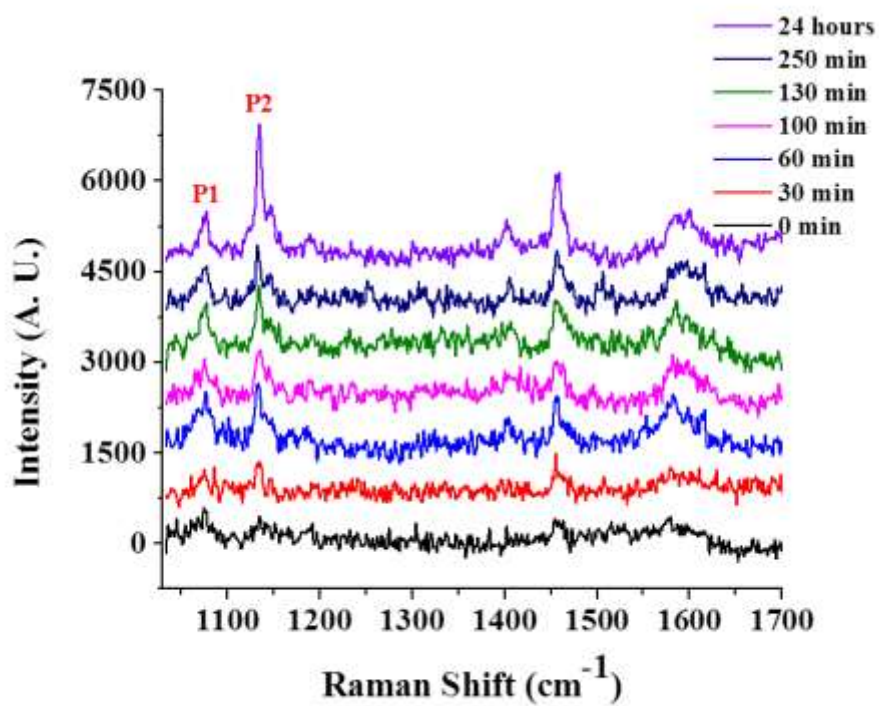


**Figure 5.7.** Top: The surface-enhanced Raman spectra showing the photoisomerization of **Azo2** back from *cis* to *trans* under visible light illumination over a period of 24 h (see legend). The spectra have been offset for clarity. Bottom: The exponential curve fit to the ratio of peak areas (P2: P1) shows the slower *cis* to *trans* back reaction. The x-axis has been truncated after 250 min to include the 24-h data point. The *cis* to *trans* photoisomerization of **Azo2** was found to be four times slower when compared to that of **Azo1**.

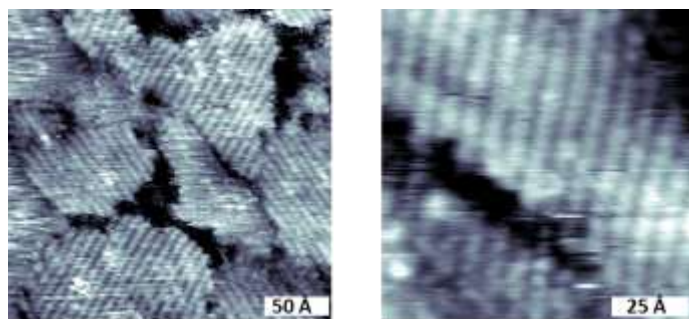


**Figure 5.8.** **Azo2** molecules assemble nominally perpendicular to the Au{111} surface as opposed to the tilted alignment of **Azo1** alkyl tethers. Imaging conditions:  $V_s = -1$  V,  $I = 1$  pA.

## 5.5 REFERENCES

1. Amabilino, D. B.; Stoddart, J. F. *Chem. Rev.* **1995**, *95*, 2725-2828.
2. Balzani, V.; Credi, A.; Raymo, F. M.; Stoddart, J. F. *Angew. Chem. Int. Ed.* **2000**, *39*, 3349-3391.
3. Feringa, B. L.; van Delden, R. A.; Koumura, N.; Geertsema, E. M. *Chem. Rev.* **2000**, *100*, 1789-1816.
4. Weiss, P. S. *Nature* **2001**, *413*, 585-586.
5. Flood, A. H.; Stoddart, J. F.; Steuerman, D. W.; Heath, J. R. *Science* **2004**, *306*, 2055-2056.
6. Barth, J. V.; Costantini, G.; Kern, K. *Nature* **2005**, *437*, 671-679.
7. Browne, W. R.; Feringa, B. L. *Nature Nanotech.* **2006**, *1*, 25-35.
8. Katsonis, N.; Lubomska, M.; Pollard, M. M.; Feringa, B. L.; Rudolf, P. *Prog. Surf. Sci.* **2007**, *82*, 407-434.
9. Kronemeijer, A. J.; Akkerman, H. B.; Kudernac, T.; van Wees, B. J.; Feringa, B. L.; Blom, P. W. M.; de Boer, B. *Adv. Mater.* **2008**, *20*, 1467-1473.
10. Weiss, P. S. *Acc. Chem. Res.* **2008**, *41*, 1772-1781.
11. Li, D.; Paxton, W. F.; Baughman, R. H.; Huang, T. J.; Stoddart, J. F.; Weiss, P. S. *MRS Bull.* **2009**, *34*, 671-681.
12. Kudernac, T.; Ruangsapichat, N.; Parschau, M.; Macia, B.; Katsonis, N.; Harutyunyan, S. R.; Ernst, K.-H.; Feringa, B. L. *Nature* **2011**, *479*, 208-211.
13. Weiss, P. S. *Nature* **2011**, *479*, 187-188.
14. Zheng, Y. B.; Pathem, B. K.; Hohman, J. N.; Thomas, J. C.; Kim, M.; Weiss, P. S. *Adv. Mater.* **2012**, *24*, in press. DOI: 10.1002/adma.201201532.



15. Evans, S. D.; Johnson, S. R.; Ringsdorf, H.; Williams, L. M.; Wolf, H. *Langmuir* **1998**, *14*, 6436-6440.
16. Zhang, C.; Du, M. H.; Cheng, H. P.; Zhang, X. G.; Roitberg, A. E.; Krause, J. L. *Phys. Rev. Lett.* **2004**, *92*, 158301.
17. Choi, B. Y.; Kahng, S. J.; Kim, S.; Kim, H.; Kim, H. W.; Song, Y. J.; Ihm, J.; Kuk, Y. *Phys. Rev. Lett.* **2006**, *96*, 156106.
18. Alemani, M.; Peters, M. V.; Hecht, S.; Rieder, K. H.; Moresco, F.; Grill, L. *J. Am. Chem. Soc.* **2006**, *128*, 14446-14447.
19. Henzl, J.; Mehlhorn, M.; Gawronski, H.; Rieder, K. H.; Morgenstern, K. *Angew. Chem. Int. Ed.* **2006**, *45*, 603-606.
20. Comstock, M. J.; Levy, N.; Kirakosian, A.; Cho, J. W.; Lauterwasser, F.; Harvey, J. H.; Strubbe, D. A.; Frechet, J. M. J.; Trauner, D.; Louie, S. G.; Crommie, M. F. *Phys. Rev. Lett.* **2007**, *99*, 038301.
21. Henningsen, N.; Rurali, R.; Franke, K. J.; Fernandez-Torrente, I.; Pascual, J. I. *Appl. Phys. A* **2008**, *93*, 241-246.
22. Kumar, A. S.; Ye, T.; Takami, T.; Yu, B. C.; Flatt, A. K.; Tour, J. M.; Weiss, P. S. *Nano Lett.* **2008**, *8*, 1644-1648.
23. Zarwell, S.; Rueck-Braun, K. *Tetrahedron Lett.* **2008**, *49*, 4020-4025.
24. Cho, J.; Berbil-Bautista, L.; Levy, N.; Poulsen, D.; Frechet, J. M. J.; Crommie, M. F. *J. Chem. Phys.* **2010**, *133*, 234707.
25. Gilat, S. L.; Kawai, S. H.; Lehn, J. M. *Chem. - Euro. J.* **1995**, *1*, 275-284.
26. Tian, H.; Yang, S. J. *Chem. Soc. Rev.* **2004**, *33*, 85-97.
27. Kobatake, S.; Takami, S.; Muto, H.; Ishikawa, T.; Irie, M. *Nature* **2007**, *446*, 778-781.

28. Raymo, F. M.; Alvarado, R. J.; Giordani, S.; Cejas, M. A. *J. Am. Chem. Soc.* **2003**, *125*, 2361-2364.
29. Zheng, Y. B.; Kiraly, B.; Cheunkar, S.; Huang, T. J.; Weiss, P. S. *Nano Lett.* **2011**, *11*, 2061-2065.
30. Gobbi, L.; Seiler, P.; Diederich, F.; Gramlich, V.; Boudon, C.; Gisselbrecht, J. P.; Gross, M. *Helv. Chim. Acta* **2001**, *84*, 743-777.
31. Boggio-Pasqua, M.; Bearpark, M. J.; Hunt, P. A.; Robb, M. A. *J. Am. Chem. Soc.* **2002**, *124*, 1456-1470.
32. Broman, S. L.; Petersen, M. A.; Tortzen, C. G.; Kadziola, A.; Kilsa, K.; Nielsen, M. B. *J. Am. Chem. Soc.* **2010**, *132*, 9165-9174.
33. Parker, C. R.; Tortzen, C. G.; Broman, S. L.; Schau-Magnussen, M.; Kilsa, K.; Nielsen, M. B. *Chem. Commun.* **2011**, *47*, 6102-6104.
34. Tsuji, T.; Takeuchi, H.; Egawa, T.; Konaka, S. *J. Am. Chem. Soc.* **2001**, *123*, 6381-6387.
35. Fliegl, H.; Kohn, A.; Hattig, C.; Ahlrichs, R. *J. Am. Chem. Soc.* **2003**, *125*, 9821-9827.
36. Zheng, Y. B.; Payton, J. L.; Chung, C.-H.; Liu, R.; Cheunkar, S.; Pathem, B. K.; Yang, Y.; Jensen, L.; Weiss, P. S. *Nano Lett.* **2011**, *11*, 3447-3452.
37. Comstock, M. J.; Strubbe, D. A.; Berbil-Bautista, L.; Levy, N.; Cho, J.; Poulsen, D.; Frechet, J. M. J.; Louie, S. G.; Crommie, M. F. *Phys. Rev. Lett.* **2010**, *104*, 178301/1-4.
38. Pechenezhskiy, I. V.; Cho, J.; Nguyen, G. D.; Berbil-Bautista, L.; Giles, B. L.; Poulsen, D. A.; Frechet, J. M. J.; Crommie, M. F. *J. Phys. Chem. C* **2012**, *116*, 1052-1055.
39. Henzl, J.; Puschnig, P.; Ambrosch-Draxl, C.; Schaate, A.; Ufer, B.; Behrens, P.; Morgenstern, K. *Phys. Rev. B* **2012**, *85*, 035410.
40. Zheng, Y. B.; Kiraly, B.; Weiss, P. S.; Huang, T. J. *Nanomedicine* **2012**, *7*, 751-770.

41. Lewis, P. A.; Inman, C. E.; Yao, Y. X.; Tour, J. M.; Hutchison, J. E.; Weiss, P. S. *J. Am. Chem. Soc.* **2004**, *126*, 12214-12215.
42. Moore, A. M.; Mantooth, B. A.; Donhauser, Z. J.; Maya, F.; Price, D. W.; Yao, Y. X.; Tour, J. M.; Weiss, P. S. *Nano Lett.* **2005**, *5*, 2292-2297.
43. Willner, I.; Rubin, S. *Angew. Chem. Int. Ed.* **1996**, *35*, 367-385.
44. Riskin, M.; Willner, I. *Langmuir* **2009**, *25*, 13900-13905.
45. Alemani, M.; Selvanathan, S.; Ample, F.; Peters, M. V.; Rieder, K.-H.; Moresco, F.; Joachim, C.; Hecht, S.; Grill, L. *J. Phys. Chem. C* **2008**, *112*, 10509-10514.
46. Jung, U.; Filinova, O.; Kuhn, S.; Zargarani, D.; Bornholdt, C.; Herges, R.; Magnussen, O. *Langmuir* **2010**, *26*, 13913-13923.
47. Xu, S.; Shan, J.; Shi, W.; Liu, L.; Xu, L. *Opt. Express* **2011**, *19*, 12336-12341.
48. Shipway, A. N.; Katz, E.; Willner, I. *Chemphyschem* **2000**, *1*, 18-52.
49. Stavvytska-Barba, M.; Salvador, M.; Kulkarni, A.; Ginger, D. S.; Kelley, A. M. *J. Phys. Chem. C* **2011**, *115*, 20788-20794.
50. Qune, L. F. N. A.; Akiyama, H.; Nagahiro, T.; Tamada, K.; Wee, A. T. S. *Appl. Phys. Lett.* **2008**, *93*, 083109/1-3.
51. Wagner, S.; Leyssner, F.; Koerdel, C.; Zarwell, S.; Schmidt, R.; Weinelt, M.; Rueck-Braun, K.; Wolf, M.; Tegeder, P. *Phys. Chem. Chem. Phys.* **2009**, *11*, 6242-6248.
52. Ye, T.; Kumar, A. S.; Saha, S.; Takami, T.; Huang, T. J.; Stoddart, J. F.; Weiss, P. S. *ACS Nano* **2010**, *4*, 3697-3701.
53. Moore, A. M.; Yeganeh, S.; Yao, Y.; Claridge, S. A.; Tour, J. M.; Ratner, M. A.; Weiss, P. S. *ACS Nano* **2010**, *4*, 7630-7636.

54. Zheng, Y. B.; Pathem, B. K.; Payton, J. L.; Bob, B.; Kumar, A. S.; Chung, C.-H.; Yu, B. C.; Yang, Y.; Tour, J. M.; Jensen, L.; Weiss, P. S. *To be submitted*.
55. Joachim, C. *New J. Chem.* **1991**, *15*, 223-229.
56. Bumm, L. A.; Arnold, J. J.; Cygan, M. T.; Dunbar, T. D.; Burgin, T. P.; Jones, L.; Allara, D. L.; Tour, J. M.; Weiss, P. S. *Science* **1996**, *271*, 1705-1707.
57. Bumm, L. A.; Arnold, J. J.; Dunbar, T. D.; Allara, D. L.; Weiss, P. S. *J. Phys. Chem. B* **1999**, *103*, 8122-8127.
58. Holmlin, R. E.; Ismagilov, R. F.; Haag, R.; Mujica, V.; Ratner, M. A.; Rampi, M. A.; Whitesides, G. M. *Angew. Chem. Int. Ed.* **2001**, *40*, 2316-2320.
59. Beebe, J. M.; Engelkes, V. B.; Miller, L. L.; Frisbie, C. D. *J. Am. Chem. Soc.* **2002**, *124*, 11268-11269.
60. Salomon, A.; Cahen, D.; Lindsay, S.; Tomfohr, J.; Engelkes, V. B.; Frisbie, C. D. *Adv. Mater.* **2003**, *15*, 1881-1890.
61. Engelkes, V. B.; Beebe, J. M.; Frisbie, C. D. *J. Am. Chem. Soc.* **2004**, *126*, 14287-14296.
62. Monnell, J. D.; Stapleton, J. J.; Dirk, S. M.; Reinerth, W. A.; Tour, J. M.; Allara, D. L.; Weiss, P. S. *J. Phys. Chem. B* **2005**, *109*, 20343-20349.
63. Kim, B.; Choi, S. H.; Zhu, X. Y.; Frisbie, C. D. *J. Am. Chem. Soc.* **2011**, *133*, 19864-19877.
64. Sachs, S. B.; Dudek, S. P.; Hsung, R. P.; Sita, L. R.; Smalley, J. F.; Newton, M. D.; Feldberg, S. W.; Chidsey, C. E. D. *J. Am. Chem. Soc.* **1997**, *119*, 10563-10564.
65. Donhauser, Z. J.; Mantooth, B. A.; Kelly, K. F.; Bumm, L. A.; Monnell, J. D.; Stapleton, J. J.; Price, D. W.; Rawlett, A. M.; Allara, D. L.; Tour, J. M.; Weiss, P. S. *Science* **2001**, *292*, 2303-2307.

66. Kushmerick, J. G.; Holt, D. B.; Pollack, S. K.; Ratner, M. A.; Yang, J. C.; Schull, T. L.; Naciri, J.; Moore, M. H.; Shashidhar, R. *J. Am. Chem. Soc.* **2002**, *124*, 10654-10655.
67. Zheng, Y. B.; Pathem, B. K.; Payton, J. L.; Song, T.-B.; Bob, B.; Kumar, A. S.; Yu, B. C.; Yang, Y.; Jensen, L.; Tour, J. M.; Weiss, P. S. *To be submitted*.
68. Donhauser, Z. J.; Price, D. W.; Tour, J. M.; Weiss, P. S. *J. Am. Chem. Soc.* **2003**, *125*, 11462-11463.
69. Stranick, S. J.; Parikh, A. N.; Allara, D. L.; Weiss, P. S. *J. Phys. Chem.* **1994**, *98*, 11136-11142.
70. Bumm, L. A.; Arnold, J. J.; Charles, L. F.; Dunbar, T. D.; Allara, D. L.; Weiss, P. S. *J. Am. Chem. Soc.* **1999**, *121*, 8017-8021.
71. Valiev, M.; Bylaska, E. J.; Govind, N.; Kowalski, K.; Straatsma, T. P.; van Dam, H. J. J.; Wang, D.; Nieplocha, J.; Apra, E.; Windus, T. L.; de Jong, W. A. *Comput. Phys. Commun.* **2010**, *181*, 1477.
72. Yang, G. H.; Qian, Y. L.; Engtrakul, C.; Sita, L. R.; Liu, G. Y. *J. Phys. Chem. B* **2000**, *104*, 9059-9062.

## **CHAPTER 6**

### ***PHOTOREACTION OF MATRIX-ISOLATED DIHYDROAZULENE-FUNCTIONALIZED MOLECULES ON Au{111}***

## 6.1 INTRODUCTION

Functionalization of solid substrates with molecules capable of performing specific functions when subjected to external stimuli is of great interest in the fields of electronics (display technologies),<sup>1-5</sup> biology,<sup>6-9</sup> medicine,<sup>10-13</sup> energy,<sup>14,15</sup> and nanoelectromechanics.<sup>16-23</sup> The functional molecules should be able to switch reversibly between two or more stable or metastable states. Moreover, these molecules must retain their functionality when they are assembled on solid substrates in order to be efficiently utilized in electromechanical applications. For instance, it is well established that the photoisomerization of functional molecules is quenched when deposited on conductive substrates due not only to the underlying substrates but also to the surrounding environments.<sup>24,25</sup> Hence, it is desirable to decouple (electronically) the functional group from the surface and to isolate the molecules from each other in order to understand the single molecular photokinetic behavior. Much research has focused on finding and optimizing molecular switch candidates capable of responding to a variety of external stimuli such as light,<sup>24-35</sup> electric field,<sup>19,36-39</sup> electrochemical potential,<sup>16,20-22</sup> or heat.<sup>40,41</sup> Of all the external stimuli mentioned above, light offers a straightforward means to excite and to probe the functional molecules assembled on solid substrates, because it is non-invasive, preserves the surface integrity, and is easily addressable. Various families of molecular switches have been synthesized to meet such requirements, including, azobenzenes,<sup>24,25,29,30,33</sup> spiropyrans,<sup>42-45</sup> stilbenes,<sup>46-48</sup> diarylethenes,<sup>49-52</sup> rotaxanes,<sup>16,20-22,53</sup> oligo(phenylene ethynylene)s,<sup>36,37,54-57</sup> dithienylethenes,<sup>58-61</sup> and dihydroazulenes<sup>32,41,46,62-66</sup> (**DHAs**). However, the quest for highly efficient surface-bound molecular switches continues.

It is well established that the photoreaction quantum yield of **DHAs** is higher than that of azobenzenes and stilbenes, and yet **DHA** systems have not been extensively studied as molecular

switches on solid substrates, until recently in single-molecule junctions.<sup>32,67</sup> When irradiated with UV light, **DHA** undergoes a 10-electron retro-electrocyclization to vinylheptafulvene (**VHF**) that exists in equilibrium between *s-cis* and *s-trans* conformations.<sup>68</sup> It is also known that **VHF** undergoes a ring-closing reaction to **DHA** via thermal relaxation through the *s-cis* conformation. It has been shown that the absorption maximum of **DHA** can be tuned by tailoring the substituents on the functional moiety. Although reversible transformation between **DHA** and **VHF** isomers has been well established in solution,<sup>46,64,65,68-76</sup> the photochromism has not been extensively studied when these molecules are bound to solid substrates.<sup>32</sup> To that end, we have designed a S-(4-((4-(1,1-dicyano-1,8a-dihydroazulen-2-yl)phenyl)ethynyl)phenyl)ethanethioate molecule (henceforth **DHA'**) and studied the photokinetics by assembling them as isolated single molecules on a Au{111} nanohole array. By attaching an acetyl-protected thiolate via a tolane linker to the five-membered ring of **DHA**, we were not only able to separate the functional moiety spatially from the underlying substrate but also to restrict the photoreaction to just the *s-cis* conformation.<sup>24,25,33</sup> We employed highly sensitive SERS to monitor the kinetics of photoreaction due to its high sensitivity to molecular conformation, non-destructive nature, and high throughput.<sup>33</sup> We interpret our experimental measurements and analyses with supporting density functional theory calculations.

We have previously demonstrated a sensitive means to follow the photoisomerization kinetics of functional molecules assembled on atomically flat surfaces using SERS.<sup>33</sup> By employing a Au nanohole array substrate we have shown that the vibrational modes of the molecule are enhanced using plasmonics, which are otherwise not detectable when a substrate without nanoholes is used. We employ the same technique here to follow the photoreaction kinetics of **DHA'** molecules assembled on Au{111} nanohole array substrates.



## 6.2 METHODS

Focused ion beam (FIB) lithography (Nova 600 NanoLab, FEI Company, Hillsboro, OR, USA) was used to fabricate cylindrical nanoholes (with a diameter of 175 nm) in square arrays (with a period of 300 nm) into Au thin films.

The samples were prepared by flame-annealing a Au{111} nanohole array substrate and then subsequently immersing it in a 1:4 mixture of ethanolic solutions of **DHA'** and **C12** in the dark such that the final solution concentration was 1 mM. The sample was then stored in the dark and under nitrogen atmosphere for 24 h. Subsequently, the sample was rinsed with ethanol and then vapor annealed over **C12** solutions at 80 °C for 2 h in order to increase the crystallinity of the matrices by backfilling the **C12** molecules into existing defect sites. This procedure resulted in the formation of tightly packed large domains of the host molecular monolayer matrix with the dilute **DHA'** molecules isolated as single molecules within the domains of the **C12** matrix.<sup>25,33,77,78</sup> Thus, random diffusion of the isolated **DHA** molecules on the substrate was restricted. The samples were stored in the dark until further analysis. Figure 6.1 shows a schematic of the assembly of isolated single molecules in a host **C12** matrix. The molecule exists in a thermodynamically favorable, closed ring **DHA** isomer and switches to corresponding vinylheptafulvene (henceforth **VHF'**) isomer upon illumination with 365 nm UV light. The thermal back reaction occurs at 30 °C.

A Renishaw inVia Raman system (Renishaw Inc., Illinois, USA) was employed for Raman analysis. A 632.8 nm He-Ne laser was chosen as the Raman excitation source taking into consideration the resonant wavelength of the Au substrates. Laser power and beam diameter were ~17 mW and ~1  $\mu$ m, respectively. All the Raman measurements were performed under

ambient conditions. Each measurement was a convolution of 50 sweeps in the wavelength range of interest with a set integration time of 150 s. Raman spectra, individual peak intensities, and the time constants from the exponential curves were calculated using Wire 3.2 and OriginPro software packages.

The samples were analyzed in a dark room by exposing the substrate to a ~365 nm UV lamp source. Time course measurements were performed over a period of 60 min. The power of the UV source was held constant ( $570 \mu\text{W}/\text{cm}^2$ ), similar to our previous measurements.<sup>33</sup> After each successive UV illumination time period, Raman spectra were collected in the same location of the substrate. Since it is common to observe a slight increase in temperature where the laser is focused on the during the Raman measurements, the sample was allowed to cool down naturally after the final UV measurements before performing the thermal relaxation measurements. The sample was then held at a constant temperature of 30 °C and time course measurements were performed at regular time intervals until the ratio of peak intensities saturated.

The NWChem package<sup>79</sup> was used to calculate the Raman spectra of **DHA'** and **VHF'** formations. The ground state geometry and normal modes were calculated using DFT<sup>80,81</sup> and the polarizability was calculated using TDDFT.<sup>82</sup> In all cases, the B3LYP functional<sup>83</sup> and the 6-311G\* basis set from the NWChem basis set library were used. The differential Raman cross sections were calculated using a three-point numerical differentiation of the polarizability for each normal mode<sup>79</sup> and an assumed incident laser wavelength of 633 nm. The differential Raman cross sections were broadened using a Lorentzian function with a full width at half maximum (FWHM) of  $20 \text{ cm}^{-1}$ . The Raman intensities for a mixture of open and closed isomers for a given normal mode  $k$  ( $I^{\text{Mixed}}_k$ ) was calculated as  $I^{\text{Mixed}}_k = x^{\text{Open}} * I^{\text{Open}}_k + x^{\text{Closed}} * I^{\text{Closed}}_k$ , where  $x^{\text{Open}}$  and  $x^{\text{Closed}}$  are the mole fractions of the open and closed isomers, respectively, and

$I_k^{\text{Open}}$  and  $I_k^{\text{Closed}}$  are the Raman intensity of the open and closed isomers for the  $k^{\text{th}}$  normal mode, respectively.

### 6.3 RESULTS AND DISCUSSIONS

The calculated **DHA'** Raman spectrum (Fig. 6.2) revealed five distinct peaks in the range of 1000-1700  $\text{cm}^{-1}$ , with peak positions at 1112, 1166, 1230, 1572, and 1618  $\text{cm}^{-1}$ . The peak at 1112  $\text{cm}^{-1}$  is due to the ring breathing modes of the tether (parallel to the S-C bond) that was employed to attach the functional moiety to the underlying Au substrate. The motion symmetrically localized around the  $\text{C}\equiv\text{C}$  stretch attached to the functional moiety has an intense peak positioned at 1166  $\text{cm}^{-1}$ . The peak at 1230  $\text{cm}^{-1}$  arises due to intense symmetric H wagging modes of the benzene spacer unit. The C-C stretching modes and in-plane H wagging motion of the five-membered ring of the functional moiety give rise to a distinct peak at 1572  $\text{cm}^{-1}$  and the prominent C-C stretch in the five-membered ring of the functional moiety results in peak at 1618  $\text{cm}^{-1}$  (Fig. 6.3). In order to follow the surface photokinetics, we simulated the Raman spectra of the **VHF'** isomer and the intermediate spectra of **DHA'** and **VHF'** at different mole fractions. As can be seen from Fig. 6.2, the intensities of all the peaks decrease dramatically as the photoreaction proceeds from **DHA'** to **VHF'**, except for the peak at 1112  $\text{cm}^{-1}$ , labeled P1. Since this peak arises due to the vibrational modes of the tether unit (Fig. 6.4), the photoreaction has no effect on the peak intensity. The peak labeled P2, on the other hand, is directly affected due to the cross-conjugation in the five-membered ring of the functional moiety and the intensity of C-H bending vibrational modes decreases as the photoreaction proceeds from **DHA'** to **VHF'** (See Fig. 6.4). Thus, monitoring the peak intensities of peaks labeled P1 and P2 experimentally, provides a direct measure of the fractions of reactant and product. Figure 6.4 shows the vibrational modes of **DHA'** and **VHF'** isomers that give rise to peaks P1 and P2, respectively.

Figure 6.5 shows a series of Raman spectra collected over time as described in the experimental section above. Four distinct peaks in the 1000-1700  $\text{cm}^{-1}$  range are observed. The spectra are measured as a function of illumination time and are offset for clarity. Although peaks P1 and P2 are well resolved, the peaks at 1580 and 1610  $\text{cm}^{-1}$  (corresponding to 1572 and 1618  $\text{cm}^{-1}$  in the simulated spectra), were not completely resolved and thus were not considered for quantification. Also, it can be seen that the intensity of peak P1 remains constant, in agreement with simulations. We thus chose P1 as an internal standard. Since the peak intensity of P1 is the least affected by the **DHA'**→**VHF'** photoreaction, comparison of the intensity of P2 with that of P1 provides a direct measurement of the progress of the photoreaction on the surface. Hence, we measured the ratio of the peaks P2 and P1 (P2:P1) and monitored it as a function UV illumination time.

The series of Raman spectra in Fig. 6.5 show that the intensity of P2 decreases dramatically with UV illumination time, while the intensity of P1 remains constant, indicating the forward photoreaction of **DHA'** to **VHF'**. The UV measurements were stopped when the ratio of peak intensities saturated. The samples were then cooled to room temperature for a few minutes and were maintained at a constant temperature of 30 °C. Time course Raman measurements were performed as a function of time at constant temperature. Relevant series of Raman spectra can be seen in Fig. 6.6. As can be seen, the intensities of peaks other than P1 increase as a function of time. The peak intensities in the Raman spectra after 60 min of measurements was observed to be close to those of the initial (pre-illumination) measurements, however, the ratio of the peaks was still lower than the initial values, indicating that the thermal back reaction was not yet complete. By 120 min, the peak ratios saturated.

Figure 6.7a shows an exponential fit to the decay curve plotted for P2:P1 peak ratios with respect to UV illumination time. The error bars are from five measurements performed on five different nanohole array substrates. The P2:P1 ratio saturated after about 25 min of UV illumination. The minimal deviation in the data points after the 25 min mark from five different measurements indicates the robustness of the SERS measurement technique. The data were fit with an exponential curve with the formula  $Y=Y_0+A*\exp(R_0t)$ , where  $R_0$  is the decay constant of the best fit curve, with units of  $\text{time}^{-1}$ . The time constant was then calculated by taking the inverse of the decay constant in units of min. The time constant extracted for the **DHA'** to **VHF'** photoreaction was  $9 \pm 2$  min. This is in agreement with our previous single-molecule measurements where the onset of photoreaction was observed to occur after 10-20 min of UV illumination.<sup>32</sup> The correlation of the single-molecule measurements with those of the ensemble measurements of surface-bound molecules reveals that the photoreaction quantum yield of the **DHA** moieties is higher even when assembled and isolated on surfaces, when compared to other photochromic molecules such as azobenzenes and stilbenes.<sup>32</sup> As a comparison figure of merit, isolated azobenzenes with saturated tethers exhibit photoisomerization time constant of ~38 min studied using the same measurement conditions and techniques<sup>33</sup> and ~54 min when studied using high-resolution scanning tunneling microscopy (STM).<sup>25</sup>

Figure 6.7b shows the exponential increase in P2:P1 as a function of thermal relaxation time. The ratio of peak intensities increased as a function of time and eventually saturated after 120 min, indicating completion of the surface-bound **VHF'**→**DHA'** thermal back reaction. The time constant calculated was similar to that of the UV-induced forward reaction measurement,  $38 \pm 7$  min. The ratio (P2:P1) of peak intensities from theoretical calculations were also plotted as a function of **VHF'** mole fractions in order to compare with the experimentally observed trend.

A decreasing trend in the peak ratio with increasing mole fraction of **VHF'** was observed (Fig. 6.8), further providing support to our experiment.

In order to improve the efficiency of controlled molecular motion and function of surfaces functionalized with switches, molecules with higher photoisomerization quantum yield have to be employed. *Trans*→*cis* photoreaction of azobenzene, for example, has an average quantum yield of ~0.2 and a yield of ~0.5 for the reverse reaction,<sup>84,85</sup> whereas **DHA**→**VHF** photoreaction in acetonitrile has a quantum yield of 0.55.<sup>70</sup> We calculated the photoisomerization cross sections of the current **DHA'** system and compared them to those of our previous measurements of azobenzene-functionalized molecules performed under identical conditions to get a quantitative estimate of the photoisomerization efficiency. By using the formula  $\sigma = hc/(\lambda\tau I_0)$ , where  $h$  is Planck's constant,  $c$  the speed of light,  $\lambda$  the wavelength of irradiation (365 nm),  $\tau$  the time constant, and  $I_0$  the power of the UV light source (570  $\mu\text{W}/\text{cm}^2$ ), we get the photoisomerization cross section with units of  $\text{cm}^2$ . In solution, we observe switching times of 1 min,<sup>32</sup> corresponding to  $\sigma_{\text{soln}} = 2 \times 10^{-17} \text{ cm}^2$ ; similarly, we found that the photoisomerization cross section of surface-bound **DHA'** molecules with a rate constant of 9 min under these conditions gives  $\sigma_{\text{bound}} = 1.5 \times 10^{-18} \text{ cm}^2$ , in reasonable agreement with our previous single-molecule measurements.<sup>32</sup> These cross sections are an order of magnitude lower than those observed in solution. However, when compared with measurements of azobenzene-functionalized molecules studied under the identical conditions and with those measured using STM, we find that the surface-bound photoreaction cross section for **DHA'** is higher, where  $\sigma_{\text{Azo}}$  varied between  $4 \times 10^{-19}$  and  $8 \times 10^{-20} \text{ cm}^2$  depending upon the conductance of the tether and the degree of spatial separation of the functional moiety from the underlying substrate.<sup>24,33</sup>

## 6.4 CONCLUSIONS AND FUTURE PROSPECTS

We have designed novel photochromic dihydroazulene-functionalized molecules and isolated them as single molecules on Au{111} nanohole arrays. The cross sections derived from SERS measurements as a function of UV illumination time reveal the high photoswitching efficiency of the functional molecules, compared to previous studies on various other surface-bound photoswitches. Furthermore, the reversibility of the dihydroazulene photoreactions via thermal relaxation has also been established. Since these molecules do not need large free volume to isomerize, these molecules could be used to fabricate 2D films on Au{111} and the reversibility of the entire monolayer between the two isomeric states could be achieved. Atomic force microscopy can be employed to study the I-V characteristics of the 2D films before and after illumination with UV light and subsequently after thermal relaxation. In conjunction with theory, the reversible changes in the conductance of the molecules can be established.

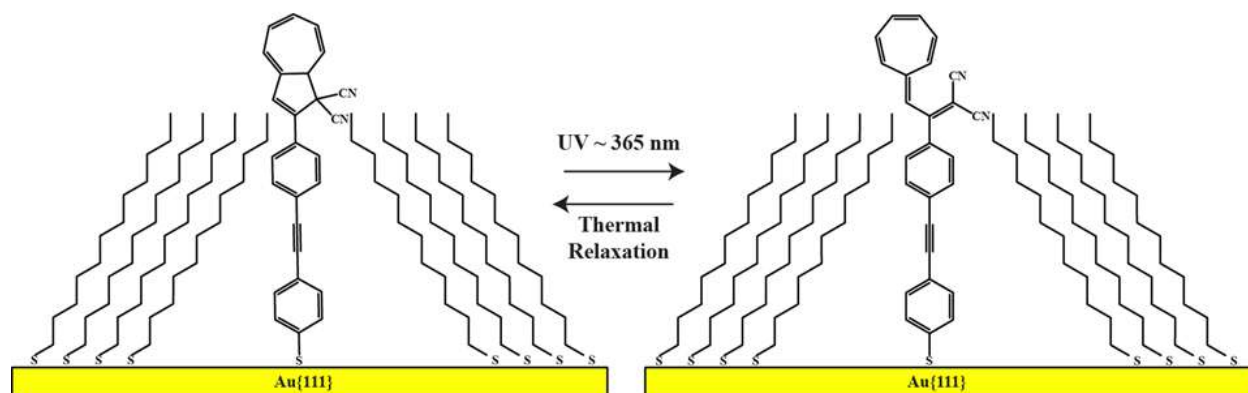


**Figure 6.1.** Schematic of UV-light-induced photoreaction of functionalized dihydroazulene (**DHA'**, left) to a vinylheptafulvene (**VHF'**, right) isolated as single molecules in a dodecanethiol (**C12**) matrix and the back reaction via thermal relaxation.



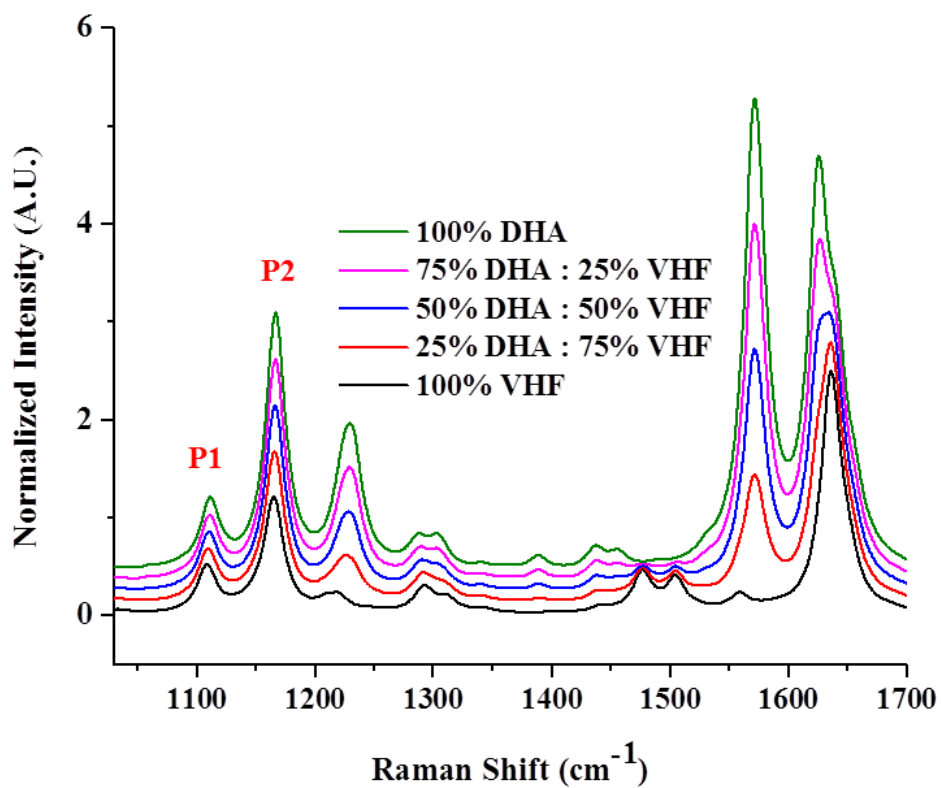


**Figure 6.2.** Series of theoretical simulations of Raman spectra as a mixture of different mole fractions of functionalized dihydroazulene (**DHA'**) and corresponding vinylheptafulvene (**VHF'**), spectra are offset for clarity. Peaks labeled P1 and P2 were used to follow the photoreaction spectroscopically.

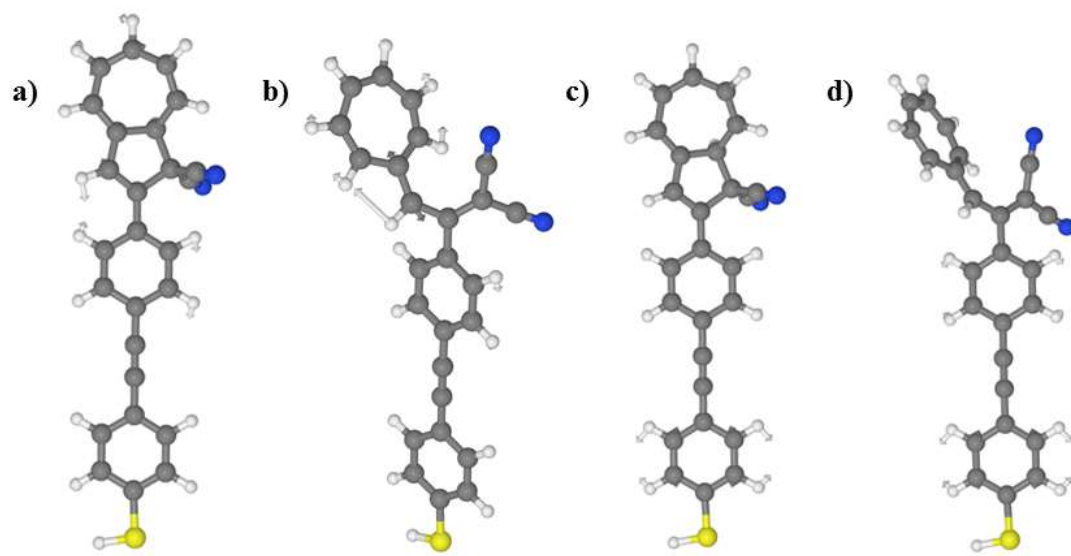


**Figure 6.3.** Vibrational modes of the peaks at  $1572\text{ cm}^{-1}$  in dihydroazulene (**DHA'**) and vinylheptafulvene (**VHF'**) isomers, respectively.

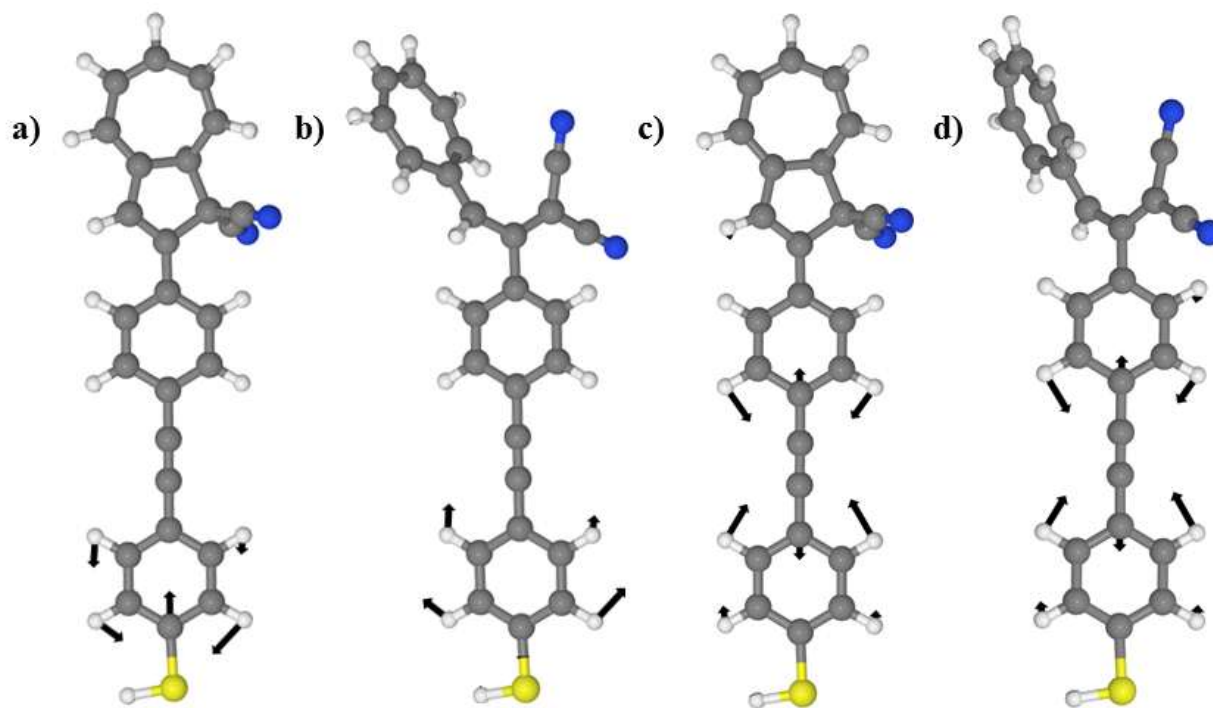


**Figure 6.4.** Vibrational mode P1 of a) functionalized dihydroazulene (**DHA'**) and b) vinylheptafulvene (**VHF'**) isomers. Vibrational mode P2 of c) **DHA'** and d) **VHF'** isomers.

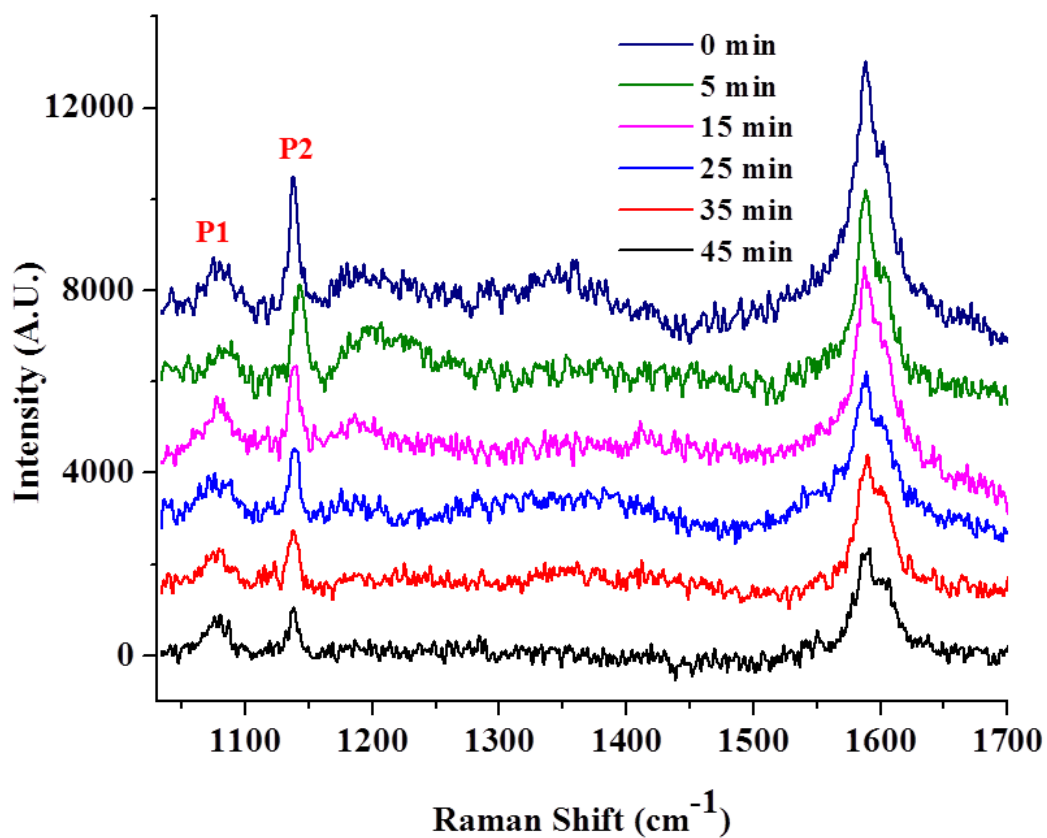


**Figure 6.5.** Series of experimental surface-enhanced Raman spectra as a function of 365 nm UV light illumination time (the legend shows the duration of light illumination). The ratio of peaks labeled P1 and P2 was used to follow the kinetics of surface-bound molecular photoreaction. The spectra are offset for clarity.

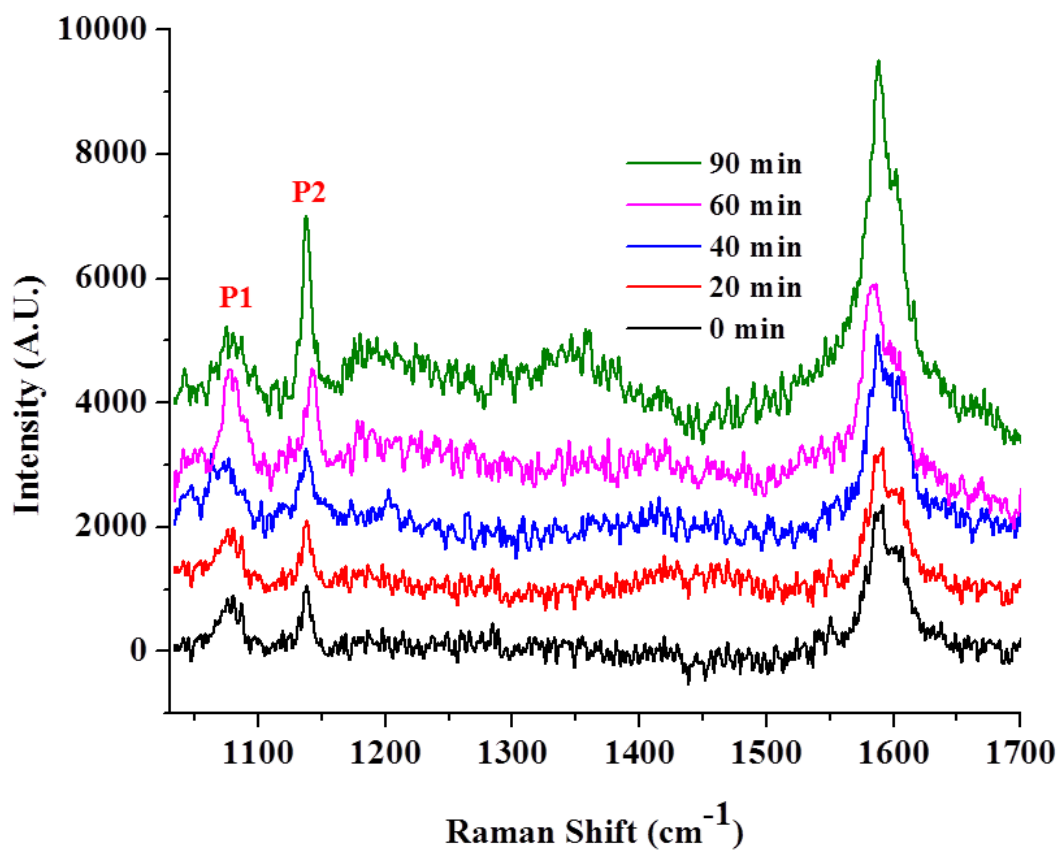


**Figure 6.6.** Series of experimental surface-enhanced Raman spectra as a function of thermal relaxation time (the legend shows the thermal relaxation time at 30 °C). The spectra are offset for clarity.

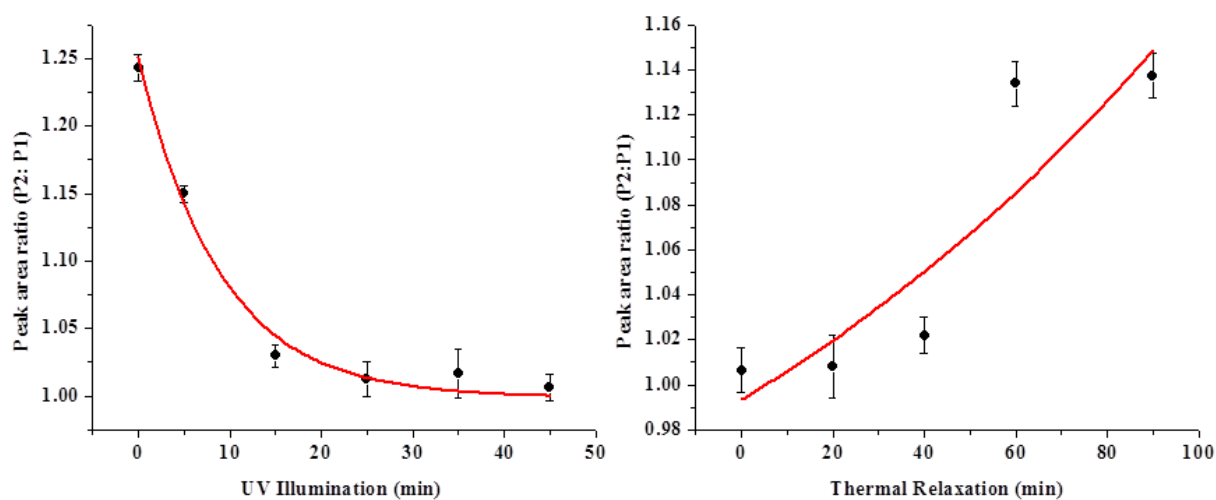


**Figure 6.7.** (Left) The peak area ratio (P2:P1) as a function of UV light irradiation time fit to an exponential decay. The extracted time constant for dihydroazulene to vinylheptafulvene (**DHA'**→**VHF'**) photoreaction was  $9\pm 2$  min. (Right) Data showing the increase in P2:P1 ratio as a function of thermal relaxation time at a constant temperature of 30 °C, also fit to an exponential curve. The time constant for the **VHF'**→**DHA'** thermal back reaction was  $38\pm 7$  min. The errors bars are from five sets of measurements.

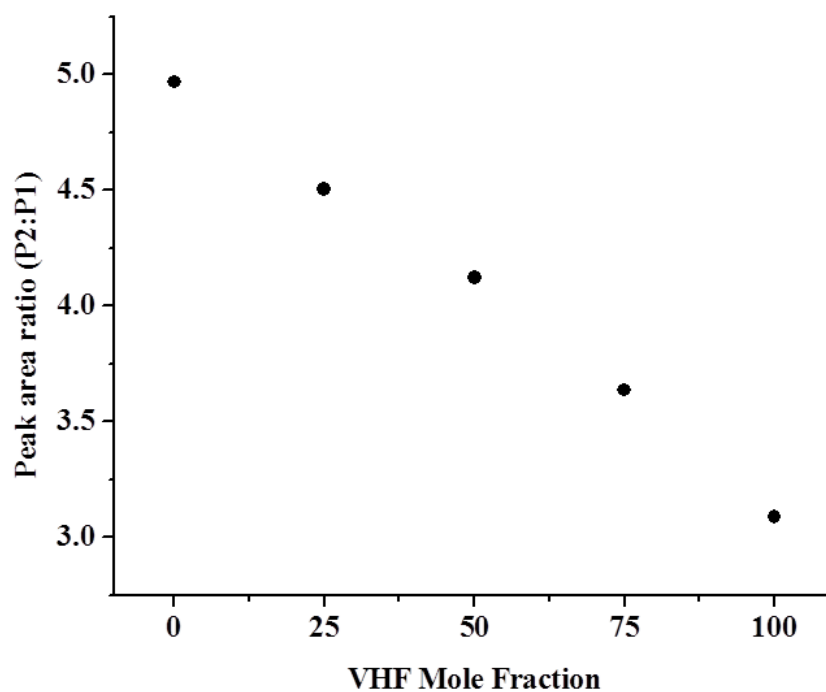


**Figure 6.8.** Plot showing the decrease in the P2:P1 peak area ration from simulated spectra as a function of **VHF'** mole fraction.

## 6.5 REFERENCES

1. Forrest, S. R. *Nature* **2004**, 428, 911-918.
2. Veinot, J. G. C.; Marks, T. J. *Acc. Chem. Res.* **2005**, 38, 632-643.
3. Chu, C. W.; Ouyang, J.; Tseng, J. H.; Yang, Y. *Adv. Mater.* **2005**, 17, 1440-1443.
4. Saragi, T. P. I.; Spehr, T.; Siebert, A.; Fuhrmann-Lieker, T.; Salbeck, J. *Chem. Rev.* **2007**, 107, 1011-1065.
5. Ma, H.; Yip, H.-L.; Huang, F.; Jen, A. K. Y. *Adv. Funct. Mater.* **2010**, 20, 1371-1388.
6. Falconnet, D.; Csucs, G.; Michelle Grandin, H.; Textor, M. *Biomaterials* **2006**, 27, 3044-3063.
7. Wang, L.; Fine, D.; Sharma, D.; Torsi, L.; Dodabalapur, A. *Analyt. Bioanalyt. Chem.* **2006**, 384, 310-321.
8. Slowing, I. I.; Trewyn, B. G.; Giri, S.; Lin, V. S. Y. *Adv. Funct. Mater.* **2007**, 17, 1225-1236.
9. Mendes, P. M. *Chem. Soc. Rev.* **2008**, 37, 2512-2529.
10. Sanchez, C.; Julian, B.; Belleville, P.; Popall, M. *J. Mater. Chem.* **2005**, 15, 3559-3592.
11. Ma, P. X. *Adv. Drug. Deliv. Rev.* **2008**, 60, 184-198.
12. Zhang, L.; Webster, T. J. *Nano Today* **2009**, 4, 66-80.
13. Giljohann, D. A.; Seferos, D. S.; Daniel, W. L.; Massich, M. D.; Patel, P. C.; Mirkin, C. A. *Angew. Chem. Int. Ed.* **2010**, 49, 3280-3294.
14. Xue, J.; Rand, B. P.; Uchida, S.; Forrest, S. R. *Adv. Mater.* **2005**, 17, 66-71.
15. Mihailetschi, V. D.; Koster, L. J. A.; Blom, P. W. M.; Melzer, C.; de Boer, B.; van Duren, J. K. J.; Janssen, R. A. J. *Adv. Funct. Mater.* **2005**, 15, 795-801.
16. Bissell, R. A.; Cordova, E.; Kaifer, A. E.; Stoddart, J. F. *Nature* **1994**, 369, 133-137.



17. Balzani, V.; Credi, A.; Raymo, F. M.; Stoddart, J. F. *Angew. Chem. Int. Ed.* **2000**, *39*, 3349-3391.
18. Collin, J.-P.; Dietrich-Buchecker, C.; Gaviña, P.; Jimenez-Molero, M. C.; Sauvage, J.-P. *Acc. Chem. Res.* **2001**, *34*, 477-487.
19. Li, D. B.; Paxton, W. F.; Baughman, R. H.; Huang, T. J.; Stoddart, J. F.; Weiss, P. S. *MRS Bull.* **2009**, *34*, 671-681.
20. Zheng, Y. B.; Yang, Y.-W.; Jensen, L.; Fang, L.; Juluri, B. K.; Flood, A. H.; Weiss, P. S.; Stoddart, J. F.; Huang, T. J. *Nano Lett.* **2009**, *9*, 819-825.
21. Juluri, B. K.; Kumar, A. S.; Liu, Y.; Ye, T.; Yang, Y.-W.; Flood, A. H.; Fang, L.; Stoddart, J. F.; Weiss, P. S.; Huang, T. J. *ACS Nano* **2009**, *3*, 291-300.
22. Ye, T.; Kumar, A. S.; Saha, S.; Takami, T.; Huang, T. J.; Stoddart, J. F.; Weiss, P. S. *ACS Nano* **2010**, *4*, 3697-3701.
23. Zheng, Y. B. P., B. K.; Hohman, J. N.; Thomas, J. C.; Kim, M.; Weiss, P. S. *Adv. Mater.* **2012**, *24*, in press. DOI: 10.1002/adma.201201532.
24. Comstock, M. J.; Levy, N.; Kirakosian, A.; Cho, J. W.; Lauterwasser, F.; Harvey, J. H.; Strubbe, D. A.; Frechet, J. M. J.; Trauner, D.; Louie, S. G.; Crommie, M. F. *Phys. Rev. Lett.* **2007**, *99*, 038301.
25. Kumar, A. S.; Ye, T.; Takami, T.; Yu, B. C.; Flatt, A. K.; Tour, J. M.; Weiss, P. S. *Nano Lett.* **2008**, *8*, 1644-1648.
26. Willner, I.; Rubin, S. *Angew. Chem. Int. Ed.* **1996**, *35*, 367-385.
27. Koumura, N.; Zijlstra, R. W. J.; van Delden, R. A.; Harada, N.; Feringa, B. L. *Nature* **1999**, *401*, 152-155.

28. Feringa, B. L.; van Delden, R. A.; Koumura, N.; Geertsema, E. M. *Chem. Rev.* **2000**, *100*, 1789-1816.
29. Hugel, T.; Holland, N. B.; Cattani, A.; Moroder, L.; Seitz, M.; Gaub, H. E. *Science* **2002**, *296*, 1103-1106.
30. Banghart, M.; Borges, K.; Isacoff, E.; Trauner, D.; Kramer, R. H. *Nature Neurosci.* **2004**, *7*, 1381-1386.
31. Weiss, P. S. *Acc. Chem. Res.* **2008**, *41*, 1772-1781.
32. Lara-Avila, S.; Danilov, A. V.; Kubatkin, S. E.; Broman, S. L.; Parker, C. R.; Nielsen, M. *B. J. Phys. Chem. C* **2011**, *115*, 18372-18377.
33. Zheng, Y. B.; Payton, J. L.; Chung, C.-H.; Liu, R.; Cheunkar, S.; Pathem, B. K.; Yang, Y.; Jensen, L.; Weiss, P. S. *Nano Lett.* **2011**, *11*, 3447-3452.
34. Kim, M.; Hohman, J. N.; Cao, Y.; Houk, K. N.; Ma, H.; Jen, A. K. Y.; Weiss, P. S. *Science* **2011**, *331*, 1312-1315.
35. Kudernac, T.; Ruangsapapichat, N.; Parschau, M.; Macia, B.; Katsonis, N.; Harutyunyan, S. R.; Ernst, K.-H.; Feringa, B. L. *Nature* **2011**, *479*, 208-211.
36. Donhauser, Z. J.; Mantooth, B. A.; Kelly, K. F.; Bumm, L. A.; Monnell, J. D.; Stapleton, J. J.; Price, D. W.; Rawlett, A. M.; Allara, D. L.; Tour, J. M.; Weiss, P. S. *Science* **2001**, *292*, 2303-2307.
37. Lewis, P. A.; Inman, C. E.; Maya, F.; Tour, J. M.; Hutchison, J. E.; Weiss, P. S. *J. Am. Chem. Soc.* **2005**, *127*, 17421-17426.
38. Alemani, M.; Peters, M. V.; Hecht, S.; Rieder, K.-H.; Moresco, F.; Grill, L. *J. Am. Chem. Soc.* **2006**, *128*, 14446-14447.
39. Morgenstern, K. *Acc. Chem. Res.* **2009**, *42*, 213-223.

40. Cipolloni, M.; Ortica, F.; Bougdid, L.; Moustrou, C.; Mazzucato, U.; Favaro, G. *J. Phys. Chem. A* **2008**, *112*, 4765-4771.
41. Broman, S. L.; Petersen, A. U.; Tortzen, C. G.; Vibenholt, J.; Bond, A. D.; Nielsen, M. B. *Org. Lett.* **2012**, *14*, 318-321.
42. Berkovic, G.; Krongauz, V.; Weiss, V. *Chem. Rev.* **2000**, *100*, 1741-1753.
43. Raymo, F. M.; Alvarado, R. J.; Giordani, S.; Cejas, M. A. *J. Am. Chem. Soc.* **2003**, *125*, 2361-2364.
44. Raymo, F. M.; Giordani, S.; White, A. J. P.; Williams, D. J. *J. Org. Chem.* **2003**, *68*, 4158-4169.
45. Tian, H.; Qin, B.; Yao, R. X.; Zhao, X. L.; Yang, S. J. *Adv. Mater.* **2003**, *15*, 2104-2107.
46. Daub, J.; Beck, M.; Knorr, A.; Spreitzer, H. *Pure Appl. Chem.* **1996**, *68*, 1399-1404.
47. Ranganathan, S.; Steidel, I.; Anariba, F.; McCreery, R. L. *Nano Lett.* **2001**, *1*, 491-494.
48. Hahm, S. G.; Lee, S. W.; Lee, T. J.; Cho, S. A.; Chae, B.; Jung, Y. M.; Bin Kim, S.; Ree, M. *J. Phys. Chem. B* **2008**, *112*, 4900-4912.
49. Gilat, S. L.; Kawai, S. H.; Lehn, J. M. *Chem. Eur. J.* **1995**, *1*, 275-284.
50. Irie, M. *Chem. Rev.* **2000**, *100*, 1685-1716.
51. Tian, H.; Yang, S. J. *Chem. Soc. Rev.* **2004**, *33*, 85-97.
52. Kronemeijer, A. J.; Akkerman, H. B.; Kudernac, T.; van Wees, B. J.; Feringa, B. L.; Blom, P. W. M.; de Boer, B. *Adv. Mater.* **2008**, *20*, 1467-1473.
53. Saha, S.; Stoddart, J. F. *Chem. Soc. Rev.* **2007**, *36*, 77-92.
54. Cygan, M. T.; Dunbar, T. D.; Arnold, J. J.; Bumm, L. A.; Shedlock, N. F.; Burgin, T. P.; Jones, L.; Allara, D. L.; Tour, J. M.; Weiss, P. S. *J. Am. Chem. Soc.* **1998**, *120*, 2721-2732.
55. Fichou, D. *J. Mater. Chem.* **2000**, *10*, 571-588.

56. Moore, A. M.; Mantooth, B. A.; Donhauser, Z. J.; Maya, F.; Price, D. W.; Yao, Y. X.; Tour, J. M.; Weiss, P. S. *Nano Lett.* **2005**, *5*, 2292-2297.
57. Moore, A. M.; Mantooth, B. A.; Donhauser, Z. J.; Yao, Y. X.; Tour, J. M.; Weiss, P. S. *J. Am. Chem. Soc.* **2007**, *129*, 10352-10353.
58. Fernandez-Acebes, A.; Lehn, J. M. *Chem. Eur. J.* **1999**, *5*, 3285-3292.
59. Osuka, A.; Fujikane, D.; Shinmori, H.; Kobatake, S.; Irie, M. *J. Org. Chem.* **2001**, *66*, 3913-3923.
60. Liddell, P. A.; Kodis, G.; Moore, A. L.; Moore, T. A.; Gust, D. *J. Am. Chem. Soc.* **2002**, *124*, 7668-7669.
61. Areephong, J.; Browne, W. R.; Katsonis, N.; Feringa, B. L. *Chem. Commun.* **2006**, 3930-3932.
62. Fischer, C.; Daub, J. *Chem. Ber. Recl.* **1993**, *126*, 1631-1634.
63. Daub, J.; Mrozek, T.; Ajayaghosh, A. *Mol. Cryst. Liq. Cryst.* **2000**, *344*, 41-50.
64. Petersen, M. A.; Broman, S. L.; Kadziola, A.; Kilsa, K.; Nielsen, M. B. *Eur. J. Org. Chem.* **2009**, 2733-2736.
65. Broman, S. L.; Petersen, M. A.; Tortzen, C. G.; Kadziola, A.; Kilsa, K.; Nielsen, M. B. *J. Am. Chem. Soc.* **2010**, *132*, 9165-9174.
66. Perrier, A.; Maurel, F.; Jacquemin, D. *Phys. Chem. Chem. Phys.* **2011**, *13*, 13791-13799.
67. Broman, S. L.; Lara-Avila, S.; Thisted, C. L.; Bond, A. D.; Kubatkin, S.; Danilov, A.; Nielsen, M. B. *Adv. Funct. Mater.* In Press (10.1002/adfm.201200897).
68. Nielsen, M. B.; Broman, S. L.; Petersen, M. A.; Andersson, A. S.; Jensen, T. S.; Kilsa, K.; Kadziola, A. *Pure Appl. Chem.* **2010**, *82*, 843-852.

69. Achatz, J.; Fischer, C.; Salbeck, J.; Daub, J. *J. Chem. Soc., Chem. Commun.* **1991**, 504-507.
70. Gorner, H.; Fischer, C.; Gierisch, S.; Daub, J. *J. Phys. Chem.* **1993**, 97, 4110-4117.
71. Spreitzer, H.; Daub, J. *Chem. Eur. J.* **1996**, 2, 1150-1158.
72. Ern, J.; Petermann, M.; Mrozek, T.; Daub, J.; Kuldova, K.; Kryschi, C. *Chem. Phys.* **2000**, 259, 331-337.
73. Mrozek, T.; Gorner, H.; Daub, J. *Chem. Eur. J.* **2001**, 7, 1028-1040.
74. De Waele, V.; Schmidhammer, U.; Mrozek, T.; Daub, J.; Riedle, E. *J. Am. Chem. Soc.* **2002**, 124, 2438-2439.
75. Petersen, M. A.; Kilsa, K.; Kadziola, A.; Nielsen, M. B. *Eur. J. Org. Chem.* **2007**, 1415-1418.
76. Parker, C. R.; Tortzen, C. G.; Broman, S. L.; Schau-Magnussen, M.; Kilsa, K.; Nielsen, M. B. *Chem. Commun.* **2011**, 47, 6102-6104.
77. Bumm, L. A.; Arnold, J. J.; Charles, L. F.; Dunbar, T. D.; Allara, D. L.; Weiss, P. S. *J. Am. Chem. Soc.* **1999**, 121, 8017-8021.
78. Donhauser, Z. J.; Price, D. W.; Tour, J. M.; Weiss, P. S. *J. Am. Chem. Soc.* **2003**, 125, 11462-11463.
79. Valiev, M.; Bylaska, E. J.; Govind, N.; Kowalski, K.; Straatsma, T. P.; Van Dam, H. J. J.; Wang, D.; Nieplocha, J.; Apra, E.; Windus, T. L.; de Jong, W. A. *Comput. Phys. Commun.* **2010**, 181, 1477-1489.
80. Hohenberg, P.; Kohn, W. *Phys. Rev.* **1964**, 136, B864-B871.
81. Kohn, W.; Sham, L. J. *Phys. Rev.* **1965**, 140, A1133-A1138.
82. Runge, E.; Gross, E. K. U. *Phys. Rev. Lett.* **1984**, 52, 997-1000.

83. Lee, C.; Yang, W.; Parr, R. G. *Phys. Rev. B* **1988**, *37*, 785-789.
84. Rau, H.; Lueddecke, E. *J. Am. Chem. Soc.* **1982**, *104*, 1616-1620.
85. Bortolus, P.; Monti, S. *J. Phys. Chem.* **1987**, *91*, 5046-5050.

## **CHAPTER 7**

### ***OUTLOOK***

## 7.1 OUTLOOK

In this chapter, I discuss the future directions of the design, control, and measurement of molecular assemblies. Based on our understanding from single-molecule and ensemble measurements, we can design better molecules to harness enhanced and precise molecular function at the nanoscale. I will discuss designs of new molecules in subsections based on the kind of molecular motion/function.

### 7.1.1 AZOBENZENE

Scanning-tunneling-microscope-based measurements have revealed unprecedented cooperative motion of nanoscale assemblies (Chapter 3) and highly sensitive SERS measurements revealed the tunability of dipole-dipole interactions by exploiting nanoscale fabrication via self- and directed assembly of azobenzene-functionalized molecules. By comparing the efficiency of photoisomerization of isolated single molecules, 1D linear chains, and 2D clusters, we were able to elucidate the limits of molecular motion and identified the critical players such as the conductivity of the tether, the spatial freedom required for the functional moiety, and the intermolecular interactions that determine molecular function at the nanoscale. By designing tethers that enable sufficient spatial freedom for azobenzene moieties to switch without steric interference, 2D films of functional molecules can be fabricated and cooperative reversible isomerization of single-component systems can be achieved. Adamantanetrithiols have been shown to assemble on Au{111} with intermolecular separations of  $\sim 7.4$  Å.<sup>1</sup> If azobenzene molecules are functionalized with these bulky adamantanetrithiols (Fig. 7.1), the lateral separation provides enough spatial freedom for the azobenzene moieties to switch *without* interactions from the neighboring molecules. The S atoms of each trithiol cage



are separated from the S atom of neighboring molecule by  $\sim 2.88$  Å, indicating that strong intermolecular interactions are possible. Moreover, adamantane cage molecules are known to assemble on metal substrates with fewer defects than do alkanethiols. Hence, increased and uniform surface coverage of azobenzene-functionalized adamantanetrithiol is possible, potentially resulting in enhanced photoisomerization cross sections of the SAM.

It is known that surface modification of metals with SAMs of organic molecules can introduce changes to the work function of the material. It is also known that by tuning the surface polarity, the hydrophilicity of a metallic surface can be tuned. Azobenzene has 0 D dipole moment in its *trans* conformation and the dipole moment increases to 3 D after conversion to *cis* conformation. If a 2D film of these organic molecules can be cooperatively switched between polar and nonpolar states, the simultaneous nanoscale motion can be employed to induce microscale motion on the surface.<sup>2-4</sup> Moreover, by introducing a dipole moment into the functional moiety in its *trans* conformation (Fig. 7.2) and by studying the effects of photoisomerization on such systems, the effect of molecular polarity on the work function of the materials can be understood. Kelvin probe measurements on 2D SAMs of such molecular systems will reveal interesting properties of concerted nanoscale motion on the properties of materials. Single-molecule measurements that can reveal the effects of tunneling electrons on molecular switching can be performed using STM (see chapter 3 for details on experimental setup and materials and methods).

### 7.1.2 DIHYDROAZULENE

We have demonstrated that dihydroazulene-functionalized molecules can be switched between an open form and a closed form using light (Fig. 7.3). Our initial theoretical

calculations reveal that **DHA** is more conductive than **VHF** and the electron transport properties vary dramatically when the molecule switches between closed and open forms of the five-membered ring of the **DHA** moiety (unpublished results). Moreover, DHA molecules were successfully isolated as single molecules in alkanethiol matrices and the reversible isomerization has been demonstrated at ensemble scales using SERS (see chapter 6). *In situ* single-molecule measurements using STM can reveal the changes in conductance of isolated molecules (without change in physical height). Scanning tunneling microscopy can be employed to study the I-V characteristics of the monolayer before and after illumination with UV light and the experimental results can be compared with our initial theoretical calculations. Using nanofabrication techniques that have been demonstrated previously,<sup>5</sup> 2D films of these molecules can be sandwiched between two metal electrodes and by controlling the conductance of the molecules via external stimulus, a functional device can be fabricated.

### 7.1.3 ROTAXANE

Mechanically interlocked molecules (MIMs) are a class of molecular switches based on noncovalent interactions between two or more components that can move relative to one other.<sup>6-8</sup> Bistable catenanes and rotaxanes are two commonly studied MIMs.<sup>9-13</sup> Rotaxanes are shaped like a dumbbell with a ring threaded on the shaft (Fig. 7.4A). The cyclobis(paraquat-*p*-phenylene) ring (CBPQT<sup>4+</sup>, shown in blue) can associate noncovalently with either of two stations: a tetrathiafulvalene station (TTF, shown in green) or a dioxynaphthalene station (DNP, shown in red). When the TTF station is in its thermodynamically favorable neutral state, the CBPQT<sup>4+</sup> ring docks to the TTF station through electron donor-acceptor interactions. When oxidized, the TTF loses two electrons, resulting in electrostatic repulsion between positive charges on the ring and the TTF station, pushing the ring to the DNP station. Upon reduction of

the TTF unit, the ring shuttles back to its original position.<sup>14-16</sup> Properties of rotaxanes have been well established in solution. However, surface switching is also important for potential device applications, and as with azobenzenes and other switches, binding to the surface can change the behavior of the molecules.

To investigate the properties of surface-bound rotaxanes, in collaboration with Huang and Stoddart, we designed rotaxanes functionalized with dithiol tethers to facilitate binding to Au{111}, and monitored molecular motion *in situ* using electrochemically controlled STM.<sup>16</sup> Individual tethered rotaxanes on Au{111} appear as a single protrusion on the surface in STM images.<sup>16</sup> Since the rotaxane shaft is much less conductive than the ring, the thread does not appear in STM images, and the protrusions correspond to the location of the rings (Fig. 7.4A). Since STM images are convolutions of topographic and electronic effects, including the size of the probe tip, and since the ring is conductive, it typically has an apparent height of  $\sim 3$  Å and a lateral dimension of  $\sim 12$  Å, substantially larger than the physical diameter of the ring ( $\sim 5$  Å). Since only the ring is visible, the locations of the TTF and DNP stations are inferred from the locations of the ring when the STM is held at low ( $\sim 0.1$  V) and high ( $\sim 0.5$  V) potentials. Blue and red arrows in Fig. 7.4A show the direction and magnitude of each ring motion as the electrochemical potential is raised and lowered, respectively.

Measuring the motions of many individual rings reveals the behavior of the molecules bound to the surface (Fig. 7.4B). For the oxidation step, a root mean square displacement of  $\sim 20$  Å was observed (smaller than the 32 Å distance between the two stations in the extended molecule) (Fig. 7.4C). Along with the wide observed distribution (0–55 Å) of displacements, this suggests bending of the flexible thread, and interactions between the rings and the substrate in some cases. Thus, rotaxanes with a more rigid shaft would be expected to exhibit improved

device performance, producing a tighter distribution of shuttling distances nearer to the inter-station distance. In addition, proximate molecules were found to interfere with one another.

As with photochromic switches, mechanically interlocked switches bound to surfaces can be used together to perform microscopic work.<sup>15,17</sup> Figure 7.5A shows the structure of a bistable rotaxane used to induce mechanical strain in a solid substrate, similar to the contraction of a muscle. The shaft contains four stations, and is encircled by two rings, which are thiolated and bound to the gold surface. Upon oxidation, the positively charged TTF<sup>+</sup> stations propel the rings toward the DNP stations, straining the substrate. Upon subsequent reduction, the rings shuttle back to the original positions.<sup>14,15</sup> Cantilevers coated with rotaxanes on one side and held in a microfluidic chamber deflected by ~30 nm when chemical oxidizing and reducing agents were added, repeatable for several oxidation and reduction cycles.<sup>17</sup> However, electrochemically controlled actuation (similar to the STM experiments) produced nearly an order of magnitude greater deflection of the cantilever (~ 300 nm) (Fig. 7.5B), reversible through hundreds of oxidation/reduction cycles.<sup>15</sup> Thus, the collective nanoscale motion of ~8 billion molecules induced micron-scale motion of the cantilevers.

If intermolecular interactions were designed into this system to guide assembly and the threads were synthesized to be rigid and conjugated, we anticipate that greater and cooperative forces and action would be induced. To this end, we have designed oligorotaxanes in collaboration with Prof. Stoddart's group (Fig. 7.6A). A preliminary X-ray crystal structure of the oligo DNP/CBPQT ring complex showed that there exists chain folding of DNP thread in the presence of the rings and continuous donor-acceptor interactions between DNP stations and the rings, forming rigid stacks. The additional binding force is hydrogen bonding (C-H....O) between the ring and the glycol chain. The distance of the rigid part of the structure is 3.85 nm

calculated from extreme aromatic rings (each aromatic ring is 3.5 Å thick). The distance between the two disulfide ligands is greater 3.85 nm due to the inclusion of the lengths of flexible chain of the stopper and alkyl chains attached to the ligand.

Initial STM measurements revealed that the feature size of individual molecules is not uniform, indicating that the molecule is not completely rigid (feature sizes varied between 30 - 40 Å). However, due to the high conductance of the rings on the linear thread, intramolecular resolution could not be obtained (Fig. 7.6B). Low-temperature UHV (LT-UHV) measurements are underway in order to develop sufficient statistics on the rigidity of the molecules when molecular motion is precluded.

Force-curve measurements on isolated single molecules using stable AFM could reveal very interesting properties of these oligorotaxanes. One end of the disulfide ligand of the oligorotaxane is tethered to the Au{111} surface and the molecules can be pulled using a Au-coated AFM tip to unfold the oligorotaxane structure into its linear analogue. The secondary interaction force between the ring and the unbound DNP unit would be expressed by the mechanical force read by the AFM tip. In principle, more mechanical input is necessary for the extended oligorotaxanes to break up the folding structure.

A longer version of the molecule with an additional ring incorporated into the system has also been designed (Fig. 7.7A). Similar measurements will be performed on this longer supramolecule in order to understand both the intramolecular interactions using AFM and the rigidity and intermolecular interactions using STM. Initial measurements revealed that the molecules are not rigid upon adsorption on Au{111}. Lengths of the molecules varied between a fully extended form of ~60 Å and the shortest features were ~30 Å. Most commonly, the

molecules were found in a distorted rectangular feature with diagonal distance of  $\sim 40$  Å, indicating that the molecules adsorb in a looped thread orientation (Fig. 7.7B). However, it should be noted that the molecules desorbed after repeated scanning over the same area, indicating that molecular motion takes place under the imaging conditions. In order to explore the submolecular features and to develop sufficient statistics to calculate the separation between the consecutive rings within the molecules, LT-UHV measurements are required.

Molecules in which the  $\pi$ - $\pi$  interactions of the aromatic rings (separated by 3.5 Å) make the thread rigid and help retain its linearity have also been synthesized recently (Fig. 7.8). Ambient STM measurements on isolated single-molecules revealed that the molecules do not form ordered monolayers due to the thioether functional groups at the end. Although isolated single molecules were observed on Au{111}, the molecules desorbed from the surface while the probe tip rastered over the imaging area. Due to this, submolecular features could not be observed under ambient conditions. However, sample preparation at 1  $\mu$ M concentration did result in the adsorption of isolated single molecules. Measurements using a LT-UHV STM are underway such that the molecules can be frozen on the Au surface thereby restricting the mobility of the molecule thus enabling us to resolve the submolecular features. These single-molecule measurements from both STM and AFM will help us understand the behavior of these supramolecules and guide us in increasing the efficiency of mechanical work that can be harnessed from the cooperative motion of functional molecules.

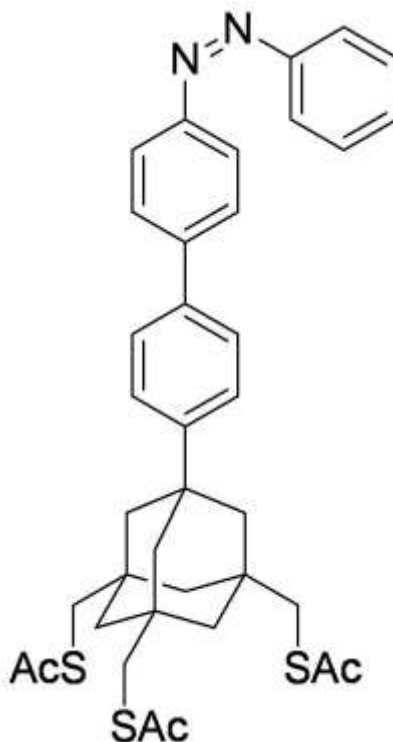


**Figure 7.1.** Structure of azobenzene-functionalized adamantanetrithioacetate molecule. The lateral separation between neighboring surface-bound molecules will be  $\sim 7.4$  Å, providing enough spatial freedom for the azobenzene moiety to switch between *trans* and *cis* conformations.

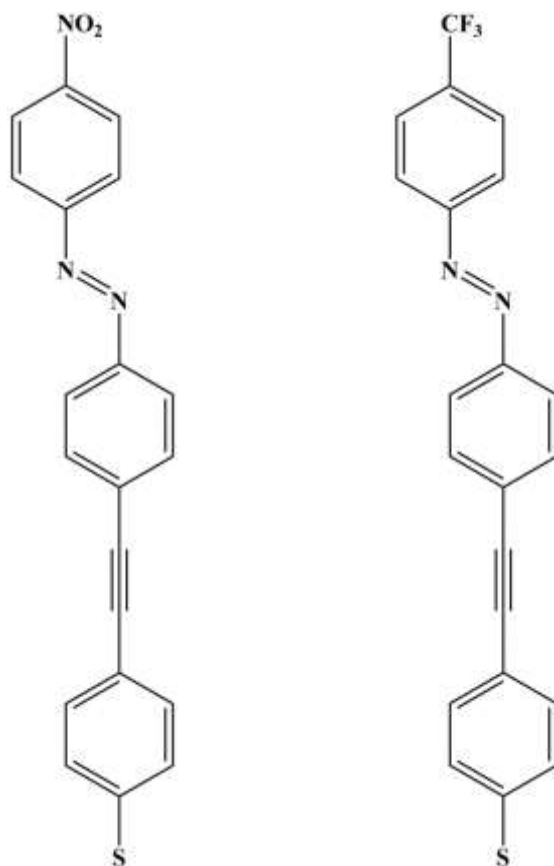


**Figure 7.2.** Structures of azobenzene terminally functionalized with polar (left) NO<sub>2</sub> functional group and (right) CF<sub>3</sub> functional groups. Introduction of dipole to the trans conformation of the azobenzene moiety will help elucidate the effect of dipole moment on the photoisomerization cross sections of the molecules when assembled on solid substrates and the effects on the work function of the metal before and after isomerization.



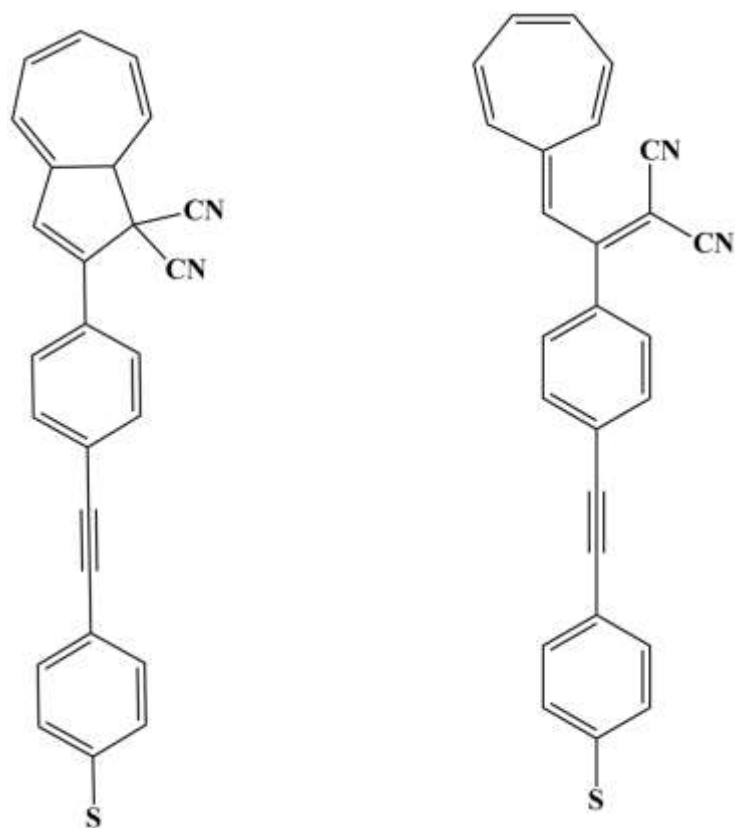


**Figure 7.3.** Structures of the dihydroazulene-functionalized molecule (in its closed form, left) and vinylheptafulvalene (in its open form, right) studied.

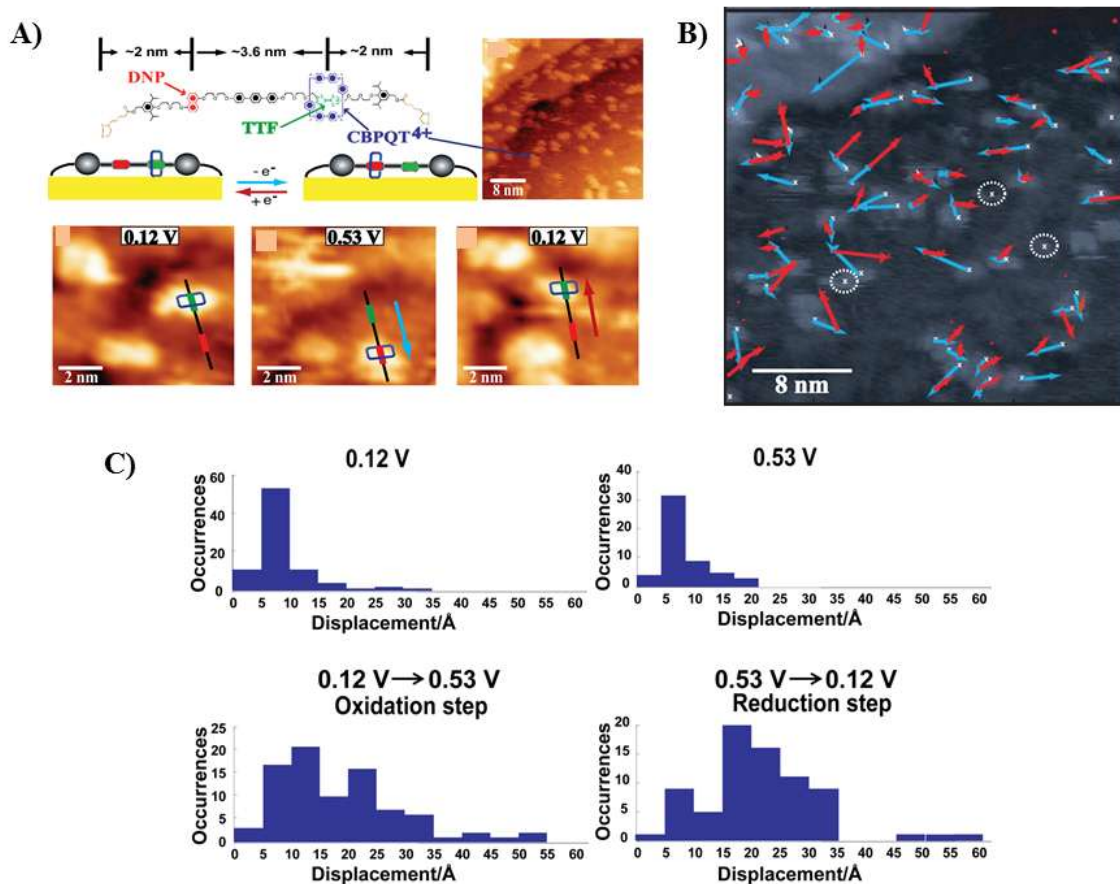


**Figure 7.4.** A) Structure of a surface-bound rotaxane. Initially, the ring docks at the TTF station, shown in green. Upon oxidizing the TTF unit at 0.53 V, the ring shuttles to the red DNP unit (blue arrow). Subsequent reduction of the TTF unit propels the ring back to the original position (red arrow). B) Three STM images (initial, after oxidation, and after reduction) superimposed on each other show the translation of the rings on the rotaxane molecules shuttling between the DNP and TTF stations. The blue arrows indicate the motion of the ring after the oxidation step and the red arrows indicate the motion after the reduction step. C) Histograms depicting the displacements of the protrusions in STM at equilibrium potentials of 0.12 V and 0.53 V (top). The displacement of rings after the oxidation step showing a range of 0-55 Å with a root mean

square (rms) displacement of 20 Å and after the reduction step with a rms displacement of 16 Å (bottom). Figure reproduced with permission from reference 11. Copyright ACS 2010.

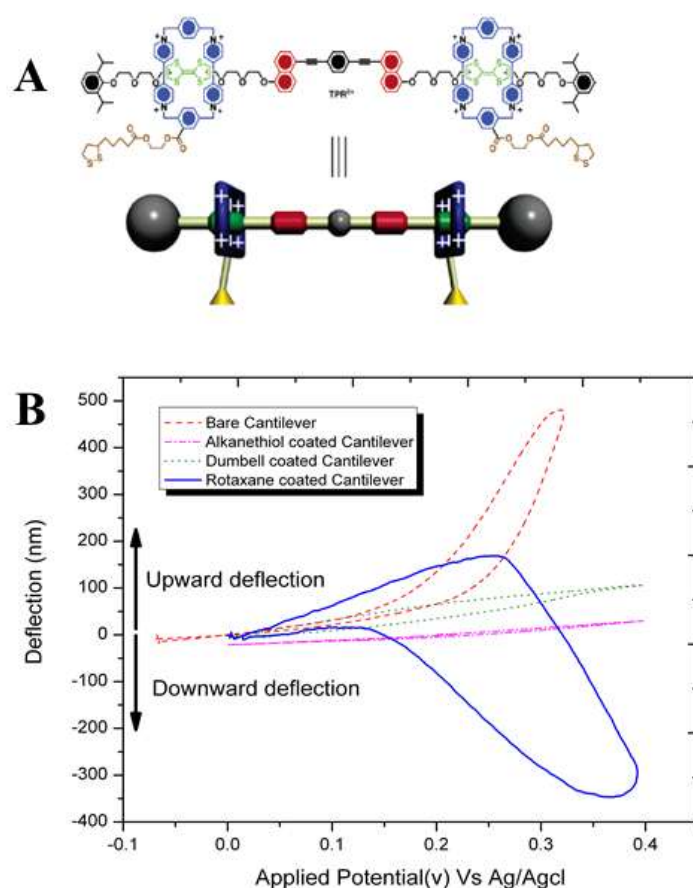


**Figure 7.5.** A) Schematic of surface-bound rotaxanes. B) Deflections of the cantilever after reduction and oxidation sweeps. Bare cantilever deflection in the upward direction due to perchlorate adsorption during the forward sweep, and perchlorate desorption during the backward sweep (red). Control experiments with alkanethiols (pink) and molecules *without* the rings (green) blocked some of the ion adsorption/desorption (more for the higher quality alkanethiol monolayer). Cantilever assembled with functional rotaxanes showed upward deflection at low potential due to some ion adsorption and downward deflection once a potential

is reached where the TTF unit oxidizes, indicating the onset of ring shuttling and hence stress on the substrate. Figure reproduced with permission from reference 10. Copyright ACS 2009.

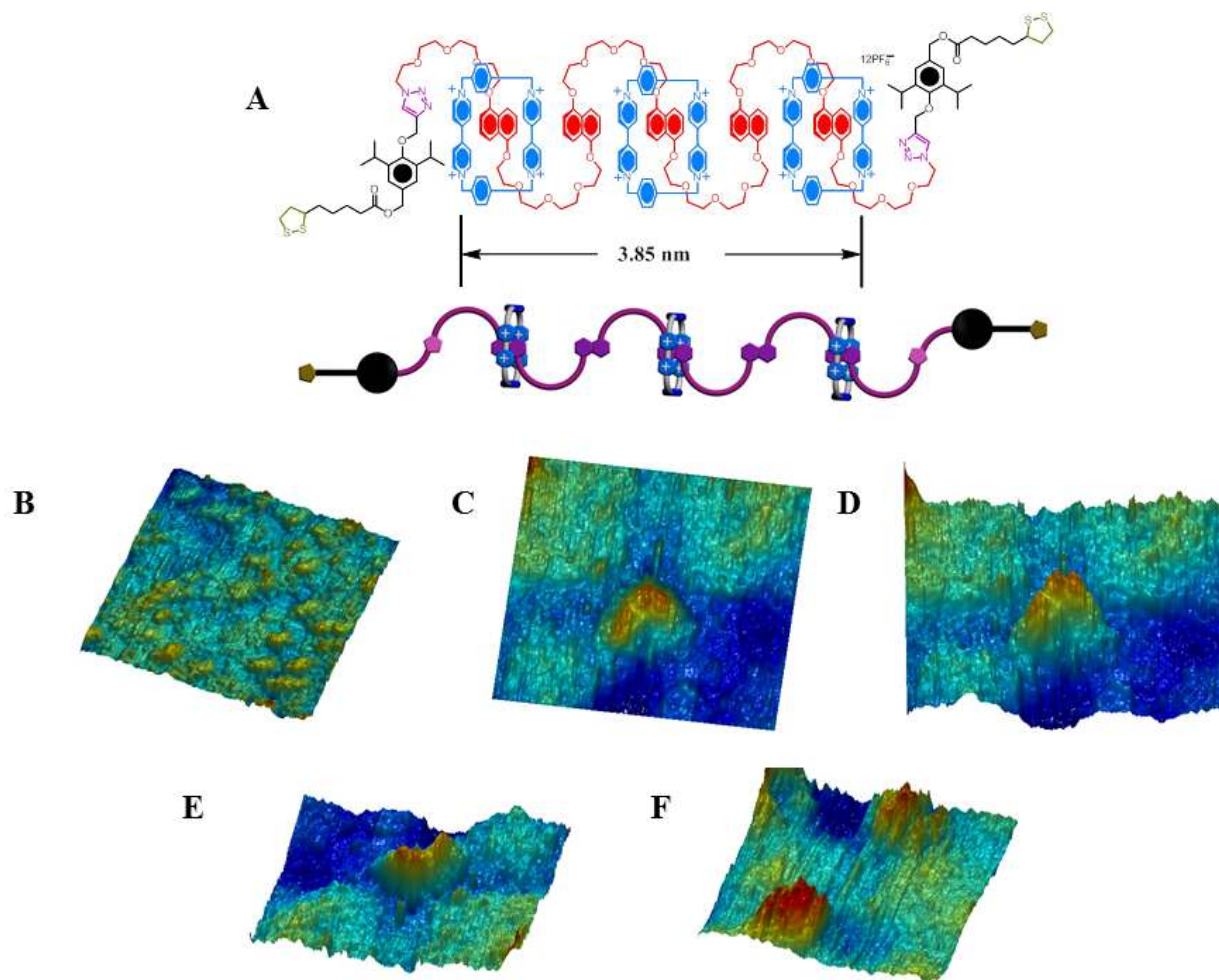


**Figure 7.6.** A) Structure of polyrotaxane (5NP[4]R) functionalized with dithiol tethers in order to enable adsorption to Au. B) Scanning tunneling microscope image of isolated single molecules of 5NP[4]R showing the varied size distribution of rotaxane molecules indicating that the molecular thread is not rigid. C-F) High-resolution images of isolated single molecules showing a curved feature indicating that the molecular thread is not rigid and that the molecules orient themselves in bent conformations when adsorbed on a metal surface. Imaging conditions:  $V_s = -1.0$  V and  $I_t = 2$  pA.

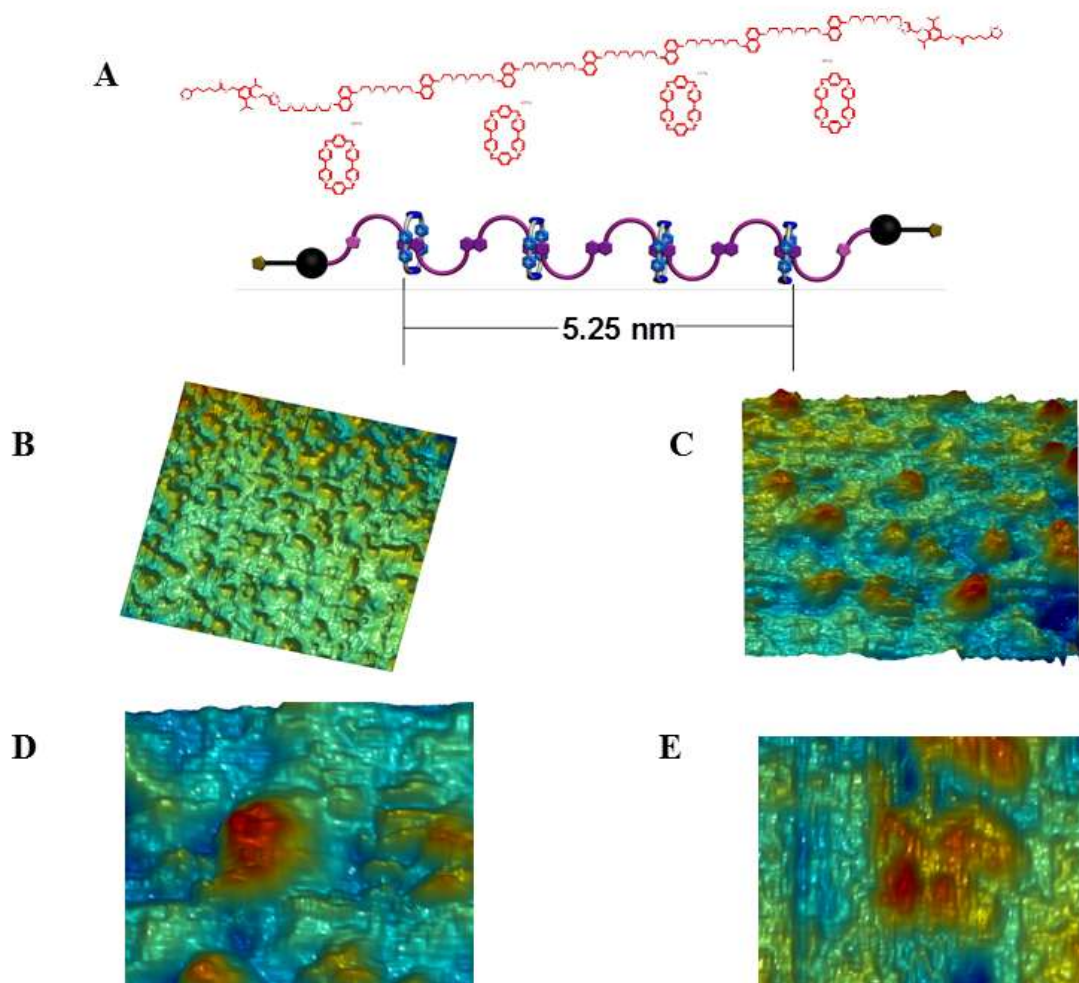


**Figure 7.7.** A) Structure of a longer polyrotaxane (7NP[5]R) functionalized with dithiol tethers. B, C) Scanning tunneling microscope images of isolated single molecules of 7NP[5]R showing the variation in feature size. D, E) High-resolution images showing the preferred looped orientation of single molecules. Imaging conditions:  $V_s = -1.0$  V and  $I_t = 2$  pA.

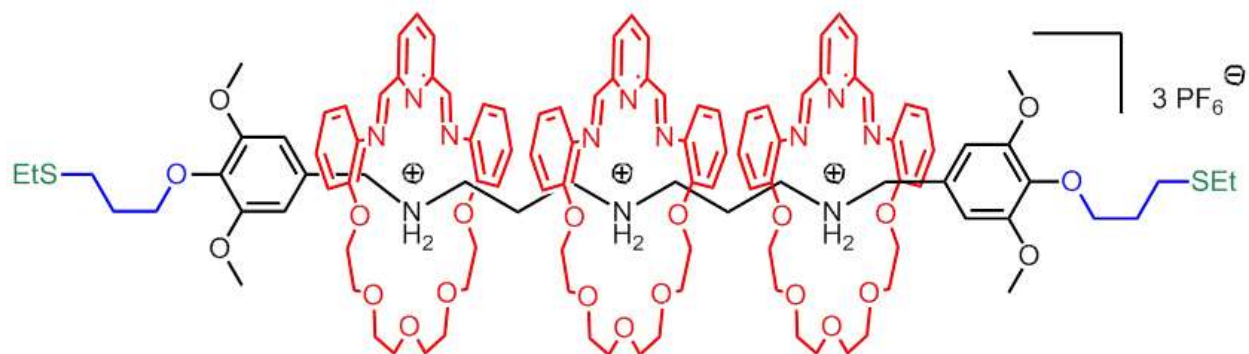


**Figure 7.8.** Structure of a [4]rotaxane **3R.3PF<sub>6</sub>** molecule (designated as ***n*R·*n*PF<sub>6</sub>**, where *n* is equal to the number of  $-\text{CH}_2\text{NH}_2^+\text{CH}_2-$  recognition sites) with thioether functionality.



## 7.2 REFERENCES

1. Katano, S.; Kim, Y.; Matsubara, H.; Kitagawa, T.; Kawai, M. *J. Am. Chem. Soc.* **2007**, *129*, 2511-2515.
2. Ichimura, K.; Oh, S. K.; Nakagawa, M. *Science* **2000**, *288*, 1624-1626.
3. Hugel, T.; Holland, N. B.; Cattani, A.; Moroder, L.; Seitz, M.; Gaub, H. E. *Science* **2002**, *296*, 1103-1106.
4. Koshima, H.; Ojima, N.; Uchimoto, H. *J. Am. Chem. Soc.* **2009**, *131*, 6890-6891.
5. Kronemeijer, A. J.; Akkerman, H. B.; Kudernac, T.; van Wees, B. J.; Feringa, B. L.; Blom, P. W. M.; de Boer, B. *Adv. Mater.* **2008**, *20*, 1467-1473.
6. Balzani, V.; Gomez-Lopez, M.; Stoddart, J. F. *Acc. Chem. Res.* **1998**, *31*, 405-414.
7. Coti, K. K.; Belowich, M. E.; Liong, M.; Ambrogio, M. W.; Lau, Y. A.; Khatib, H. A.; Zink, J. I.; Khashab, N. M.; Stoddart, J. F. *Nanoscale* **2009**, *1*, 16-39.
8. Davis, J. J.; Orlowski, G. A.; Rahman, H.; Beer, P. D. *Chem. Commun.* **2010**, *46*, 54-63.
9. Asakawa, M.; Ashton, P. R.; Balzani, V.; Credi, A.; Hamers, C.; Mattersteig, G.; Montalti, M.; Shipway, A. N.; Spencer, N.; Stoddart, J. F.; Tolley, M. S.; Venturi, M.; White, A. J. P.; Williams, D. J. *Angew. Chem. Int. Ed.* **1998**, *37*, 333-337.
10. Flood, A. H.; Stoddart, J. F.; Steuerman, D. W.; Heath, J. R. *Science* **2004**, *306*, 2055-2056.
11. Liu, Y.; Flood, A. H.; Bonvallett, P. A.; Vignon, S. A.; Northrop, B. H.; Tseng, H. R.; Jeppesen, J. O.; Huang, T. J.; Brough, B.; Baller, M.; Magonov, S.; Solares, S. D.; Goddard, W. A.; Ho, C. M.; Stoddart, J. F. *J. Am. Chem. Soc.* **2005**, *127*, 9745-9759.
12. Stoddart, J. F.; Colquhoun, H. M. *Tetrahedron* **2008**, *64*, 8231-8263.
13. Stoddart, J. F. *Chem. Soc. Rev.* **2009**, *38*, 1802-1820.

14. Zheng, Y. B.; Yang, Y. W.; Jensen, L.; Fang, L.; Juluri, B. K.; Flood, A. H.; Weiss, P. S.; Stoddart, J. F.; Huang, T. J. *Nano Lett.* **2009**, *9*, 819-825.
15. Juluri, B. K.; Kumar, A. S.; Liu, Y.; Ye, T.; Yang, Y. W.; Flood, A. H.; Fang, L.; Stoddart, J. F.; Weiss, P. S.; Huang, T. J. *ACS Nano* **2009**, *3*, 291-300.
16. Ye, T.; Kumar, A. S.; Saha, S.; Takami, T.; Huang, T. J.; Stoddart, J. F.; Weiss, P. S. *ACS Nano* **2010**, *4*, 3697-3701.
17. Huang, T. J.; Brough, B.; Ho, C. M.; Liu, Y.; Flood, A. H.; Bonvallet, P. A.; Tseng, H. R.; Stoddart, J. F.; Baller, M.; Magonov, S. *Appl. Phys. Lett.* **2004**, *85*, 5391-5393.